CHARACTERIZATION OF VORTEX RING IN ABDOMINAL AORTIC ANEURYSM PHANTOM USING PARTICLE IMAGE VELOCIMETRY

A THESIS SUBMITTED TO
THE GRADUATE SCHOOL OF NATURAL AND APPLIED SCIENCES
OF
MIDDLE EAST TECHNICAL UNIVERSITY

BY

KEREM TUĞ GÖKÇEK

IN PARTIAL FULFILLMENT OF THE REQUIREMENTS
FOR
THE DEGREE OF MASTER OF SCIENCE
IN
MECHANICAL ENGINEERING

SEPTEMBER 2021

Approval of the thesis:

CHARACTERIZATION OF VORTEX RING IN ABDOMINAL AORTIC ANEURYSM PHANTOM USING PARTICLE IMAGE VELOCIMETRY

submitted by **KEREM TUĞ GÖKÇEK** in partial fulfillment of the requirements for the degree of **Master of Science** i**n Mechanical Engineering, Middle East Technical University** by,

Prof. Dr. Halil Kalıpçılar
Dean, Graduate School of **Natural and Applied Sciences** _____

Prof. Dr. M. A. Sahir Arıkan
Head of the Department, **Mechanical Engineering** _____

Prof. Dr. M. Metin Yavuz
Supervisor, **Mechanical Engineering, METU** _____

Examining Committee Members:

Assoc. Prof. Dr. Cüneyt Sert
Mechanical Eng., METU _____

Prof. Dr. M. Metin Yavuz
Mechanical Eng., METU _____

Assist. Prof. Dr. Ö. Uğraş Baran
Mechanical Eng., METU _____

Assist. Prof. Dr. Ali Karakuş
Mechanical Eng., METU _____

Prof. Dr. Murat Kadri Aktaş
Mechanical Eng., TOBB ETU _____

Date: 01.09.2021

I hereby declare that all information in this document has been obtained and presented in accordance with academic rules and ethical conduct. I also declare that, as required by these rules and conduct, I have fully cited and referenced all material and results that are not original to this work.

Name Last name : Kerem Tuğ Gökçek

Signature :

ABSTRACT

CHARACTERIZATION OF VORTEX RING IN ABDOMINAL AORTIC ANEURYSM PHANTOM USING PARTICLE IMAGE VELOCIMETRY

Gökçek, Kerem Tuğ
Master of Science, Mechanical Engineering
Supervisor: Prof. Dr. M. Metin Yavuz

September 2021, 110 pages

Abdominal aortic aneurysm (AAA) is the permanent enlargement of the abdominal artery that may even rupture at the end, and it is a critical medical situation with a high mortality rate. Although there are some approaches to model its enlargement and rupture, a complete understanding is far from over. A vortex ring is generated during physiological flow pattern, and its evolution should be analyzed in detail to understand its effect on the flow field. The aim of this study is to investigate and characterize vortex rings in a simplified abdominal aortic aneurysm geometry using an experiment setup with Particle Image Velocimetry (PIV) measurement method.

An experimental setup is designed and established to simulate physiological flow patterns through a AAA geometry with refractive index match of the phantom and the working fluid. Different vortex identification methods, including λ_{ci} - criterion, Q - criterion, Δ - criterion and λ_2 - criterion have been reviewed and implemented. The vortex structures are characterized for certain phases of different cycles with these methods. A MATLAB code is developed to apply these methods to planar PIV data.

The results show that a vortex ring is formed as the instabilities arise, and multi vortex rings can occur simultaneously at certain phases due to collision of this vortex

ring with the walls. Furthermore, the mentioned vortex identification methods provided the same results. However, it is seen that they require noise reduction to obtain robust results. A couple of methods are tested for this purpose. Further studies are required to reveal more about the vortex mechanics.

Keywords: Abdominal Aortic Aneurysm, Vortex Identification, Hemodynamics, Particle Image Velocimetry

ÖZ

ABDOMİNAL AORT ANEVRİZMA FANTOMUNDAKİ VORTEKS HALKASININ PARTİKÜL GÖRÜNTÜ VELOSİMETRİYLE KARAKTERİZASYONU

Gökçek, Kerem Tuğ
Yüksek Lisans, Makina Mühendisliği
Tez Yöneticisi: Prof. Dr. M. Metin Yavuz

Eylül 2021, 110 sayfa

Abdominal aort anevrizması (AAA), bu damarın kalıcı olarak genişlemesidir ve damarın yırtılmasına kadar ilerleyebilir. Yüksek ölüm oranına sebep olan ciddi bir tıbbi durumdur. Damarın genişlemesini ve yırtılmasını modellemek için bazı yaklaşımlar olmasına rağmen henüz kesin olarak anlaşılmaktan oldukça uzaktır. Fizyolojik akış sırasında bir girdap halkası oluşur ve bu halkanın evriminin akış üzerindeki etkisini anlamak için ayrıntılı analizlere ihtiyaç vardır. Bu çalışmanın amacı, basitleştirilmiş bir abdominal aort anevrizması geometrisindeki girdap yapılarını, Parçacık Görüntü Hızı (PIV) ölçüm yöntemi ile bir deney düzeneği kullanarak incelemek ve karakterize etmektir.

Bir AAA geometrisinde fizyolojik akışı simüle edecek bir deney düzeneği tasarlanmış ve kurulmuştur. Damar modeli ile çalışma svısısı arasında kırılma indisi eşitliği sağlanmıştır. Farklı girdap tanımlama metotları; λ_{ci} - kriter, Q - kriter, Δ - kriter ve λ_2 - kriter, detaylıca araştırılmış ve ölçüm sonuçlarına uygulanmıştır. Girdap yapıları, akış çevrimlerinin belli döngüleri için karakterize edilmiştir. Bu yöntemleri düzlemsel PIV verilerine uygulamak için bir MATLAB kodu geliştirilmiştir.

Sonuçlar, kararsızlıklar arttıkça bir girdap halkasının oluştuğunu ve bu girdap halkasının duvarlarla çarpışması nedeniyle belirli fazlarda aynı anda çoklu girdap halkalarının oluşabileceğini göstermektedir. Ayrıca bahsedilen girdap tanımlama yöntemleri de aynı sonuçları vermiştir. Ancak daha iyi sonuçlar elde etmek için gürültü azaltma metotlarına ihtiyaç vardır. Bu amaçla birkaç yöntem denenmiştir. Girdap mekaniğini daha detaylı bir şekilde ortaya çıkarmak için daha ileri çalışmalara ihtiyaç vardır.

Anahtar Kelimeler: Abdominal Aort Anevrizması, Girdap Tanımlanması, Hemodinamik, Parçacık Görüntülemeli Hız Ölçme Metodu

To my family and my love

ACKNOWLEDGMENTS

This thesis has been conducted in collaboration with Qatar University under Qatar University International Research Collaboration Co-Funds (IRCC) Program (IRCC 2020-002).

I would like to thank TUBITAK for its support throughout my studies with the help of the scholarship programme, 2210 - E.

I would like express my sincere gratitude to the people who were always there for me during thesis studies. Firstly, I want to thank my thesis supervisor, Prof. Dr. Mehmet Metin Yavuz. He always gives the best recommendations both for academic career and social life. His extensive experiences contribute me a lot, and thanks to that I feel development after every day spent at the laboratory.

My parents, Yasin Murat Gökçek and Fatma Kızılca, always give me comfort and support me throughout this study. For sure these days are not possible without them.

I would also like to thank my friends and group members of the laboratory group. Firstly, Semih Türk always did his best. The mutual solidary between him and me made lots of hardships easy. Burcu Ramazanlı, Osman Ohtaroğlu and Kayacan Kestel always helped me with their experience. Oğuzhan Yılmaz was very willing to help in laboratory studies. Finally, I want to thank Mr. Mehmet Özçifçi for his efforts and support on the experimental setup of this study.

TABLE OF CONTENTS

LIST OF TABLES

TABLES

LIST OF FIGURES

FIGURES

LIST OF ABBREVIATIONS

ABBREVIATIONS

AAA	Abdominal aortic aneurysm
PIV	Particle image velocimetry
WSS	Wall shear stress
RI	Refractive index
VGT	Velocity gradient tensor
IA	Interrogation area

LIST OF SYMBOLS

SYMBOLS

Re	Reynolds number
Re_m	Mean Reynolds number with respect to time
Ω	Vorticity matrix
ω	Vorticity
x	Streamwise direction
y	Normal to streamwise direction
u	Velocity component in streamwise direction
v	Velocity component in normal to streamwise direction
T	Period
S	Strain matrix
μ	Dynamic viscosity
ν	Kinematic viscosity
ρ	Density
Q	Q - Criterion
λ_{ci}	Swirling strength criterion
λ_2	λ_2 - criterion
Δ	Δ - Criterion

CHAPTER 1

INTRODUCTION

Abdominal aortic aneurysm, shortly AAA, is defined as the persistent enlargement of the diameter of the abdominal aorta. The human heart generates the blood flow, and blood circulation is done by artery and vein systems throughout all body parts. After the blood is extracted from cardiac valves, it flows through in the order of the ascending aorta, aortic arch, and descending aorta. The abdominal aorta is the continuing part of the descending aorta located in the abdominal cavity. The abdominal aorta consists of many segments of veins, and this system of veins is responsible for transporting the blood to all body parts below the abdomen. The healthy diameter of the abdominal aorta is around 20 mm, and it is one of the arteries with the largest diameter magnitude. This diameter may increase in time due to various genetic or environmental reasons or a combination of them, and this situation becomes a critical health issue for a person. The AAA diagnosis for a patient is made after a critical threshold of this diameter as it widens, and the commonly accepted threshold is 30 mm [1]. After the threshold, the enlargement process of the aorta must be monitored carefully to treat the patient in the best way possible. However, AAA is asymptotic which makes it very critical and dangerous. The condition may become critical before AAA diagnosis, and it may be too late when it is realized. This enlargement process may even lead to rupture of the vessel. Necessary precautions must be taken beforehand since the rupture of AAA results in the death of the patient in 80% of cases [2]. This makes it one of the most dangerous threats to life expectancy and quality.

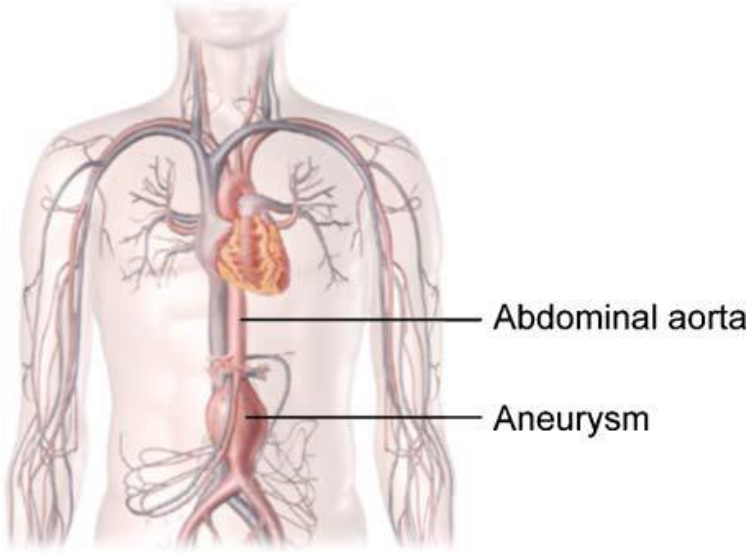

Figure 1.1: Abdominal aortic aneurysm [3]

There are many factors associated with the AAA. The exact mechanism of the rupture process for a patient cannot be defined yet due to insufficient data and the complexity of the problem. The potential causes of AAA include genetics and environmental effects. Heart-related diseases, hypertension and obesity are some of the genetic causes. For the environmental causes, smoking is one of the most prominent factors of AAA. For men with age ≥ 65, the AAA occurrence is strongly related to previous myocardial infarction and smoking for a lifetime [4]. Aging affects the structure of the arteries directly. An artery has three main layers. The innermost one is endothelium which is in contact with the blood. The outer one is median and the outermost one is named adventitia. The mechanical characteristics of arteries are defined with respect to collagen and elastin. Collagen is a protein type that is the basis of cartilage, and elastin provides elasticity. As a person gets older, the median layer becomes thinner dramatically and so its structure takes a segmented manner [5]. This situation increases the risk of mechanical failure of any vessel and also myocardial infarction. Another impact of getting older may be the increasing effect of fatigue stresses. These show that aging only can cause AAA as well.

From a mechanical point of view, the vessel will rupture when the vessel structure cannot stand against the mechanical forces acting on its boundaries due to the lack of structural integrity. To identify these forces, the flow field inside the artery must be analyzed as well.

The mortality rate and so the rupture risk gets higher as the diameters increases [6]. However, the diameter itself should not be considered as the primary rupture indicator. The rate of its change is also essential as it can indicate a higher rupture risk [7]. Another situation that throws suspicion on the diameter size is that there are ruptured cases although the diameter is not very large [6]. Computational fluid dynamics simulations showed that rupture zones of real ruptured cases correspond to low wall shear stress (WSS) zones, and these zones are correlated to thrombus generation locations [8]. WSS is the tangential component of the force per unit area applied by the blood on the vessel wall which depends on the velocity gradient vicinity of the vessel wall. Thrombus is created in the blood when a tissue is damaged so that the bleeding stops. This study indicates that high WSS magnitudes should not be considered as the primary indicator of the rupture. As the intraluminal thrombus increases in size, the rupture risk increases considerably. The small sized AAA cases with rupture are also related to this increased thrombus regions [9].

Thrombus may have a critical role in the rupture of the vessel and on the flow field. Thrombus formation occurs in most of the AAA cases. As the diameter of AAA increases, the thrombus distribution inside becomes more nonuniform [10]. Thrombus formation and distribution are known to be important in AAA cases, so this fact shows the risk of considering the diameter only as a parameter. The combined effect of large diameter and nonuniform thrombus may accelerate the rupture process. In a study that consists of sixty-seven AAA patients, it was found out that the rate of increase of thrombus size is a better indicator of rupture compared to the maximum diameter [11]. As it can be seen, there is no single parameter to follow. Moreover, a pure mechanical point of view or high shear stress approach is not appropriate as well. The possibility of thrombus formation being the prominent

risk factor and are correlated regions of low shear stresses reveal the importance of vortex structures in the flow fields.

As the aneurysm and so the enlargement starts, the flow behavior inside the vessel changes due to geometrical changes. This results in a flow with large spatial and temporal changes. In addition, blood is a mixture of different constitutes that behave differently under different conditions. The combination of all these makes the problem very complicated and intricate. WSS is one of the prominent flow terms in AAA. The velocity gradients near the wall are dependent on time naturally in physiological flow. With the geometric change caused by the aneurysm, these gradients will be under the effect of the spatial changes as well. One can simply think that high WSS is the cause of the rupture as the stress on the vessel wall increases and the mechanical integrity of the vessel is corrupted. Although this may sound correct preliminary, it is already discussed that it is not a right approach in most cases. Low shear stresses may be more critical due to thrombus formation. The low shear layer regions are generally seen where the vortex structures dominate the flow. A vortex can be simply defined as the region of fluid where accumulated fluid particles make a rotating motion around a common point in the flow field.

The potential reasons for rupture in the context of hemodynamics can be listed as; low wall shear stress, high wall shear stress, highly oscillating shear stress (both in magnitude and direction). Vortical structures occurring in AAA have a significant effect on the velocity gradient distribution throughout the AAA location. Hence, WSS and the parameters related to WSS are highly dependent on these vortical structures. This situation brings the need to study these vortical structures in detail to address their effect on flow field considering their effect on the blood platelets. The movement of platelets under the effect of a vortex may lead to the accumulation of them. This is an undesired situation that can end up with the partial blockage of the flow. Biological changes in the blood are affected by these structures as well.

1.1 Aim and Motivation of the Study

As the exact mechanism of enlargement and rupture mechanism is still unknown, the effect of the temporal and spatial changes of the vortex structures on the flow field in the aneurysm is still a fundamental question mark. There are various studies about the wall shear stress in AAA considering that WSS may be the apparent parameter affecting the integrity of the artery walls. However, WSS distribution or many other parameters that are studied on AAA cannot be discussed thoroughly without characterization of the vortices in the flow field. Several studies show that the vortex ring dominates the flow in most of the cycle. These reasons bring the requirement to understand how a vortex ring evolves in a AAA case. For this purpose, an experimental setup is designed and established to simulate physiological flow patterns. Flow field and pressure waveforms are obtained by using Particle Image Velocimetry (PIV) and pressure measurements from transducers, respectively.

The present study aims to apply different methods to identify vortices and extract detailed information about their evolution by taking PIV measurements for different flow patterns. To achieve this aim, one steady flow and two physiological flow patterns with different periods are studied. The evolution of vortex ring in physiological flow patterns is studied in detail by implementing vortex identification methods. Different vortex identification methods; λ_{ci} - criterion, Q - criterion, Δ - criterion and λ_2 - criterion are reviewed. Moreover, a comparison is made between them for both steady and physiological flow patterns. After that, λ_{ci} - criterion is applied to characterize the vortex rings at some specific phases of cycles. The post-process of the results is done by a MATLAB code that is developed for this study. This code calculates the required parameters of mentioned vortex identification methods to identify vortices from planar PIV measurements. Since planar PIV measurements may contain measurement errors due to experimental conditions on the complex spatial distributions of vortices, some methods are also applied to obtain more robust results.

1.2 The Outline of the Thesis

The thesis consists of five main chapters.

The first chapter is the introduction. The definition of abdominal aortic aneurysm, its possible reasons and effects on health are discussed. In addition to that, the possible effects of flow field on AAA are examined. Lastly in this chapter, the aim and the motivation of this study is explained.

The second chapter is about the literature survey on this topic. Hemodynamics and blood mimicking fluids are explained. The flow parameters appear on AAA studies, especially vortex detection methods are introduced, and then the flow field in AAA geometries under different flow conditions are described.

The third chapter covers the design of the experimental setup and measurement techniques used in this study. The experimental matrix is presented. Moreover, data processing and post-processing steps are explained.

The fourth chapter includes the results of the experiments. PIV measurements of experiment matrices and vortex ring characterization are discussed in this part in a very detailed manner.

The last chapter is the conclusion that emphasizes the critical findings of this study with future work suggestions.

CHAPTER 2

LITERATURE REVIEW

This chapter includes an extensive summary of studies on AAA, a general description hemodynamic, experimental setup concerns, and a review of vortex identification methods.

2.1 Hemodynamics

Hemodynamics is the field that studies blood flow dynamics. Blood consists of plasma, red cells, white cells, platelets and other proteins. This complex mixture makes it nearly impossible to mimic realistic blood. Red blood cells become prominent in the case of hemodynamics. Hematocrit is defined as the ratio of red blood cell volume ratio by percent in blood, and it is not the same for every person. This situation results in different blood characteristics for any human being. Another vital component of blood in AAA is platelets. Platelets play a major role in thrombus formation, which occurs due to an unexpected change in blood flow. If the artery is damaged structurally, platelets start to form blood clots to stop the bleeding. Although it is a behavior of human immune system, it can be dangerous in certain situations when it is undesired. The clot formation may block the blood flow and completely change the flow characteristics inside an artery.

The blood flow in arteries can be thought of as a superposition of a steady flow and pulsatile flow. Therefore, it should be considered in two different aspects; rheology and physiological [12]. Rheological parameters of blood are extracted under steady flow conditions. Hence, kinematic or dynamic viscosity is studied under the rheological aspect. There are various studies to report viscosity and density of the

blood differently. Generally, the dynamic viscosity of the blood is accepted as 3.5 cp. For high shear rates between 94.5 – 400 s^{-1}, the dynamic viscosity of the blood is 4.4 ± 0.6 cP [13]. Blood density is around 1060 kg/m^3. Blood shows Newtonian characteristics in arteries with a diameter larger than 0.5 mm [14]. However, if the shear rate is lower than 50 s^{-1}, non-Newtonian characteristics start to be seen since large aggregates of red blood cells start to form [15]. Considering the existence of a vortex ring in an AAA, the shear rate distribution can be said to be highly nonhomogeneous. Non-Newtonian characteristics of the blood may have effect on the vortex structures. The exact effect on this Newtonian assumption is not apparent in the literature yet.

Physiological aspect of blood results in an oscillatory behavior of viscosity and elasticity which can be combined in complex viscosity context.

$$\eta = \eta' - i\eta''$$

The above formulation shows the complex viscosity where η' is the oscillatory viscosity and η'' is the oscillatory elasticity. Oscillatory viscosity represents the dissipated energy meanwhile oscillatory elasticity is the recovered energy. These parameters become important in non-Newtonian considerations of the blood flow. The viscoelastic behavior of the human blood can be seen in Figure 2.1. At lower shear rates, viscosity is decreasing as the shear rate increases. The elasticity decreases more rapidly compared to viscosity.

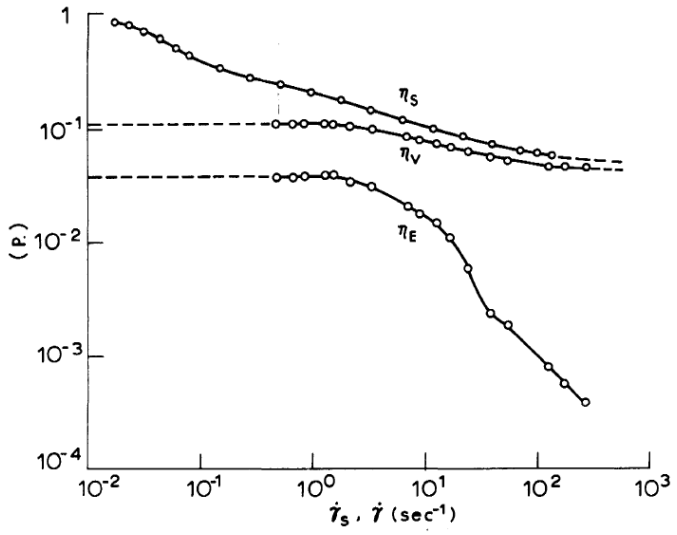

Figure 2.1: The change of steady flow viscosity with respect to shear rate with viscous and elastic parts of complex viscoelasticity [12]

A typical wave form flow rate and Re in the abdominal is given in Figure 2.2. Generally, mean Re is 300 for a typical flow rate in abdominal artery [16]. Mean Re is calculated from time average velocity at the inlet of the artery. The peak flow rate point just before label ‘C’ is identified as the peak systole. The flow starts to decelerate after the peak systole and diastole starts with no such a dramatic change in flow rate. There are only gradual changes in diastole regime which starts after the peak systole.

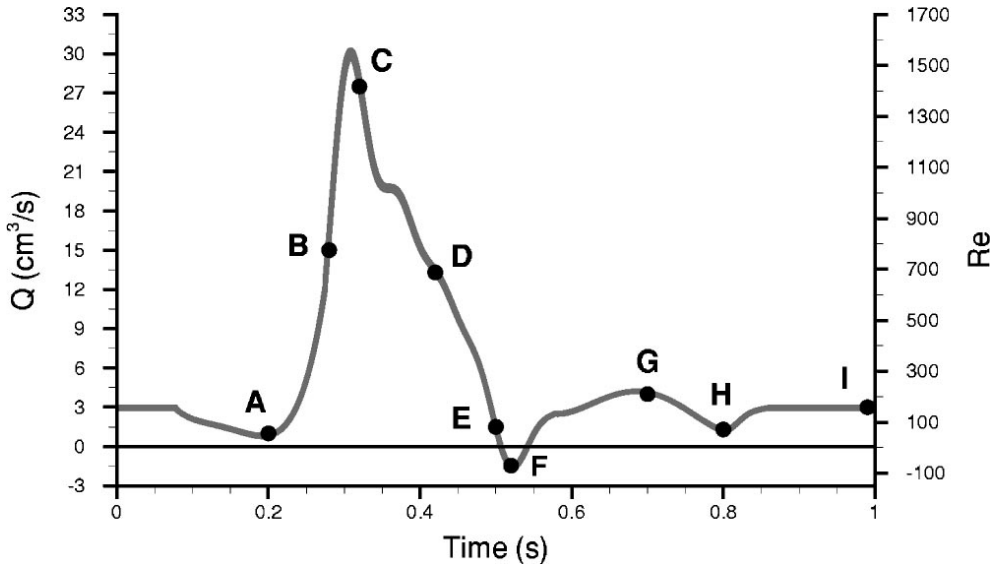

Figure 2.2: A typical pulsatile flow pattern through abdominal aorta [16]

The mean pressure of the blood flow coming out of cardiac vales is around 80 mm Hg [3]. This mean pressure value does not remain constant as it flows through different arteries since it is damped depending on the time.

2.2 Blood Mimicking Fluid and Phantom Production

Blood mimicking fluid selection is made based on the phantom model of an experimental setup. Since they are related processes, they are discussed together in this part.

The selection and preparation of a blood mimicking fluid for a hemodynamics study is not very straightforward and easy because there are different parameters to consider. Considering the flow physics only, the density and the viscosity of the working fluid are the important parameters to simulate the Reynolds number and Womersley number variation occurring in a human artery. Preparing a mixture with viscosity characteristics matching perfectly with human blood is very hard due to its shear-thinning non-Newtonian behavior for a shear rate range.

Other than the flow parameters, safety and the optical characteristics of the working fluid matter for PIV experiments of internal flows. The fluid is in contact with various experimental apparatus, and it should not react with the materials because such chemical interactions may lead to the change in the color of the fluid, the refractive index, viscosity, density and so on. Moreover, these reactions can cause rust to occur. These small rust particles may mix to the flow and they may block the flow through fittings and eventually break these fittings. The refractive index plays a significant role in PIV experiments since it is an optical measurement technique. The refraction of light is governed by Snell's Law. As the refractive index difference of two mediums increases, the refraction angle with respect to the surface normal direction increases. The orientation of camera may not be appropriate in such a case. The lens plane must be perfectly parallel to the image plane in 2D PIV. Moreover, the laser plane may be shifted from the calculated plane, or it may be tilted. To have the best possible resolution and accuracy of PIV images, the values of RI for all the experimental equipment's materials that laser travel through must be the same. This brings a major criterion that RI of the working fluid and the vessel material must be close as possible. RI match will also result in minimum reflection the vessel walls so that PIV image quality is not affected considerably. In the case of intense reflection on the walls of the vessel, some of the seeding particles may not be seen vicinity of the walls. This will cause difficulties in wall shear stress measurement from PIV. Moreover, if a small-scale vortex structure exists very close to the vortex or maybe interacting with the wall, the details of such an event may not be captured in fine enough details. The effect of RI match between the fluid and the vessel can be seen in Figure 2.3. Even a slight difference such as 0.003 can cause high visibility of the vessel.

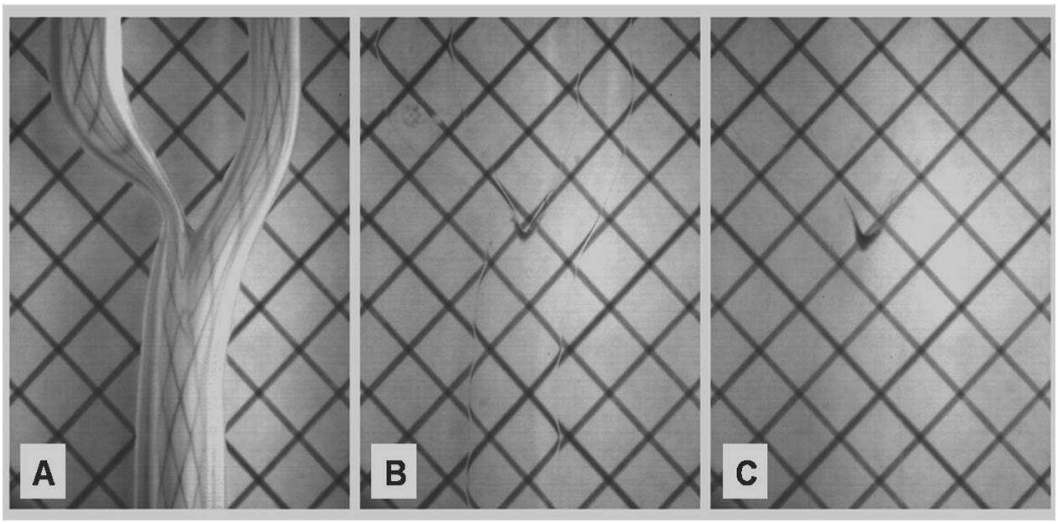

Figure 2.3: The effect of refractive index match on optical access, a) no match b) near match with 0.003 difference c) match [13]

There are two main material types used in experimental AAA studies for vessel production; silicon elastomers and glass. Silicon elastomer-based materials, such as Sylgard184 provide considerable advantage. Sylgard184 is a two-component silicone elastomer. The most prominent advantage of it is the availability to produce complex geometries with the help of molds and elastic walls as adjusting the thickness throughout the mold. The male mold part is the lumen of the vessel. After the production, it must be removed out mechanically or with an alternative method. Since removing it out mechanically is a sensitive process that needs intense care to preserve the internal smoothness, other methods should be chosen if possible. One of the prevalent methods is to use a water solvable 3D printing resin in male mold formation. It can be removed easily. If the desired geometry is patient specific, a female mold must be designed carefully to adjust the thickness of the real geometry of AAA of the patient. If elasticity is not going to be studied, this male mold can be placed in a rigid box to form the walls of vessel geometry as in Figure 2.4. Sylgard184 have the refractive index of 1.414 under this wavelength and this value can be accepted a low one so preparing a mixture with this RI is relatively simple compared to glass case.

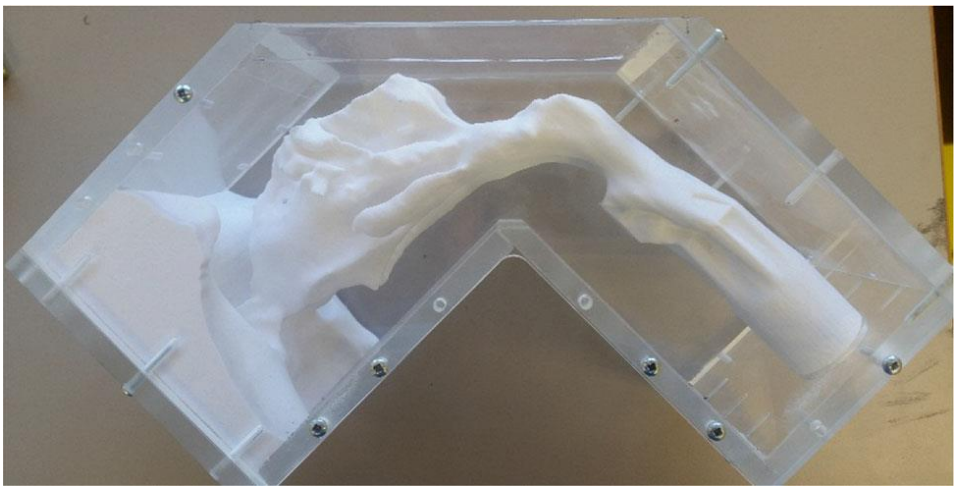

Figure 2.4: The lumen made from 3D printing inside a box [17]

Glass is very cheap compared to silicone elastomers, but it has some major disadvantages. These disadvantages require strict design criteria of the experimental setup. A vessel geometry made from glass must be fixed on another component, a box. This situation gives rise to the necessity of RI match between the fluid filling the space between the box and the phantom with the working fluid itself. Here, it should be noted that RI of the suitable glass types is higher than silicon elastomers, so preparing a working fluid is a more challenging process in comparison. Moreover, glass is a fragile material that must be handled carefully through experiments. Pyrex glass and fused quartz glass are the best two options for glass materials. RI of these types of glasses was measured in Şişecam Company by using Abbe Refractometer under 589 nm wavelength. The RI of fused quartz was found as 1.4590. Meanwhile, RI of pyrex glass is found as 1.470. Glass is only suitable to produce simplified phantoms. Simplified phantoms are characterized by three dimensions D, d and L as seen in Figure 2.5. Different D/d and L/d ratios can be combined to investigate the fundamental flow characteristics. Nonetheless, glass is a good option to investigate fundamental flow characteristics in a physiological flow pattern so physics of the problem can be studied.

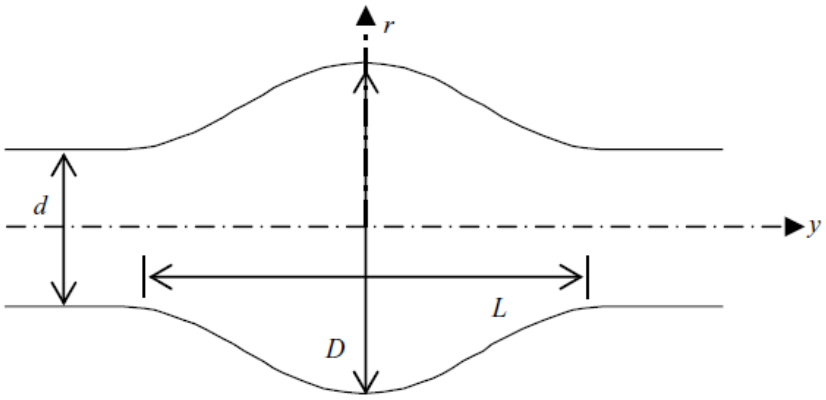

Figure 2.5: Simplified AAA phantom characterized by three dimensions; L, D and d [18]

The first step in preparing blood mimicking fluid is to decide if the working fluid will be Newtonian or non-Newtonian. For all kinds of Newtonian mixtures, Xanthan gum (XG) is the material that is added to all Newtonian solutions to obtain a non-Newtonian fluid. Xanthan gum is originally a food additive made from sugar-type material to thicken or stabilize the food.

Water and glycerin are the base components of a blood mimicking fluid. Glycerin is used to achieve the desired viscosity. Considering glass, RI of water and glycerin mixture must be increased with an additive. The reason of this is that RI of glycerin, the component with the higher RI, is around 1.47, which is RI of pyrex glass. Using glycerin only results in unreasonably high viscosity. Hence, it can be said that matching RI of glass with a mixture of water and glycerin is impossible. Sodium iodide (NaI) is the most commonly used salt to increase the RI to match with glass type material. The most prominent disadvantage of NaI is its high price. Other than that, it increases the density of the mixture [19]. It is observed that NaI gives the water - glycerin solution a pinkish color as in Figure 2.6. Adding a tiny amount of sodium thiosulfate ($Na_2S_2O_3$) will neutralize this color effect to obtain a transparent liquid. Adding NaI to water and glycerin-based Newtonian fluid does not change its viscosity, but it affects if the mixture is non-Newtonian [20]. Sodium thiocyanide

(NaSCN) is a cheaper alternative to NaI with nearly having the same effects on water and glycerin mixtures [20]. It has some unavoidable drawbacks. They are explained in the working fluid section under the experimental setup title since it is used in this study.

Figure 2.6: Pinkish color of NaI solution

The variation of kinematic viscosity of blood mimicking fluids prepared with NaI or NaSCN as with the additive of XG is shown in Figure 2.7. It is obvious that a perfect match is not possible. Adding more NaSCN results in a similar behavior in kinematic viscosity with the actual blood at lower shear rates. However, as the shear rates increase, the resulting viscosity values are higher. A high viscosity value will limit Re, so it may be undesired.

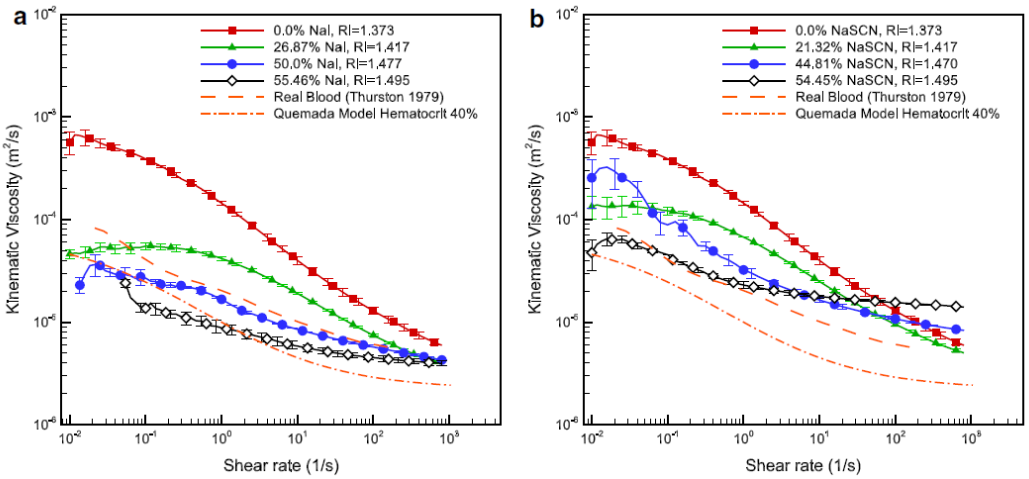

Figure 2.7: Variation of kinematic viscosity with respect to shear rate for real blood and some common blood mimicking fluids with their RI [20]

Recently, urea is suggested as a cheaper and safer alternative to these salts to increase RI of the mixture while increasing the density of the mixture lesser, which is an advantage. Urea is safer as it is not reactive as the other mentioned salts. Moreover, it does not increase the density of the mixture as high as the other. Figure 2.8 shows that urea increases the refractive index as effectively as the other additives while not increasing the density considerably which is advantageous.

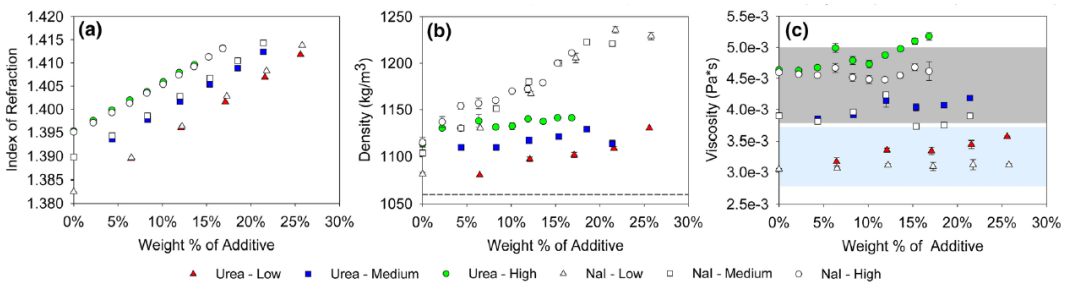

Figure 2.8: Change in RI, density and viscosity with respect to percentage of different additives [19]

2.3 Parameters to be Considered for AAA

There are various flow related parameters for AAA cases, including Eulerian or Lagrangian properties or different WSS parameters occurring due to oscillations. However, Reynolds number, Womersley number and vortex related parameters are focused on in this work. Reynolds number for AAA studies can be calculated as in Equation (2.1).

$$Re = \frac{u_m d}{v} \tag{2.1}$$

Where:

u_m: mean velocity calculated from flow rate [m/s]

d: diameter of the inlet pipe [m]

v: the kinematic viscosity [m^2/s]

Since the flow in arteries in unsteady and periodic, Womersley number becomes important. It indicates the ratio of unsteady inertial forces to viscous forces and shown in Equation (2.2).

$$\alpha = \frac{d}{2}\sqrt{\frac{\omega}{v}} \tag{2.2}$$

Where:

d: diameter of the inlet pipe [m]

v: the kinematic viscosity [m^2/s]

ω: angular frequency [rad/s]

Womersley number affects the velocity profile in a pipe flow considerably. Depending on its magnitude, the flatness or the curvature the parabolic profile changes. As Womersley number increases, the temporal changes in the velocity becomes steeper. The typical Womersley number for the abdominal artery is 12 [21].

2.3.1 Vortex Structures and Identification Methods

Vortex structures are studied extensively in fluid mechanics as they provide essential information about the flow field and flow field classification. They are one of the characteristics turbulent flows, but they are seen in laminar flows as well. In turbulent flows, they are coherent structures of a flow field. The coherent structures can be defined as some specific flow pattern that have a role in transport of flow properties. This effect on transport reveals itself as effective mixing processes of flow parameters due to vortices. These structures can be studied to developed turbulence modeling methods. Considering these, vortex identification methods are constructed with the aim of revealing the details of turbulence, flow control mechanisms or other flow quantities of interest depending on the specific problem.

There is no globally accepted definition of vortex. Different methods are being applied to flow fields to identify vortices. These methods can be grouped under different ways depending on how they address the question such as Eulerian and Lagrangian methods or local and non-local methods. Eulerian-based methods are based on Eulerian quantities in which the flow field is investigated from an observer that is following a fluid particle as it moves in space and time. Velocity gradient tensor is used in many of the Eulerian-based methods, which is a three by three matrix in a real flow problem in three dimensions. On the other hand, Lagrangian-based methods are based on Lagrangian description of flow in which the observer investigates specific regions and the fluid particles passing through in these regions such as pathlines. Local methods work in a point by point method, meaning that every point in flow field is studied on to extract information about the vortical

motion. Non-local methods investigate the entire flow field. Closed or spiraling streamline pattern is the most popular non-local approach to identify vortices.

Although each vortex identification method has some unique requirements, there are several conditions for well-defined and structured methods. The method should be independent of the frame of reference of the observer. In the case of translational motion with no acceleration and static rotation, this is called Galilean invariance. As it will be discussed later, most of the Eulerian based methods depend on calculation of a quantity from the velocity gradient tensor and a threshold is required. The threshold selection should not be arbitrary since there is no priori information about the vortices [22]. Moreover, for data sets with measurement errors such as PIV results, a method should give robust results and tolerate measurement errors [23].

In this case, the main focus is on understanding the flow field. As mentioned before, the vortices have major role in thrombus formation locations and so on the growth and rupture of AAA cases. Moreover, they are applied to planar PIV measurements to evaluate their performance in this work and for comparison. Lastly, some methods are applied to reduce noise and to obtain smooth data. It should be mentioned that; the focus is on some of the most popular local Eulerian based methods in this work.

2.3.2 Based on Streamlines

Streamline patterns can be investigated to identify the vortex structures and it may be the most straightforward method among with the vorticity magnitude approach. This method is a non-local Eulerian approach. In a frame of reference that is moving with the core of the vortex, if the streamlines are mapped onto normal plane of the vortex and the resulting streamlines are showing a closed or spiraling geometry, that region can be said to be a vortex [24]. This approach has a critical issue since it requires prior knowledge about the vortex core. Furthermore, streamlines are not Galilean invariant meaning that a vortex structure can be seen very differently from different frame of references. For example; an elliptic vortex can be identified as a

circular vortex in an arbitrary coordinate system. As seen in Figure 2.9, a vortex ring occurring from a rolling shear layer due to discontinuity of the jet flow can be seen very differently from different frames of reference. If the coordinate system is placed out of the vortex core, a hill-like pattern can be seen.

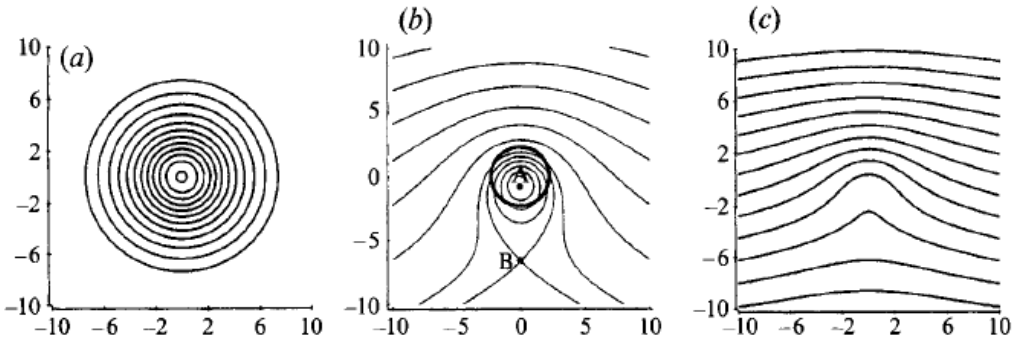

Figure 2.9: Streamline patterns of axisymmetric vortex ring from different coordinate systems, a) From vortex core b) a point inside the vortex c) out of vortex [25]

2.3.3 Vorticity Magnitude, ω

Vorticity is one of the most commonly used Eulerian-based local methods, which is the curl of the velocity and physically it is twice the angular rotation rate. Vorticity tensor, which is an antisymmetric tensor, is analyzed in many of the fluid problems in the context of the vortex. A classical approach to identify vortical structures by selecting a threshold of vorticity magnitude, and define regions where the vorticity magnitude is higher than the threshold as vortex. The next step can be finding the location with the highest value to locate the center of the vortex. In a planar flow field in xy-plane, the vorticity can be calculated only in the out of plane direction as shown in Equation (2.3).

$$\omega_z = \frac{\partial v}{\partial x} - \frac{\partial u}{\partial y} \tag{2.3}$$

There are some substantial disadvantages of applying vorticity threshold to identify the vortex structures. The most important one is that vorticity magnitude does not differentiate the swirling motion and shear layers. Shear layers have high vorticity magnitude due to large gradients existing, but they are physically defined vortex structures. A shear layer and a vortex ring may be existing in the flow field and vorticity magnitude approach may fail to distinguish these two. Considering the flow physics in this study where shear layer and vortex structures dominate the flow in a closed area, the vorticity magnitude may be a problematic approach. Nonetheless, it may provide information about shear layers that rolls up to vortex ring as mentioned before, or it can show the sense of rotation of vortex structures. Another disadvantage comes from threshold selection criteria. The maximum vorticity may lead to wrong selections since it can be observed in non-vortex regions. For example, the highest vorticity magnitude can be observed on the surface of the cylinder in a flow over cylinder problem. Lastly, vorticity depends on the coordinate system since angular velocity will change depending on the observer's coordinate system.

2.3.4 Δ - Criterion

Although a couple of different methods will be reviewed, they have noticeable common points. Considering this fact, this criterion is selected as the base method to review other methods as well. A typical approach is explained here in detail. The other methods are explained by their unique approaches. Critical points are defined in mathematics while dealing with differential equations and they are the points that make the derivative of the function zero or make the function non-differentiable. This is a start point to find the solution sets of differentiable equations in fluid mechanics and the solution set consists of possible flow trajectories. In context of fluid mechanics, critical points refer to the stagnation points where all velocity components are zero. This means that the streamline passing through that point has an indefinite slope. To do that, Taylor series expansion around a point can be used

to write the differential equation of a fluid particle with respect to that point as in Equation (2.4).

$$\frac{d\vec{x}}{dt} = \nabla\vec{u} \cdot \vec{x} \tag{2.4}$$

The first term on the right-hand side is the velocity gradient tensor and it's 3x3 in a 3D flow field, and it's a 2x2 matrix in a planar flow field. The eigenvalues of this matrix can be found by extracting the characteristic equation of it as displayed in Equation (2.5).

$$det\left[\frac{\partial u_i}{\partial x_j} - \lambda I\right] = 0 \tag{2.5}$$

The solution of the above equation will give the eigenvalues, and the corresponding eigenvectors of each eigenvalue can be found. 3D VGT can be written as a matrix in Equation (2.6).

$$\frac{\partial u_i}{\partial x_j} = \begin{bmatrix} \frac{\partial u}{\partial x} & \frac{\partial u}{\partial y} & \frac{\partial u}{\partial z} \\ \frac{\partial v}{\partial x} & \frac{\partial v}{\partial y} & \frac{\partial v}{\partial z} \\ \frac{\partial w}{\partial x} & \frac{\partial w}{\partial y} & \frac{\partial w}{\partial z} \end{bmatrix} \tag{2.6}$$

The characteristic equation of this matrix is a third order polynomial as shown in Equation (2.7).

$$\lambda^3 + P\lambda^2 + Q\lambda + R = 0 \tag{2.7}$$

P, Q and R are the invariants of the VGT, meaning that they do not depend on the coordinate system. The eigenvalues and invariants appear frequently in the vortex identification methods that are going to be reviewed in this study. Now, a study of a 2D matrix can be done here instead of 3D to understand the typical approach.

Moreover, since planar PIV measurements are taken in this study, 2D matrix will be used. The velocity gradient matrix in a 2D planar flow can be written as in Equation (2.8).

$$\frac{\partial u_i}{\partial x_j} = \begin{bmatrix} \frac{\partial u}{\partial x} & \frac{\partial u}{\partial y} \\ \frac{\partial v}{\partial x} & \frac{\partial v}{\partial y} \end{bmatrix} \tag{2.8}$$

The characteristic equation of such a second order polynomial can be found by following the steps.

$$\left(\frac{\partial u}{\partial x} - \lambda\right)\left(\frac{\partial v}{\partial y} - \lambda\right) - \frac{\partial u}{\partial y}\frac{\partial v}{\partial x} = 0$$

$$\lambda^2 + \lambda\left(-\frac{\partial u}{\partial x} - \frac{\partial v}{\partial y}\right) + \frac{\partial u}{\partial x}\frac{\partial v}{\partial y} - \frac{\partial u}{\partial y}\frac{\partial v}{\partial x} = 0$$

$$\lambda^2 + P\lambda + R = 0$$

Where:

$$P = -\frac{\partial u}{\partial x} - \frac{\partial v}{\partial y}$$

$$R = \frac{\partial u}{\partial x}\frac{\partial v}{\partial y} - \frac{\partial u}{\partial y}\frac{\partial v}{\partial x}$$

P and R are the invariants of this matrix. Compared to 3D, there are only two invariants here, with Q is absent. The discriminant of this equation can be found as below, and the discriminant depends on P and R as in Equation (2.9).

$$\Delta = \left(\frac{\partial u}{\partial x} + \frac{\partial v}{\partial y}\right)^2 - 4\left(\frac{\partial u}{\partial x}\frac{\partial v}{\partial y} - \frac{\partial u}{\partial y}\frac{\partial v}{\partial x}\right) \tag{2.9}$$

Where:

$$\Delta = P^2 - 4R$$

If this discriminant value is positive, it has two real eigenvalues. Meanwhile, if it is negative, it has one complex conjugate pair solution. These eigenvalues can be written in complex form as shown in Equation (2.10).

$$\lambda_{1,2} = \lambda_{cr} \pm i\lambda_{ci} \tag{2.10}$$

These complex eigenvalues mean that the streamlines are spiraling or closed so that the corresponding region is a vortex [26]. Zero is the theoretical threshold, but depending on the problem, a small positive number should be used. The same approach can be followed for 3D VGT. This method also needs a threshold to identify realistic vortices. There is not a particular method to determine this threshold. It should be studied for the specific problem.

2.3.5 Q - Criterion

Q-criterion is simply the second invariant, Q, of the 3D VGT. How it determines if a region is vortex or not comes in sight while characterizing the flow events as streaming, eddy and convergence zones [27]. As turbulent flows consist of coherent structures, their effect on the flow properties should be understood in detail to have a better understanding of general turbulent flows. Convergence zones are the regions of straining motion of the flow without rotation. Streaming zones are regions where the fluid particles follow a nearly straight curve. It can be said that jet flow regions where the accumulation of the fluid particles tends to be transported in the domain are streaming zones. Eddy zones correspond to the vortex regions where the rotational swirling motion is dominant over the straining motion. There are two criteria to identify these eddy zones. The first one is that the vorticity of the flow

must be higher than the irrotational straining in a position. The second criterion is that the pressure in a region must be smaller than the pressure at the environment. This additional criterion is generally disregarded. It ensures to identify the vortex regions in a rotational flow by ensuring that the streamlines are curved due to a pressure gradient. Generally, pressure minimum exists at these locations [25]. The physical reasoning of Q invariant can be displayed if it is written in Frobenius norm by using strain rate and vorticity tensors as shown in Equation (2.11).

$$Q = \frac{1}{2}(\|\Omega\|^2 - \|S\|^2) \tag{2.11}$$

It can be seen that Q is a local measure of the difference between the vorticity motion and straining. This definition can be used to identify the vortex regions where Q is larger than zero. It was displayed that Q invariant does not exist for 2D. However, the definition of Q for 3D VGT can be used here to find Q for 2D by using Frobenius norm.

For 2D VGT;

$$\Omega = \frac{1}{2}\begin{bmatrix} 0 & \frac{\partial u}{\partial y} - \frac{\partial v}{\partial x} \\ \frac{\partial v}{\partial x} - \frac{\partial u}{\partial y} & 0 \end{bmatrix}$$

$$S = \frac{1}{2}\begin{bmatrix} 2\frac{\partial u}{\partial x} & \frac{\partial u}{\partial y} + \frac{\partial v}{\partial x} \\ \frac{\partial v}{\partial x} + \frac{\partial u}{\partial y} & 2\frac{\partial v}{\partial y} \end{bmatrix}$$

$$\|\Omega\| = \sqrt{\left(\frac{1}{2}(\frac{\partial u}{\partial y} - \frac{\partial v}{\partial x})\right)^2 + \left(\frac{1}{2}(\frac{\partial v}{\partial x} - \frac{\partial u}{\partial y})\right)^2} = \sqrt{\frac{1}{2}\left(\frac{\partial u}{\partial y}\right)^2 + \frac{1}{2}\left(\frac{\partial v}{\partial x}\right)^2 - \frac{\partial u}{\partial y}\frac{\partial v}{\partial x}}$$

$$\|S\| = \sqrt{\left(\frac{1}{2}\left(\frac{\partial u}{\partial y}+\frac{\partial v}{\partial x}\right)\right)^2+\left(\frac{1}{2}\left(\frac{\partial v}{\partial x}+\frac{\partial u}{\partial y}\right)\right)^2+\left(\frac{\partial u}{\partial x}\right)^2+\left(\frac{\partial v}{\partial y}\right)^2}$$

$$= \sqrt{\frac{1}{2}\left(\frac{\partial u}{\partial y}\right)^2+\frac{1}{2}\left(\frac{\partial v}{\partial x}\right)^2+\frac{\partial u}{\partial y}\frac{\partial v}{\partial x}+\frac{1}{2}\left(\frac{\partial u}{\partial x}\right)^2+\frac{1}{2}\left(\frac{\partial v}{\partial y}\right)^2}$$

$$\|\Omega\|^2 = \frac{1}{2}\left(\frac{\partial u}{\partial y}\right)^2+\frac{1}{2}\left(\frac{\partial v}{\partial x}\right)^2-\frac{\partial u}{\partial y}\frac{\partial v}{\partial x}$$

$$\|S\|^2 = \frac{1}{2}\left(\frac{\partial u}{\partial y}\right)^2+\frac{1}{2}\left(\frac{\partial v}{\partial x}\right)^2+\frac{\partial u}{\partial y}\frac{\partial v}{\partial x}+\left(\frac{\partial u}{\partial x}\right)^2+\left(\frac{\partial v}{\partial y}\right)^2$$

Plugging in the calculated variables results in the definition of Q-criterion in planar flows as shown in Equation (2.12).

$$Q = \frac{1}{2}(\|\Omega\|^2-\|S\|^2) = -\frac{\partial u}{\partial y}\frac{\partial v}{\partial x}-\frac{1}{2}\left(\frac{\partial u}{\partial x}\right)^2-\frac{1}{2}\left(\frac{\partial v}{\partial y}\right)^2 \qquad (2.12)$$

If Q is larger than zero, that region is identified as a vortex. Q>0 condition is equal to the Δ criterion in general. However, if the vortex is straining in the parallel direction of the core, Q - criterion gives better results [27].

2.3.6 Swirling Strength, λ_{ci}

This method is derived from hairpin vortex structures by using direct numerical solution [28]. The starting point of vortex identification process is the critical point theory just like Δ - criterion. In Δ - criterion, it is stated that complex eigenvalues indicate vortices. This method defines the intensity of the vortical motion based on the magnitude of the complex eigenvalue. The VGT can be decomposed with the help of diagonalization by using eigenvalues and eigenvectors. In 2D, it can be done as in (2.13).

$$\frac{\partial u_i}{\partial x_j} = [v_{cr} \quad v_{ci}] \begin{bmatrix} \lambda_{cr} & \lambda_{ci} \\ -\lambda_{ci} & \lambda_{cr} \end{bmatrix} [v_{cr} \quad v_{ci}]^{-1} \tag{2.13}$$

λ_{cr} and λ_{ci} correspond to real and imaginary parts of the complex eigenvalues, respectively. Their eigenvectors are shown with v. The solution of the streamline patterns is shown in Equation (2.14).

$$\begin{aligned} y_1(t) &= e^{\lambda_{cr} t}\left[{C_c}^1 \cos(\lambda_{ci} t) + {C_c}^2 \sin(\lambda_{ci} t)\right] \\ y_2(t) &= e^{\lambda_{cr} t}\left[{C_c}^2 \cos(\lambda_{ci} t) - {C_c}^1 \sin(\lambda_{ci} t)\right] \end{aligned} \tag{2.14}$$

The solution equations state that if the complex eigenvalue is negative at a point in flow field, the magnitude of it determines the intensity of the swirling motion since eigenvalue appears as a coefficient for sinusoidal and cosine terms of the solution set. Swirling motion occurs at a plane that is spanned by the eigenvectors of complex eigenvalue. As the complex eigenvalue's magnitude increases, the swirling intensity increases. This approach can be used in 3D matrix in a similar approach. The spiraling motion can be visualized in eigenvector directions as displayed in Figure 2.10.

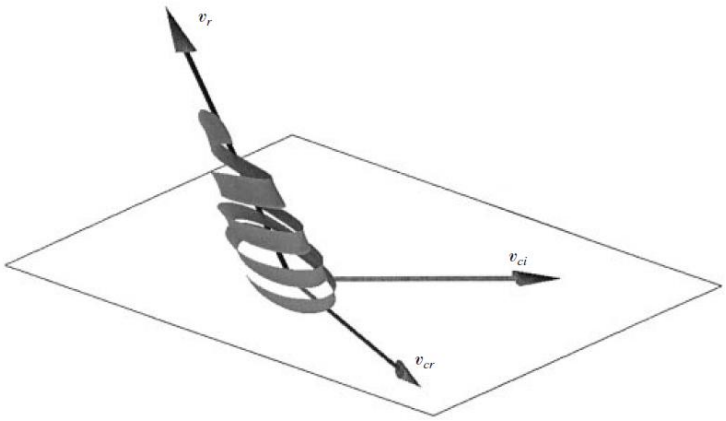

Figure 2.10: Spiraling streamlines on a plane spanned by complex eigenvectors

2.3.7 λ_2 - Criterion

In general, pressure is lower compared to the ambient for a vortex core. This approach is implemented in Q – criterion as well to ensure having curls in a rotational flow. Although pressure minimum cannot be used alone as a criterion, it can be used as a basis to have a new method. Pressure minimum at point in the flow field can occur due to two reasons other than existence of a vortex; unsteady straining and viscous forces [25]. Considering those, a new pressure minimum definition can be made by disregarding these mentioned possible effects. To do that, local maxima of pressure must be obtained. The gradient of the Navier-Stokes equation is needed as it contains information about the pressure minimum. After taking the gradient, it can be divided into symmetric and antisymmetric parts as shown in Equation (2.15).

$$a_{i,j} = \frac{DS_{ij}}{Dt} + \Omega_{ik}\Omega_{kj} + S_{ik}S_{kj} + \frac{D\Omega_{ij}}{Dt} + \Omega_{ik}S_{kj} + S_{ik}\Omega_{kj} \qquad (2.15)$$

In the above equation, the first three terms on the left-hand side compose the symmetric part while the rest is the antisymmetric part, which is actually the vorticity transport equation. The left-hand side equation consists of the gradient of the pressure term and the viscous terms so the symmetric part can be equalized with the

pressure gradient and the viscous straining. If the pressure gradient is left on the one side, the minimum of it can be detected from $S^2 + \Omega^2$ matrix. In 3D, the three eigenvalues of this matrix are ordered in magnitude and the two of them must be negative inside a vortex core as in Equation (2.16). It should be noted that, for planar flows there are two eigenvalues, and the larger one must be negative.

$$\lambda_1 \leq \lambda_2 \leq \lambda_3 \;\; \& \;\; \lambda_2 < 0 \tag{2.16}$$

λ_2 – criterion for planar flows can be seen in Equation (2.17) [29].

$$\lambda_2 = \left(\frac{\partial u}{\partial y}\frac{\partial v}{\partial x} - \frac{\partial u}{\partial x}\frac{\partial v}{\partial y}\right) + \frac{1}{2}\left(\frac{\partial u}{\partial x} + \frac{\partial v}{\partial y}\right)^2 + \frac{1}{2}\left|\frac{\partial u}{\partial x} + \frac{\partial v}{\partial y}\right| \sqrt{\left(\frac{\partial u}{\partial x} + \frac{\partial v}{\partial y}\right)^2 + \left(\frac{\partial u}{\partial y} + \frac{\partial v}{\partial x}\right)^2} \tag{2.17}$$

2.3.8 The Applications of Vortex Identification Methods in 2D

The reviewed vortex identification methods provide the same results when they are applied in planar flow fields [25]. If the criterion of each identification method is investigated, they can be correlated since the theoretical threshold is zero for all of them. For λ_{ci} and Δ criteria, the relation to be satisfied is shown in Equation (2.18). For Q-criterion, the relation can be seen in Equation (2.19). Lastly, the relation that λ_2-criterion must satisfy is shown in Equation (2.20).

$$\left(\frac{\partial u}{\partial x} + \frac{\partial v}{\partial y}\right)^2 < 4\left(\frac{\partial u}{\partial x}\frac{\partial v}{\partial y} - \frac{\partial u}{\partial y}\frac{\partial v}{\partial x}\right) \tag{2.18}$$

$$\left(\frac{\partial u}{\partial x} + \frac{\partial v}{\partial y}\right)^2 < 2\left(\frac{\partial u}{\partial x}\frac{\partial v}{\partial y} - \frac{\partial u}{\partial y}\frac{\partial v}{\partial x}\right) \tag{2.19}$$

$$\frac{1}{2}\left(\frac{\partial u}{\partial x}+\frac{\partial v}{\partial y}\right)^2+\frac{1}{2}\left|\frac{\partial u}{\partial x}+\frac{\partial v}{\partial y}\right|\sqrt{\left(\frac{\partial u}{\partial x}-\frac{\partial v}{\partial y}\right)^2+\left(\frac{\partial u}{\partial x}+\frac{\partial v}{\partial y}\right)^2} < \left(\frac{\partial u}{\partial x}\frac{\partial v}{\partial y}-\frac{\partial u}{\partial y}\frac{\partial v}{\partial x}\right) \quad (2.20)$$

These four relations can be related with one common equation as shown in Equation (2.21).

$$\frac{\partial u}{\partial x}\frac{\partial v}{\partial y}-\frac{\partial u}{\partial y}\frac{\partial v}{\partial x}>0 \quad (2.21)$$

This shows that the application of these methods in 2D datasets will yield qualitatively the same results. These methods are tested for 2D PIV measurements in a wind tunnel under steady flow conditions for comparison. In the comparison, the used threshold was zero. The comparison can be seen in Figure 2.11. The results are the same for Δ - criterion and λ_{ci} - criterion as they detect the same vortices. λ_2 - criterion was observed to be the strictest one. Q - criterion captures more vortices than λ_2 – criterion, and less than Δ - criterion and λ_{ci} - criterion.

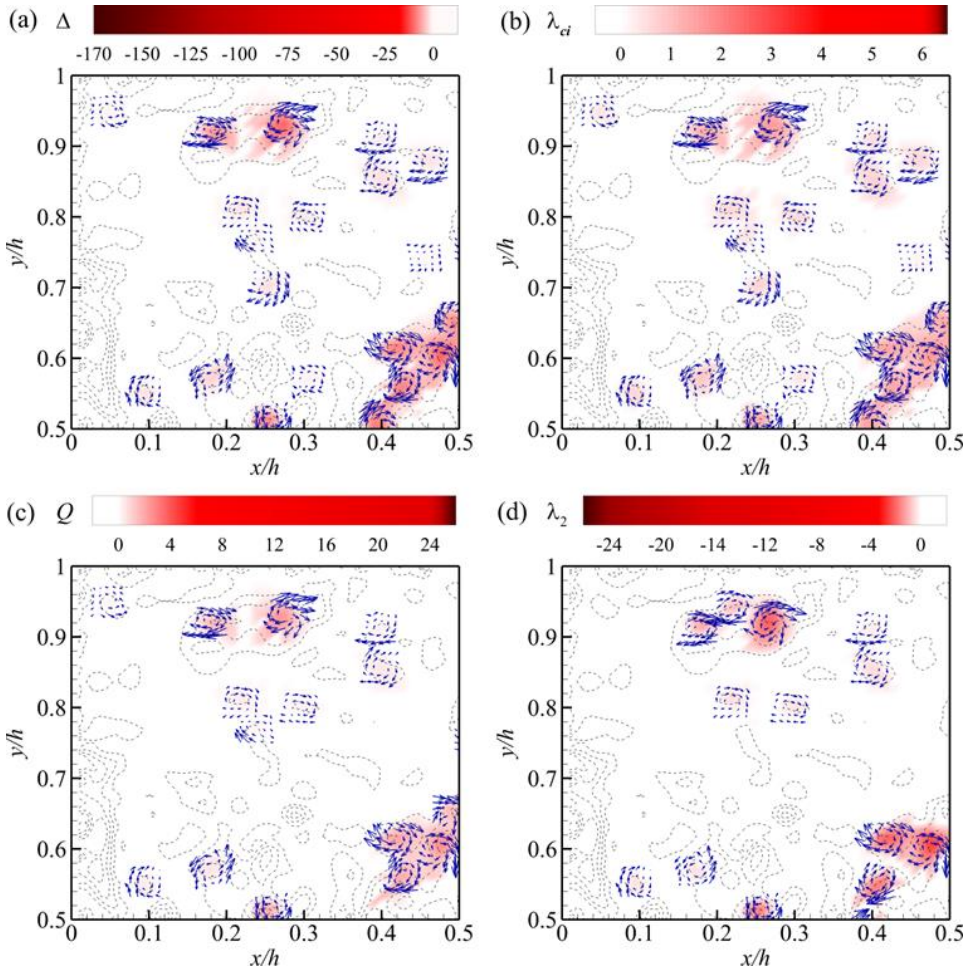

Figure 2.11: The application of reviewed vortex identification methods to planar PIV measurements [29]

2.4 Flow Field

General flow mechanics will be discussed for different conditions. However, they will not be discussed in details as this study also focuses on flow field, especially in vortex structure aspects.

2.4.1 Steady Flow

Under steady-state conditions, the flow field shows some common characteristics for every Re. The recirculation region occupies a significant area in the bulge section. They generally cover the area between the side walls and a virtual line between the inlet and outlet of the same diameter. As Re increases, the core of the vortex ring shifts downstream. Moreover, the magnitude of negative axial velocity values increases. For low Re number around 200, the axial velocity in the centerline decreases about 10% of the inlet value. For the higher Re values around 600, there is no such a drop in the axial velocity [30]. The D/d and L/d ratios have minimal effect on the flow characteristics [31]. A typical steady flow can be seen in Figure 2.12. The jet flow follows straight lines, and recirculation motion dominates the bulge section.

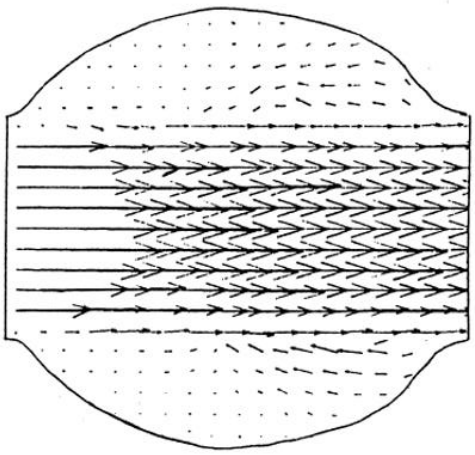

Figure 2.12: Steady flow, Re = 1000 [31]

2.4.2 Physiological Flow

The physiological flow pattern should be studied for different phases of the flow. The critical phase occurs after the peak systole of the physiological pattern. The peak systole refers to maximum flow rate phase of the cycle. After that, deceleration starts, and this results in velocity discontinuity at the outer layers of the jet flow. This is a shear layer of concentrated layer of high vorticity, but it cannot be defined as a vortex yet. This shear layer then rolls up to a vortex ring in the cycle which will evolve as the cycle progresses [32]. Other than this dominant vortex ring, small vortical structures may be observed during some phases of the cycle due Kevin Helmholtz instability [18]. During the acceleration phase, before the peak systole, the flow does not separate from the walls. Since a favorable pressure gradient exists at the beginning of the cycle, the flow does not separate in the diverging part of the bulge as well [18]. Depending on the geometry selection and flow pattern, the characteristics may change, but the flow field can be said to be governed by a vortex ring that is initialized after the deceleration starts. Depending on the local and spatial changes, the vortex can reach to distal end without any interaction with walls or it can collide the walls and vortex ring can break into smaller pieces that eventually die out in the next cycle.

The evolution of a vortex ring can be seen in Figure 2.13. The vortex is initialized after the peak flow rate as a concentrated shear layer region as seen from high vorticity magnitudes [33]. It can be detected as a counter-rotating parts at up and down halves of the bulge in 2D. The vortex ring becomes more distinct as it completely detaches from the wall at further deceleration instant. It travels downstream as the cycle progresses. The vortex ring does not die out in the cycle it is generated, and it collides to the wall at the later cycle. The remaining parts can be observed at the early stages of the cycle.

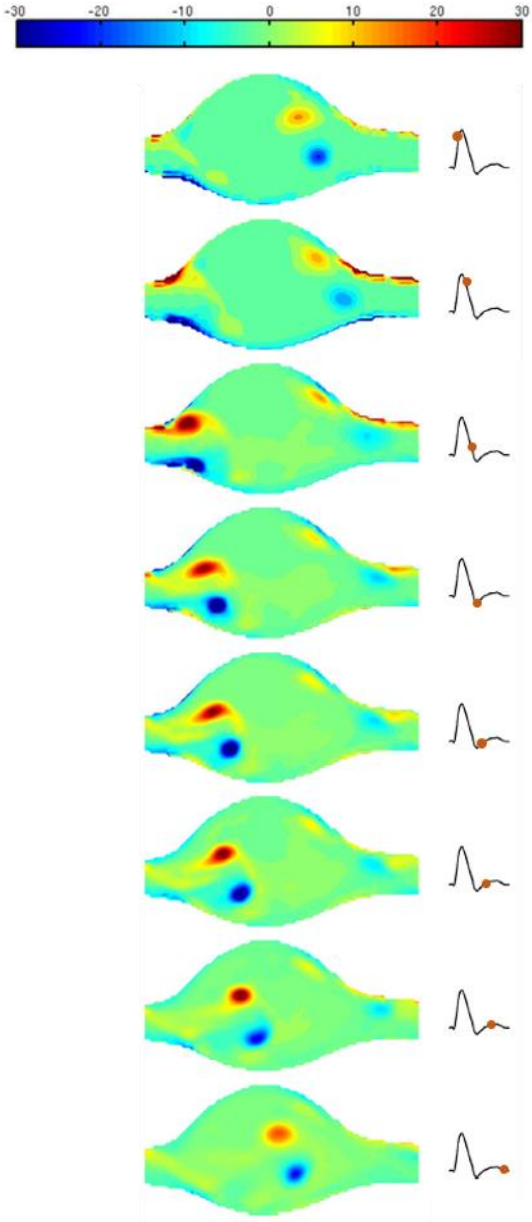

Figure 2.13: Temporal evolution of vorticity for different phases of a physiological flow pattern [33]

Although 2D PIV measurements provide general information about the vortex ring, three-dimensionality of the vortex ring should be studied as well to reveal more information. Temporal evolution of the vortex in 3D can be followed by considering the isosurfaces of swirling strength in Figure 2.14. It can be seen that even if a

symmetric vortex ring is generated after the peak flowrate, the geometrical asymmetry breaks this symmetrical approach [34]. Moreover, vortices are observed at the entrance and exit pipes for certain phases. These certain phases correspond to high flow rates. As the shear stresses increase, they can roll up to form vortices due to Kevin-Helmholtz instability [35].

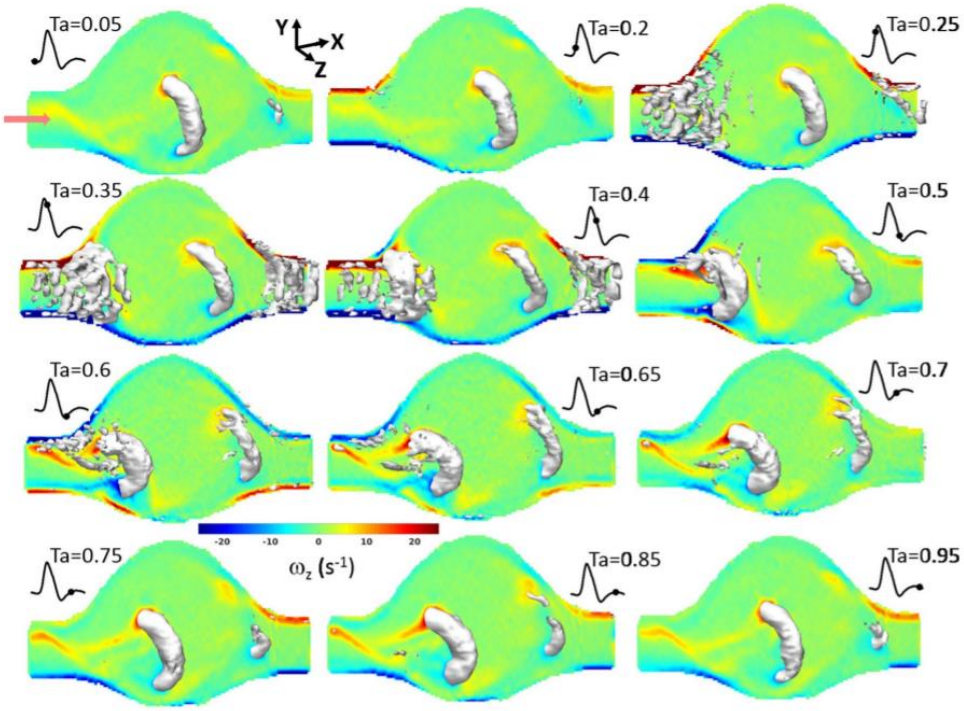

Figure 2.14: Temporal evolution of vorticity and swirling strength for different phases of a physiological flow pattern [34]

As discussed before, Womersley number should be considered in physiological flow patterns to investigate the effect of period. For the same mean Re, flow field is completely different for different Womersley numbers as seen in Figure 2.15. The vortex ring generation mechanism is the same which is the shear layer region occurring just after the deceleration starts. However, the evolution of the vortex is completely different. In the case of higher Womersley number, the shear layer stays attached to the wall for a longer time [36]. This results in a weaker vortex ring with a small size compared to the lower Womersley number case. This may not be valid for flows with very low Womersley number.

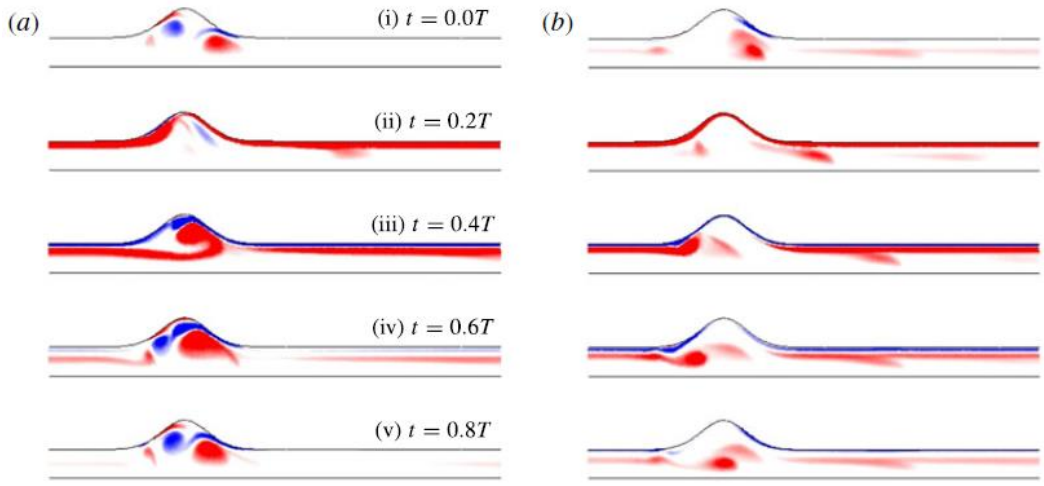

Figure 2.15: The effect of Womersley number on vorticity distribution in a typical pulsatile flow pattern, (a) α=10, (b) α=15 [36]

2.4.3 Compliance Effects

The elasticity of the wall will have an effect on the flow field during the cycle. During the accelerating part of the cycle, the elastic walls will store some of the kinetic energy carried by the flow in potential energy form. This stored energy is released again during the decelerating part from the walls to fluid [32]. Under resting conditions, the vortex appearing mechanism is nearly the same for the rigid and the compliant models but the spatial distribution of the vortex and its intensity will

change. It can be seen that vortex is located far downstream in compliant model compared to the rigid wall model in Figure 2.16. Moreover, the before mentioned effect of the releasing of the stored potential energy in the wall after the peak systole results in a stronger vortex ring in the compliance walls. The displacement of the vortex ring in the flow direction is larger for the compliant walls as well due to this energy gain.

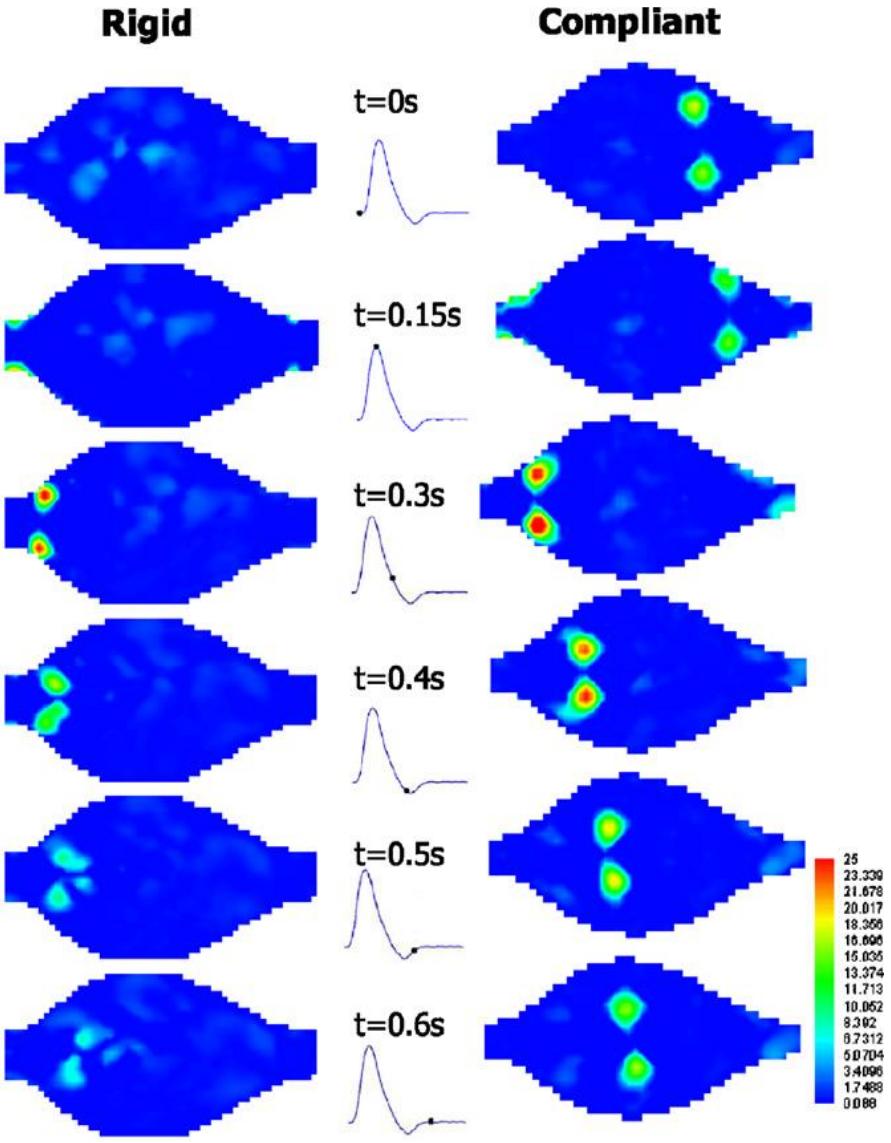

Figure 2.16: Swirling strength distribution for rigid and compliant models in a typical physiological flow pattern [32]

CHAPTER 3

EXPERIMENTAL SETUP AND MEASUREMENT TECHNIQUES

The study was carried out at the Fluid Mechanics Laboratory of Mechanical Engineering Department of Middle East Technical University. The experiment setup is described in detail, and the measurement techniques used in this study are explained with experimental matrices.

3.1 Experimental Setup

The working fluid is contained in a tank made from acrylic glass considering the reactivity of the working fluid. Another advantage of using acrylic glass as the reservoir material is optical access to the tank. It is located above the pump suction level to prevent cavitation at high flow rates. A positive displacement type pump, a gear pump (Dayton 4KHH8, Grainger, Inc., Lake Forest, IL), is used to circulate the flow, with a maximum flow rate of 300 ml/s. The pump was driven by a servo motor (Schneider Electric BMH07002P16A2A) with 2.5 Nm torque and 5500 rpm. The pump base material is bronze, which does not show any reactiveness with the working fluid. An unsteady flow pattern can be provided with this positive displacement type pump easily, so it is very advantageous to simulate a physiological flow pattern. A hose with 12 mm internal diameter is connected to the pipe outlet section to guide the flow. This hose is selected to be stiff so that there would be minimum fluid-structure interaction concerns. A plastic turbine flowmeter is used to measure the flow rate. In general, turbine flowmeters are not adequate to measure instantaneous flow rate in an unsteady flow due to low K factors. K factor shows the number of pulses measured for one volumetric unit of fluid. Although this flowmeter cannot provide the instantaneous flow rates, it takes accurate measurements in steady flows. The material of the turbine flow meter is selected as plastic, considering the

working fluid. There is a 25 cm hose length upstream and downstream of the flowmeter so that the measurement is not affected by changes in geometry as the manufacturer suggested. In physiological experiments, a pressure transducer is placed after the flowmeter. Before turning of the hose in the direction of the vessel, an air-release valve is placed to get rid of the air bubbles in the closed system. This release valve is placed in a higher place compared to the rest of the setup since air bubbles, having lower density, accumulate in the top portions of the hose. After the air release valve, the flow is directed in the vessel. There is another pressure transducer at the beginning of the straight flow portion of the setup before the diameter change in the system. A simple schematic of the experimental setup can be seen in Figure 3.1. It should be noted that PT labels refer to pressure transducers. The mounting of the measurement devices (pressure transducers and flowmeter) was done by using a plastic T-joint connection. Plastic is chosen as the material considering the working fluid as usual. These measurement devices were powered up by using an external power supply unit. Before the experiments, the working fluid is filtered.

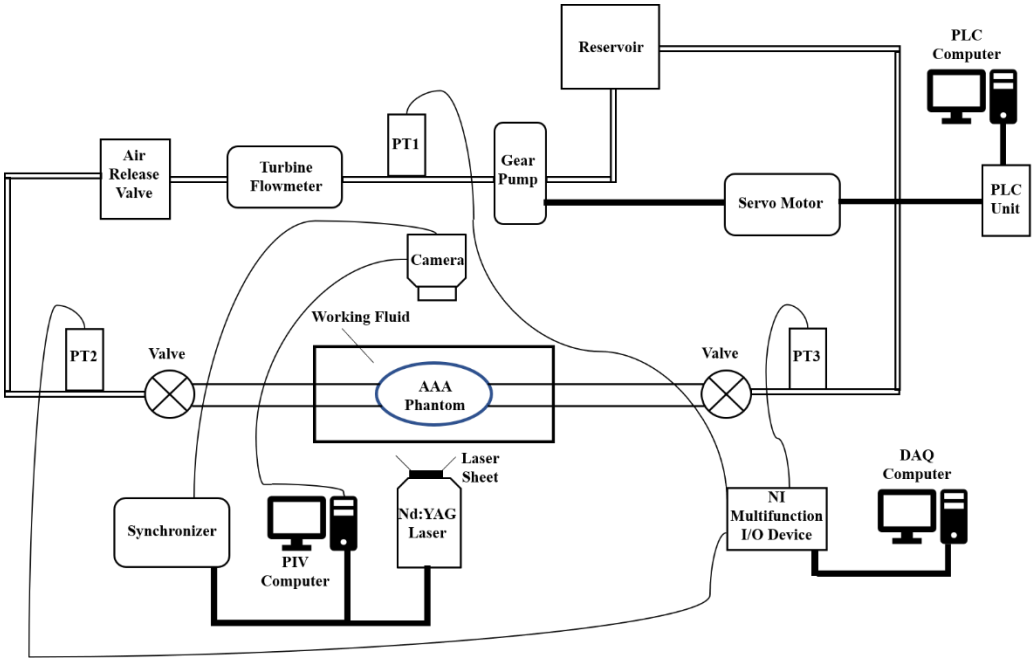

Figure 3.1: A schematic of the experimental setup

3.1.1 AAA Phantom

To investigate the flow field and extract detailed information about vortex structures for different flow conditions, a simplified elliptical geometry is selected which is characterized by D/d and L/d values. D is selected as 46 mm, L is 73.6 mm, and d is 18.4 mm as it is displayed in Figure 3.2. This geometry is chosen to simulate a typical AAA with realistic dimensions [18]. The neck region upstream where the inlet pipe and bulge are connected can be defined as the proximal neck while the symmetric part of it at downstream can be defined as the distal end. These definitions will be extensively used in the third chapter while discussing the flow field of unsteady flow patterns.

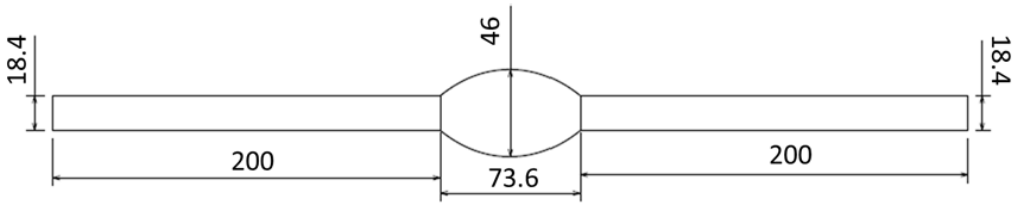

Figure 3.2: A sketch of AAA phantom with its dimensions given in mm

The AAA geometry is made of pyrex glass with a refractive index of 1.47. The vessel is placed in a rectangular box made from acrylic glass with refractive index of 1.495. The front face of this box on which the laser penetrates is made as thin as possible with a thickness of 2 mm to minimize the reflection and refraction of the laser sheet. The space between the vessel and the box is filled with the working fluid to minimize refraction.

3.1.2 Working Fluid

The working fluid is selected as a mixture of distilled water, glycerin and sodium thiocyanide with weight ratios 37.5, 17.7 and 44.81 respectively, considering mixture with RI of 1.47 in Figure 2.7. The density is measured as 1310 kg/m^3. RI of

the fluid was measured in METU Central Laboratory Polymer Analysis Laboratory by using a refractometer. The measurements were taken for four different temperatures and five different measurements were taken for each temperature. The results were reported as the average of them in Table 3.1.

Table 3.1: Refractive index of the working fluid at different temperatures

Temperature (˚C)	Refractive Index
15	1.47479
20	1.47340
25	1.47209
30	1.47110

Since the glass vessel is produced by blowing, the resulting geometry is not perfectly smooth and the thickness is not constant throughout the vessel. The RI of the vessel is not the same throughout the phantom, but considering that pyrex glass materials have RI around 1.470, it can be said that RI match is satisfied. A considerable decrease in the temperature must be avoided as RI of the fluid is nearly 1.475 which is not preferable.

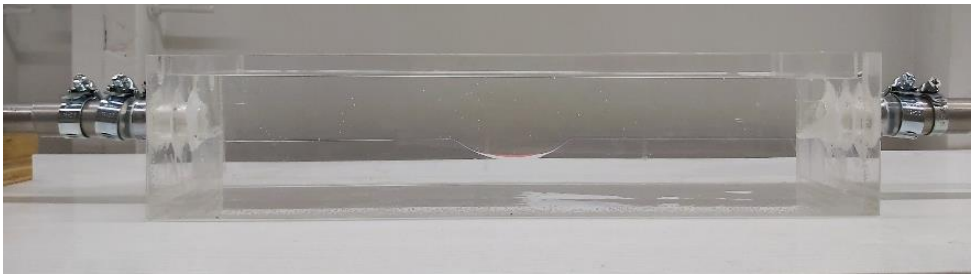

Figure 3.3: Working fluid filled in the vessel, and between the phantom and box to show RI match

The fluid is naturally transparent as water. However, it is observed to have a reactive characteristic while in contact with some material types. If it is in contact with a surface consisting of iron, iron and thiocyanide ions can combine to FeSCN, which has a blood-red color. The related chemical reaction is given below.

$$SCN^{-} + Fe^{3+} \rightarrow [Fe(SCN)]^{+2}$$

An experimental setup should not include a component with iron on the surface if the working fluid contains sodium thiocyanate. This situation is strictly considered during the installation process of the experimental setup parts, as it will be explained in the related subchapter.

The dynamic viscosity of the fluid was measured in an experiment of Hagen – Poiseuille flow where the fluid flows through a constant diameter hose in a straight pattern. Pressure measurements were taken with two different pressure transducers with a 5 m distance between them to ensure a considerable pressure drop. The pressure drop is calculated and by using the known density, the kinematic viscosity of the working fluid is measured as 9.4E-6 m^2/s. This corresponds to a dynamic viscosity of 0.012314 Pa s.

3.2 Measurement Techniques

In this study, two different measurement techniques are used; particle image velocimetry to find the velocity field and pressure transducers to measure pressure at certain locations.

3.2.1 Particle Image Velocimetry

Particle Image Velocimetry (PIV) is a non-intrusive flow measurement technique to measure instantaneous velocity in flow field. It is basically illuminating the flow consisting of tracer particles with a light sheet and take two photographs with very

short time interval and applying correlation to these two images to analyze the velocity vectors of the fluid flow.

Seeding particles with dimensions in the unit of micrometers are inserted to flow so that the flow can be trackable under light. The density of the seeding particle must match with the density of the fluid to avoid floating or subsiding of the fluid particles. Moreover, high density difference will result in higher particle response time that may increase the uncertainty in the measurements. Lasers are used as light source in PIV setups. A pump source is needed to excite a material to obtain the needed energy in the laser pulse. By electromagnetic radiation, the atoms are brought to some specific energy levels. There are various types of lasers with some common characteristics and their unique properties. In this study, a Nd: Yag laser is used in which neodymium ions are used. Nd:Yag lasers are extensively used in PIV setups. They have four energy levels available, and the required threshold energy is low compared to other lasers which is a preferable advantage [37]. Charge Coupled Device type cameras are used frequently in PIV setups. The photo diodes are very sensitive to light intensity and each photocell sensor converts the light intensity into electrical energy in volts. A photograph is divided into interrogation areas and the size of these interrogation areas can be selected by the user in pixels. Rectangular or square interrogation areas with sizes 64x64 pixels, 32x32 pixels, 32x16 etc. are generally used. The selection is based on the problem and required resolution. As a rule of thumb for classical PIV, each interrogation area should have at least more than ten seeding particles. Another rule of thumb to be mentioned is here is that the maximum displacement of the seeding particles should be quarter of the interrogation area size. Very few particles may lead to miss the flow characteristics while having too many particles may lead to noisy PIV data. After the photograph is taken, light intensity function is calculated for each interrogation area. The correlation between the light intensity distribution of the two successive photographs include the needed information to extract the velocity vector of each interrogation area.

TSI PIV system is utilized as hardware to measure velocity of the flow field in the experimental setup. The laser source is double pulsed Q-switched Litron Nano L200-15 200mJ Nd: YAG. Laser beam is converted into a laser sheet by passing it through a cylindrical lens with a radius of -15 mm and spherical lens with a focal point of 1000 mm, respectively. A 4 -megapixel CMOS camera with the lens of the camera was Nikon AF NIKKOR 50mm f1.8 is used to take photographs. The limit of the laser shutter is 15 Hz. TSI LaserPulseTM 610036 is the synchronizer model in the setup. The seeding particle used in this study is Dantec Dynamics Silver Coated Hollow Glass Spheres type with 10 microns diameter and density of 1400 kg/m^3. The silver coating increases the reflectivity. Fast Fourier Transform is used as the correlation technique for image pairs to find the velocity field from the light intensity function. The PIV measurements are taken in the horizontal plane consisting from the flow direction and the normal of at the same distance from the walls in center as shown in Figure 3.4.

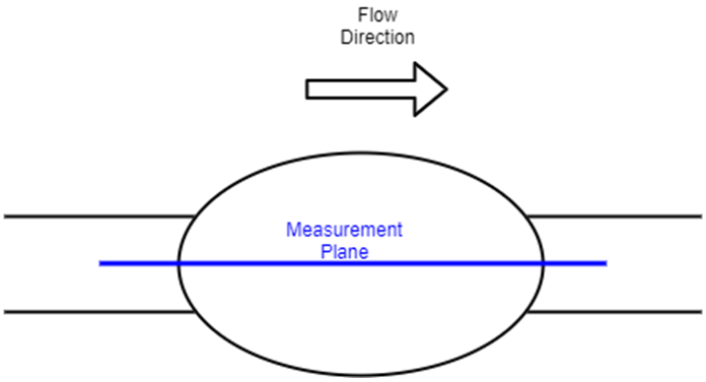

Figure 3.4: Measurement plane from the front view

The experiments in this study were conducted at the room temperature and temperature variation during an experiment did not go beyond 4˚C, so the effect of viscosity change of the working fluid is ignored. Moreover, the surroundings of the setup were covered with a blackout curtain to minimize external light sources.

3.2.2 Pressure Measurements

Pressure measurements are done by three pressure transducers. The transducers labeled by PT1 and PT2 are the same model, MESENS MPS500 series. Their measurement range is 0 – 4 bar the data output is between 4 – 20 mA. The accuracy of the measurements taken by these is 0.05% percent of the full-scale measurement. The other one, PT3, is WIKA ECO-1 model. The measurement range is 0 – 2.5 bar with the same accuracy as the others. These transducers are calibrated with a Bourdon gauge. The Bourdon gauge is calibrated by using a dead weight tester setup. These transducers are powered up by an external DC power supply, and the current measurement is done by National Instruments NI6024E card and SCB-68 terminal block with analog input and output terminals. The data is measured and collected by LABVIEW software. The data is extracted to MATLAB, and a low pass filter is applied to get rid of small frequency noisy data.

3.3 Experimental Matrices

One steady flow with Re 600 is chosen to discuss flow field in a typical steady flow. Two physiological flow patterns, one with a period of 1.1 seconds and the other with 2.9 seconds are studied. The Womersley numbers of these patterns are 7.17 and 4.42 respectively.

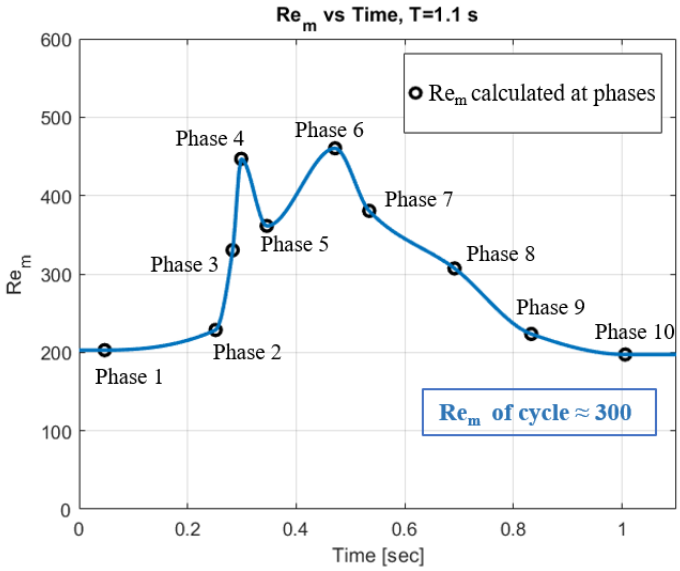

Figure 3.5: Variation of mean Re with respect to time for unsteady flow of 1.1 seconds period (T=1.1 s)

The variation of mean Re for the first physiological flow pattern with 1.1 seconds of period is displayed in Figure 3.5. Mean Re is calculated by circular integration of the velocity at the entrance of the inlet pipe found from PIV measurements. Mean Re increases till the fourth phase from the beginning of the cycle. It should be noted that the acceleration between the second and the fourth phases is steep. After the fourth phase, mean Re decreases and then increases gradually for a while. After the sixth phase, mean Re decreases gradually till the end of the cycle to the starting point.

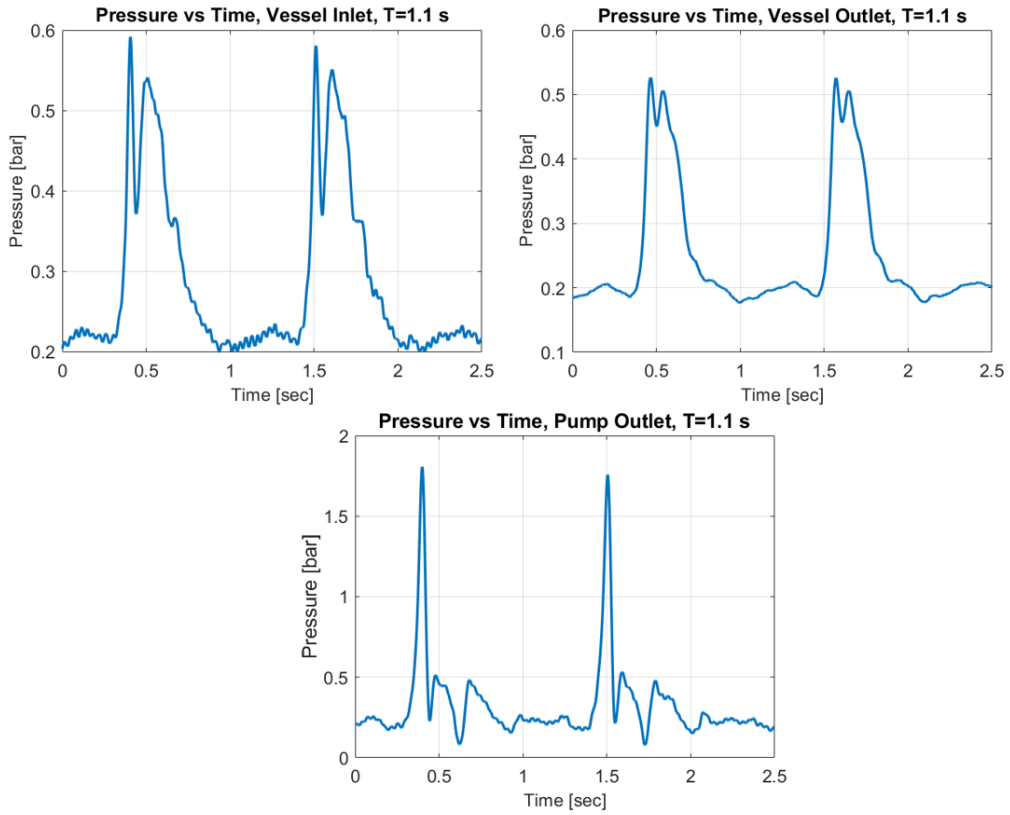

Figure 3.6: Pressure waveform at vessel inlet, vessel outlet and outlet of the pump, T=1.1 s

The pressure waveform of this physiological flow pattern can be seen in Figure 3.6. Although the peak pressure at the pump outlet is around 1.7 bar, it is noticeably damped before the vessel entrance. The large distance between the pump outlet and the vessel inlet causes damping of the pressure. Moreover, the hose downstream of the pump must be rotated in the opposite direction to guide it through the phantom. This curvature also plays a role in damping. After the peak, the pressure at the pump outlet decreases rapidly in the decelerating flow phase. Then the small acceleration gives rise to pressure to around 0.5 bar. The pressure then decreases to its lowest magnitude in the cycle where the flow is decelerated. For the rest of the cycle, the pressure at the pump outlet increases for a while and the decreases more gradually till a point where after it does not change remarkably. The pressure at the vessel entrance shows different waveform than the pump outlet. It can be said that there are

two acceleration and deceleration phases. The second acceleration and deceleration are observed to occur between the fifth and the sixth phases. After the second peak, the pressure at the vessel entrance is decreasing gradually. The pressure waveform at the vessel outlet follows a similar behavior as the vessel entrance but at lower magnitudes. There is small phase shift of 0.06 seconds due to the damping effect between these two points. Moreover, there is slight pressure drop between the vessel inlet and exit as the distance between them is around 2 meters.

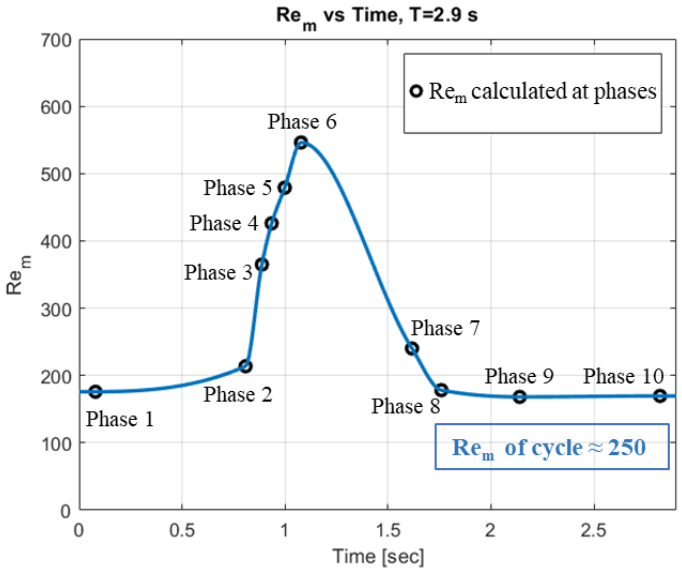

Figure 3.7: Variation of mean Re for unsteady flow of 2.9 seconds period (T=2.9 s)

The variation of mean Re for the second physiological flow pattern can be seen in Figure 3.7. This variation can be said to represent a typical physiological waveform. The cycle starts with a slight acceleration between the first two phases. Then the flowrate increases considerably phase by phase to the sixth phase at the end. The deceleration starts after the sixth phase and Re decreases dramatically between the sixth and the seventh phases. Mean Re does not change significantly for the rest of the cycle.

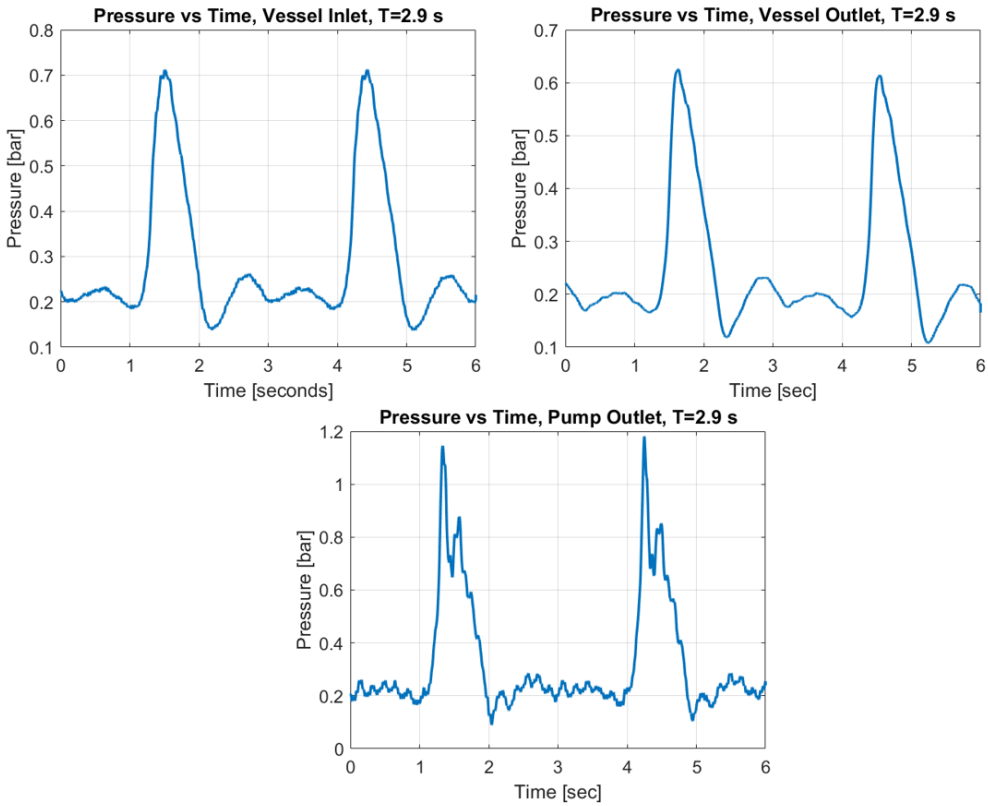

Figure 3.8: Pressure waveform at vessel inlet, vessel outlet and outlet of the pump, T=2.9 s

Pressure waveform at pump outlet, AAA phantom inlet and outlet can be seen in Figure 3.8. The pressure at the pump outlet decreases due to experimental setup concerns for fully developed flow at the vessel entrance. The large distance between the pump outlet and the vessel inlet causes damping of the pressure. Moreover, the hose downstream of the pump must be rotated in the opposite direction to guide it through the phantom. This curvature also plays a role in damping. The waveform of vessel inlet and outlet are very similar to each other with slight decrease between. The waveform obtained displays a more realistic physiological follow pattern compared to the one with 1.1 seconds of period since there is only one peak which is the peak systole.

3.4 Data Processing and Post-Processing

Taking of PIV images and processing of the raw data are done by using Insight software. To specify the boundaries of measurements, a static mask is formed in Insight software by generating points vicinity of the walls. These points are selected from inside of the wall of the phantom to reduce possible errors. Background subtraction is applied to get rid of objects detected by static display. 2D spatial calibration is done with respect to the inner diameter of the entrance pipe. As PIV plugin engine, Nyquist grid is selected which is the classical PIV grid. The selected interrogation area size is used once and then 50% overlap is used for fitting. Local vector validation is done by local median method which is the most popular approach. This method considers the median of velocity vectors at the neighborhood interrogation cells. For physiological flow patterns, synchronizer is triggered externally by using the information of the location of the pump blades. At a specific location of the shaft of the servo motor, a trigger signal is generated by using a power supply and a relay module. The generated pulse signal of 5V from the relay module is transferred to synchronizer with a trigger duration of 5 milliseconds, and the laser shutter is opened. By using external trigger, an image pair is taken for a specific instant of the cycle. This is done for multiple cycles and the average of the measurements are taken to obtain phase averaged results for physiological flow patterns. Meanwhile, continuous 15 Hz sampling rate is used for the steady flows.

The data sets of the experiments are extracted as txt files from TecPlot software. Then, they are extracted to MATLAB. Post processing is done in MATLAB, and it is s chosen to have full control over the dataset. Deriving the quantities required for different vortex identification schemes are user-friendly as well in MATLAB since it is matrix based computational programming software. The file contains positions of the interrogation areas with overlap and the velocity components in two directions. The column type data is converted into grid structure where every grid corresponds to interrogation area with the help of ‘griddata’ function. The data points in the dataset that are located out of mask contain ‘NaN’ data type. These data points are

determined, so the borders of the real measurement plane are specified. Velocity magnitude is calculated as the square root of the velocity in component and y component. Since PIV measurements provide discrete data, a finite difference method is needed to calculate the spatial derivatives of velocity. Least squares cells method is suggested for PIV experiments since it tries to minimize the random errors so this method is used in vortex identification methods [37]. It is applied to the applicable points for axial and normal velocity components in both directions. For the points near boundaries, first order forward or differences methods, or central difference methods are applied. It should be noted, applying different finite difference differentiation methods around the borders resulted in the same results. By using continuity equation in 3D, the gradient of the out of plane velocity component in the out of plane direction is calculated. The velocity gradient matrix is created in 2D for all cells of the dataset. Eigenvalues are calculated, and the imaginary parts are stored to specify swirling strength of each cell. Swirling strength defines the swirling intensity of a point, a high value means stronger vortical motion. The invariants of 2D velocity gradient matrix, P & R, are calculated. Δ - criterion is calculated as in Equation (2.9). It is based on negative values of the discriminant of the velocity gradient matrix to ensure closed or spiraling streamline pattern. Q-criterion is calculated as in Equation (2.12). Its magnitude determines the difference between the swirling motion and straining motion. λ_2 – criterion is also calculated by using Equation (2.17). It neglects viscosity and unsteady affects, and pressure minima is the base of this method. Vorticity is simply calculated in the direction of plane normal for every data point by using Equation (2.3). It should be noted a hybrid scheme is applied in the MATLAB code; as least squares method is applied to the available points, and central or first order forward/backward difference methods are applied to the remaining data points. The post process contours are drawn with suitable color map and bar settings for each figure. In addition, potential vortex core locations are investigated with ‘imregionalmax’ command, which detects local maxima values of the desired vortex identification methods.

CHAPTER 4

RESULTS AND DISCUSSIONS

This chapter presents the results of the PIV measurements of the experiments conducted in the laboratory. Swirling strength criterion is utilizied to reveal the evolution of vortices. The evolution and formation of the primary vortex is studied in detail. Moreover, some methods are tested to cancel noise and obtain more reliable and robust methods for PIV experiments.

4.1 PIV Measurements of Steady Flow

One case of study flow is analyzed to study the flow field under steady conditions in a AAA phantom. Eighty image pairs are used to estimate velocity field. Re 600 case is studied in detail here to investigate the flow field for a typical Re.

4.1.1 Steady Flow of Reynolds Number Re = 600

The general flow description of a steady will be done in this part. Laminar flows with different Re have common characteristics in the flow field. The axial velocity contour and streamline pattern can be seen in Figure 4.1. The jet flow is not disturbed, and translates in the axial direction without any curves. However, the region between the walls and a curved layer slightly outward radially from the jet flow is dominated by reverse motion. This reverse motion becomes more intense at the converging walls upstream of the distal end. These negative axial velocity values may indicate a vortex region in such an axially dominated flow pattern. Streamline pattern also shows that jet flow streamlines have no curvature as expected. The reverse motion identified from the axial velocity contour is proven by the streamlines as a large region of recirculation motion with a center located upstream of the distal

end. It can be said that there is one vortex ring with a large size completely occupying the bulging section.

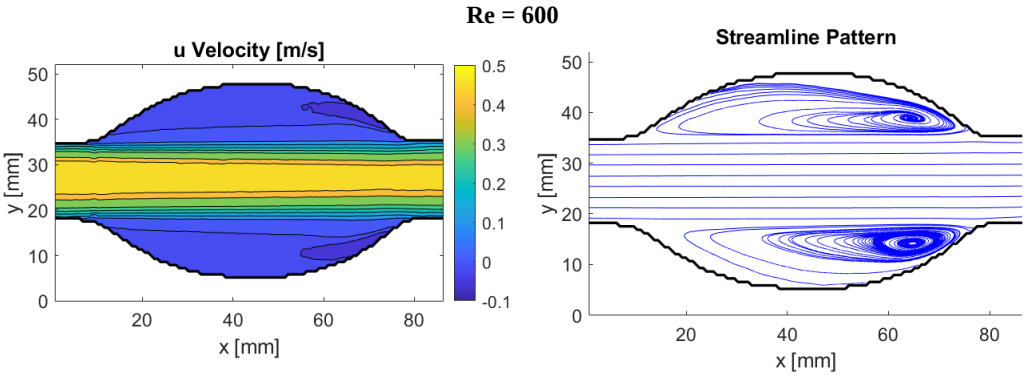

Figure 4.1: Axial velocity contour at the left and streamline pattern at the right for the steady flow of Re = 600

To understand more about the vortex structure of this flow, vortex identification methods that are reviewed in this work can be applied. The results can be seen in Figure 4.2. No filter is applied to these methods but only an arbitrary threshold is selected. As it is discussed in the review part of these methods, it is expected that the results will indicate the same regions as vortex since it is a planar measurement. It can be said that this expectancy is fulfilled. The core of the recirculation motion can be found upstream of the distal end. The global maxima locations are the same for all methods applied. However, the data includes noise due to uncertainty in normal velocity distribution, which is very high when the estimated velocity is very low. This situation is valid for a steady flow, as the flow is dominated by high axial velocity magnitudes except around the core of the vortex core. The maximum swirling strength inside the bulge is 10.6, which is located at the down half. For the upper half, it is 9.26. It can be said that a vortex ring with an average swirling strength of 9.93 dominates the flow. The locations of the maximums are nearly symmetric with respect to the horizontal centerline.

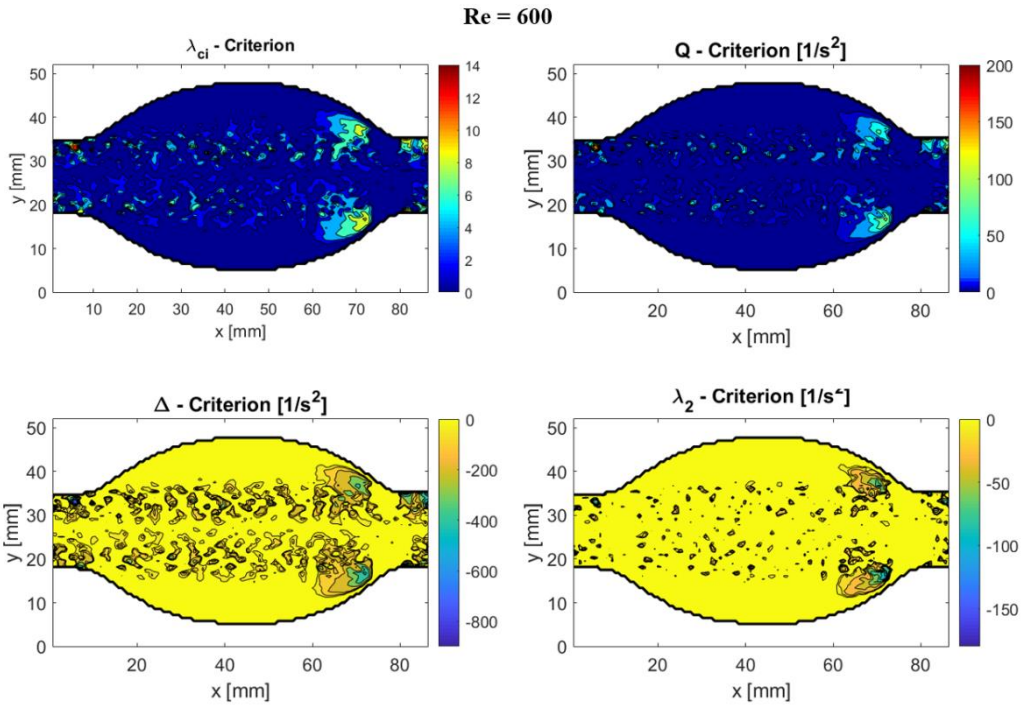

Figure 4.2: λ_{ci}, Q - criterion, Δ - criterion and λ_2 - criterion methods applied to the steady flow of Re = 600

The classical approach of vorticity magnitude can be also followed to identify the vortices as discussed before. As a reminder, vorticity magnitude includes shear layers. Vorticity in the direction normal to the measurement plane is calculated by applying the least squares method and represented in Figure 4.3. It shows an antisymmetric behavior with respect to the horizontal centerline as the values between this line and recirculation motion at the upper half is positive, while for the other half it is negative. The center of a vortex cannot be identified by using this contour. The highest values occur in the proximal neck, and they correspond to shear layers, not the vortex core. Hence, vorticity magnitude can be said to be insufficient to identify vortices in a steady flow of AAA cases.

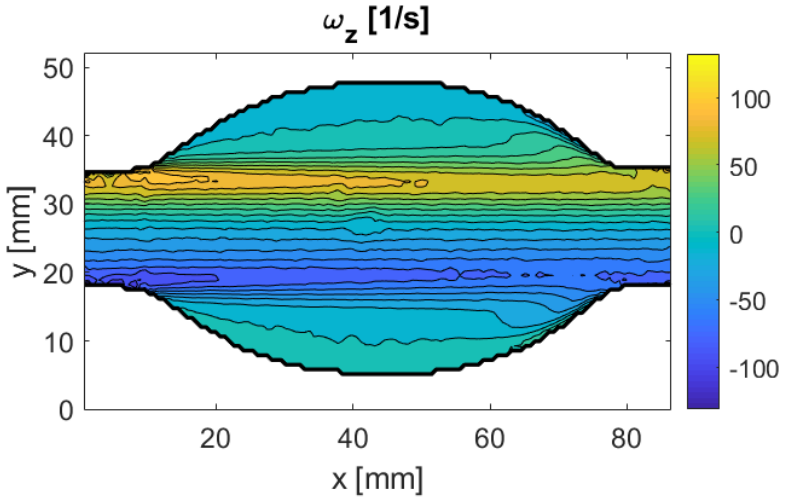

Figure 4.3: Vorticity contour for steady flow of Re = 600

4.2 Validation of Results and Code Verification

To validate the results in this study, a comparison is made with a previous steady considering a steady flow with a very close Re. The comparison is presented in Figure 4.4. The Re is 584 for the compared case, and the bulge geometry is different compared to the geometry used in this study. The differences in axial velocity magnitudes are caused by the difference in geometry. However, the distribution of axial velocity is very similar. The streamline pattern is nearly the same as well. The results show that the flow field is obtained as expected.

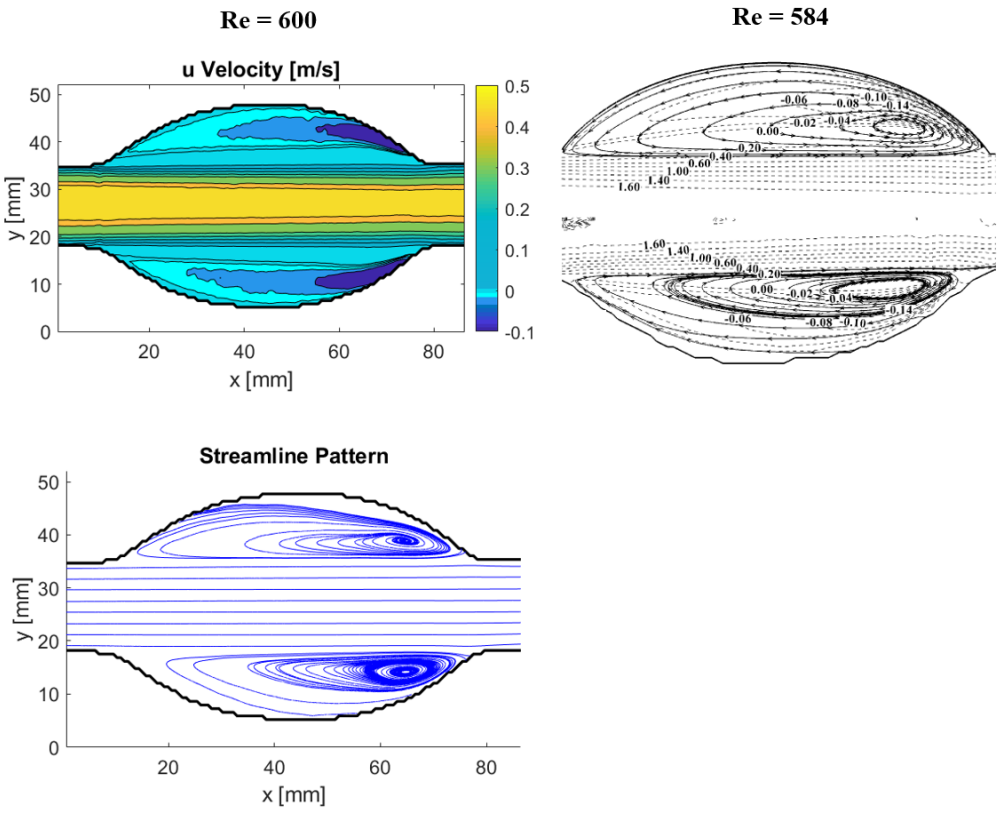

Figure 4.4: Comparison of steady flow field with respect to axial velocity distribution and streamline pattern [30]

To validate the MATLAB code that is developed for this study, a simple comparison can be made by using a software. This comparison is done by using Paraview to calculate the vorticity in the out of plane direction, and the results can be seen in Figure 4.5. The distribution can be said to be same for the developed code and Paraview. Another comparison can be done in a quantitative way for vorticity in the out of plane direction. Vorticity in the out plane is calculated for two different vertical cross-sections; one at the entrance pipe and one at the center of the bulge. The results can be compared by Figure 4.6. It can be said that both the trend and magnitudes are very similar.

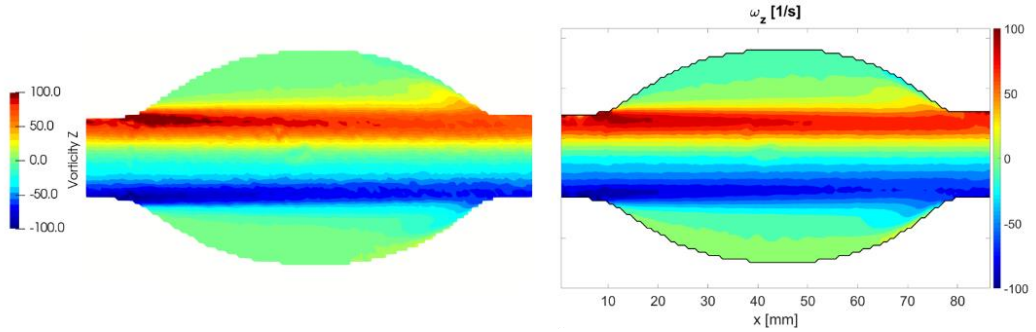

Figure 4.5: Comparison of vorticity in the out of plane direction between Paraview (at left) and MATLAB code (at right)

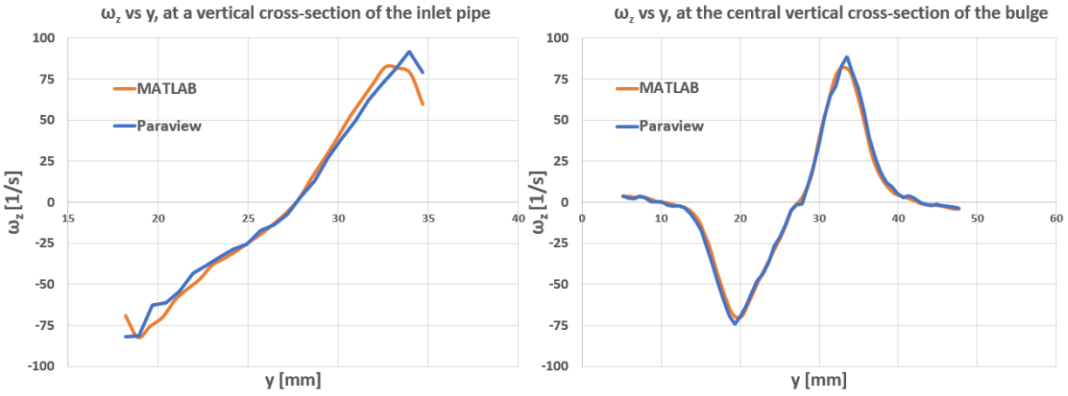

Figure 4.6: Comparison of vorticity in the out of plane direction for the used code and Paraview; at a vertical cross-section of the entrance pipe at left, and at the central vertical cross-section of the bulge at right

4.3 Physiological Flow of Period 1.1 Seconds

The variation of mean Re in time for this flow pattern can be seen in Figure 3.5. Mean Re values are calculated from PIV measurements and a circular integration scheme is followed to calculate the flowrate at phases. Although this cycle is not simulating a perfectly realistic physiological flow pattern, it contains typical acceleration and deceleration process. The second acceleration and deceleration period do not change the flow field considerably. This observation will be done in PIV measurements part. Mean Re of the cycle is calculated as 300.

4.3.1 PIV Measurements

PIV measurements are taken for ten different phases, and phase averaging is done for 100 cycles to obtain satisfactory statistical convergence. The interrogation area used is 32 x 32 with 50% overlap. The spatial resolution of an interrogation area is 14.36 mm before overlap is applied.

A brief description of flow field is required here before the detailed discussion since it is complex, and reading it from the first phase to the last phase may be confusing. A vortex ring is initialized around the fifth phase where deceleration starts. This vortex rings moves downstream and collides with the walls close to the distal end around the end of the cycle. Then, its downstream motion stops due to the effect of collision. Moreover, a secondary vortex ring is formed with an opposite axis of rotation. After a while, another vortex ring is formed due to division of the primary ring into two. This third ring is labeled as second primary vortex ring. It should be noted that while the vortex ring is being initialized at the fifth phase, the remaining vortex rings from the previous phase still exist in the bulge at the next cycle. The discussion in this part can be followed regarding this general description.

Axial (streamwise) and normal (perpendicular to streamwise) velocity components are presented with contours in this part. They are used to give general description of the flow field. After giving general information about the velocity distribution, the focus will be on the vortex identification and characterization. To do that, phase averaged streamline patterns and swirling strength contours are provided. The selected vortex identification method is the swirling strength criterion. The threshold of 1.5 is applied which is generally appropriate for two-dimensional analysis [38].

The axial velocity contours of the first six phases can be seen in Figure 4.7. The contours of the remaining last four phases are presented in Figure 4.8. Normal velocity component contours of the first six phases can be seen in Figure 4.9. For the rest of the phases, they are shown in Figure 4.10.

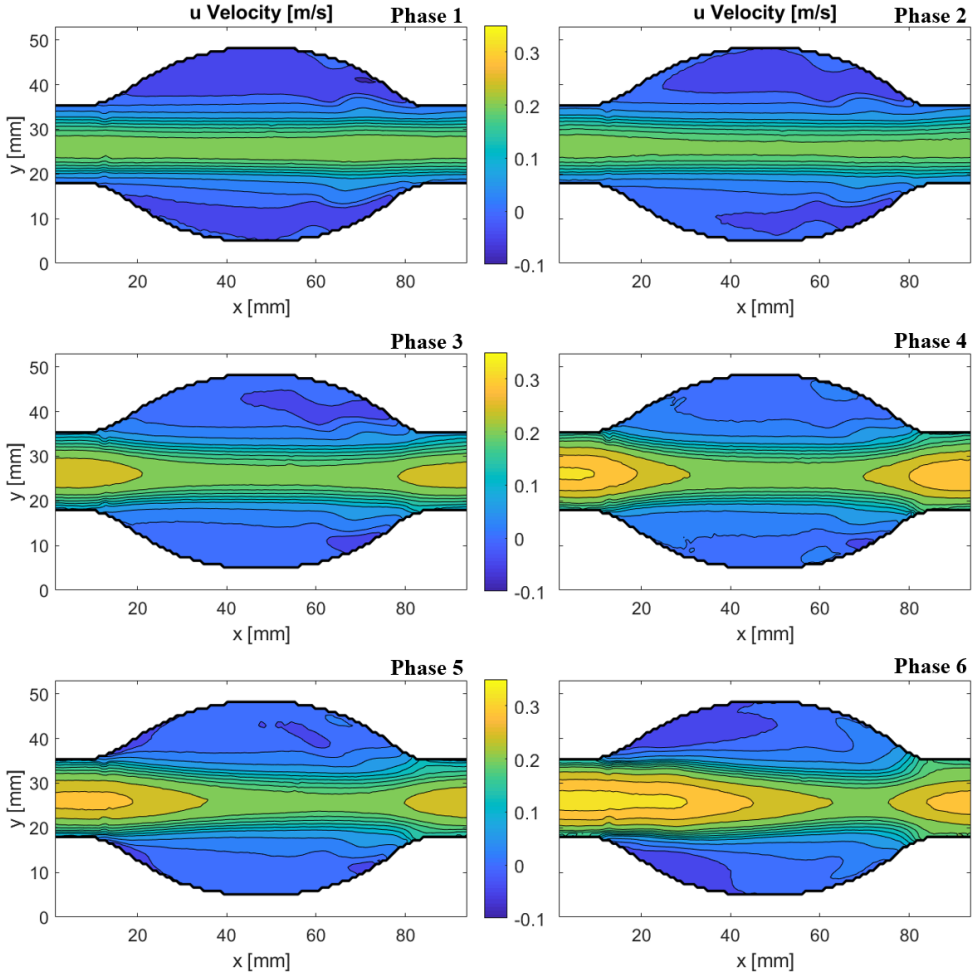

Figure 4.7: Axial velocity contours of the first six phases, T=1.1 s

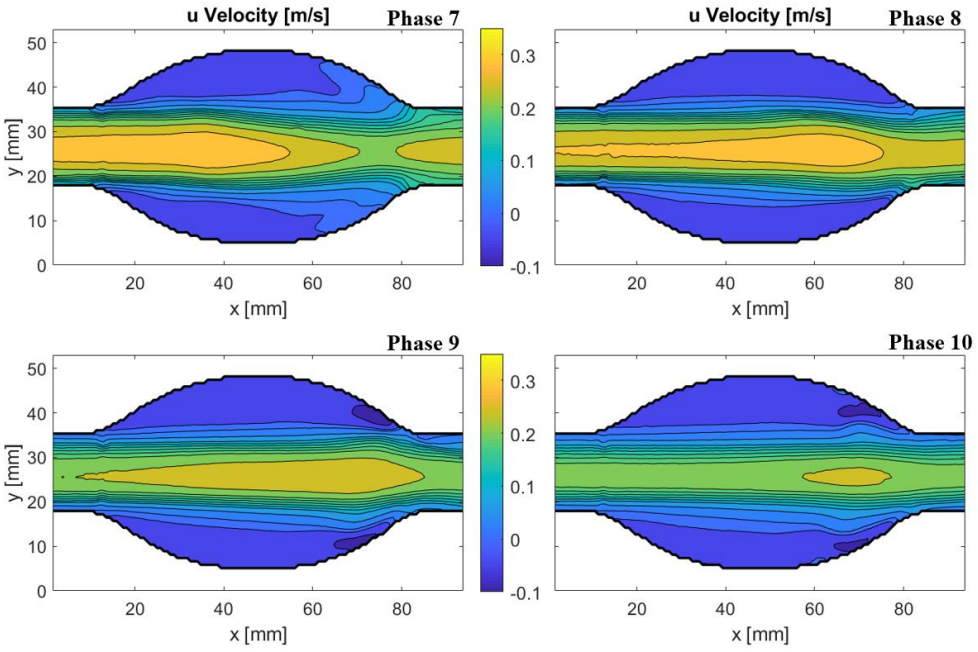

Figure 4.8: Axial velocity contours of the last four phases, T=1.1 s

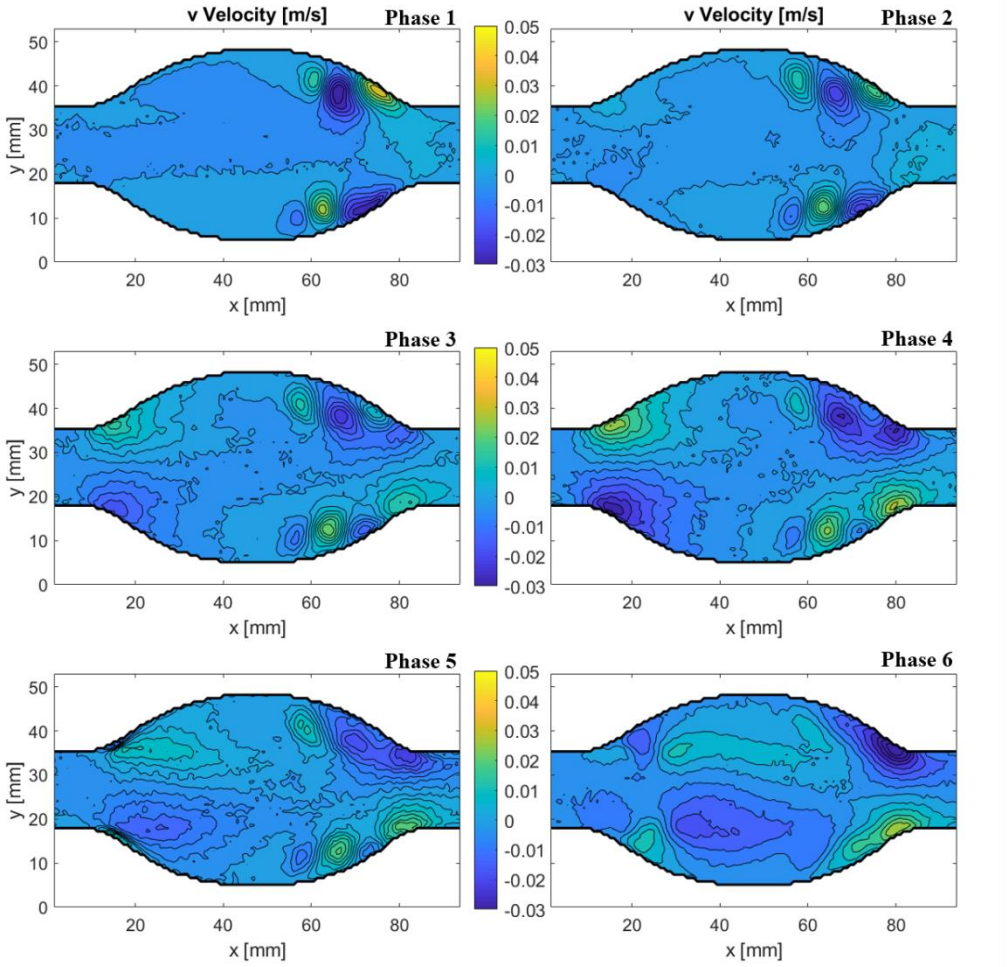

Figure 4.9: Normal velocity contours of the first six phases, T=1.1 s

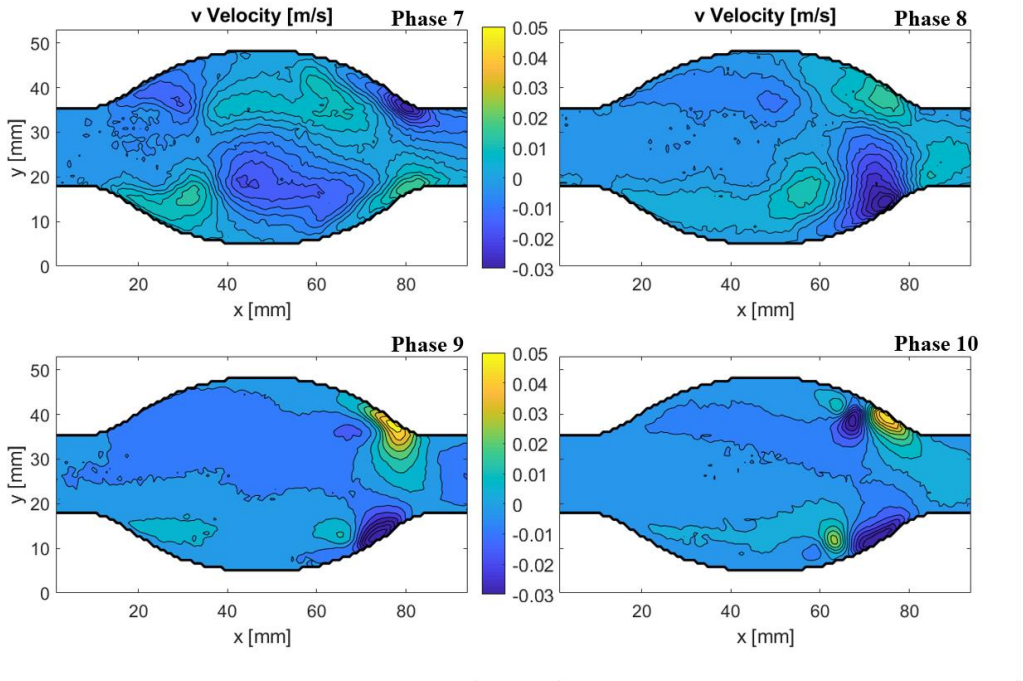

Figure 4.10: Normal velocity contours of the last four phases, T=1.1 s

Axial velocity distribution shows symmetric behavior with respect to horizontal centerline for the first two phases. There are regions with negative axial velocity upstream of the distal end at the bulging section, which indicates backflow motion that may be related with recirculation region. This reverse motion is stronger close to the distal end, and gets weaker upstream. One observation made from this axial velocity distribution is the growing region on of positive magnitudes located at both halves of the bulge vicinity of the walls, which is confined by the slowly recirculating flow particles around. This increase is expected as there is slight acceleration between the first two phases. There are regions with negative signs of each other, and nearly the same magnitude distribution in the normal velocity contours for the first two phases. They are related with the vortical motion in such a flow dominated with axial components. Streamline pattern and swirling strength contours reveal the flow field in those regions.

The third phase is at the accelerating time interval before the expected peak flow rate, and the fourth phase is just before the peak flow rate, defined as the peak systole. The axial velocity distribution can be said to be symmetrical with respect to horizontal centerline for third and the fourth phases. The magnitudes of axial velocity component increase in overall at the third phase due to acceleration compared to the previous phases. The same situation is valid for the change between the fourth phase and the third phase as well. The reverse flow gets weaker, so it can be said that flow attaches to the walls of the diverging section of the bulge. The jet flow region expanses in the fourth phase, as it is expected due to rapid acceleration. The normal velocity distribution is skew symmetric with respect to the horizontal centerline just like for these phases just like the first two. At the fourth phase, the concentrated region of high normal velocity components grabs attention at the proximal neck. It can be thought as the indicator of vortex ring formation.

The fifth phase is just after the start of the deceleration. It is known that the vortex ring is initialized around these phase points for a typical physiological flow pattern due to velocity discontinuity occurring during deceleration. The sixth phase is a little after that phase, and flow accelerates in between. The axial velocity distribution can be said to be symmetrical with respect to the horizontal centerline for the sixth phase while there is little asymmetry at the fifth phase as there is a very small region with high negative axial velocity. The jet flow is being slightly compressed upstream of the center of the bulge, and then it follows a diverging pattern for both phases. The magnitudes decrease overall with respect to the previous phase due to deceleration for the fifth phase. The opposite case is valid for the sixth phase, which is expected as there is another acceleration between the fifth and the sixth phases. The velocity in normal direction shows that concentrated high magnitudes at the proximal neck separated from the walls at the fifth phase, which indicates the vortex ring is formed. Just downstream of the proximal neck, there are regions with high and low magnitudes as the previous phases, which are the signs of vortex structures as observed in previous phases. At the sixth phase, the downstream translation of the initialized vortex ring can be seen clearly from the downstream shift of high

magnitudes in normal velocity component. There is only one skew symmetric region with locally concentrated high magnitudes at the converging section for the sixth phase. This may be a sign that the remaining vortex structures from the previous cycle that had been observed so far may have died out. Streamlines and swirling contours will provide more information about this.

For the seventh phase, the axial velocity magnitudes decrease overall compared to the sixth phase due to deceleration in the cycle. The eighth phase shows further deceleration compared to the seventh one, as the highest jet flow regions gets very thinner at the inlet section. For these both phases, the reverse flow occupies the bulging section with low magnitudes. Velocity in the normal direction still shows skew symmetric behavior with the highest absolute values concentrated at the distal end close to the walls. However, if the normal velocity distribution of the seventh and the eighth phases are compared, one can notice major differences. The primary vortex ring generated in the fifth phase must have translated in a large axial distance between these two phases. At the eighth phase, the normal velocity upstream of the distal end at the down half show negative and high magnitudes. Just the opposite case is valid for the upper wall side. These concentrated high magnitudes may be resulting from the axial displacement of the primary vortex ring.

It can be said that, there is a symmetric distribution with respect to the horizontal centerline, and reverse flow is dominant at the converging section of the bulge upstream of the distal end for the last two phases. This reverse flow is actually related with a strong recirculation around the vortex core. Compared to the eighth phase, the magnitudes decrease overall for the ninth phase and general translation motion can be seen clearly. Between the last two phases, there is deceleration which can be seen as a drop in the magnitudes of the jet flow velocity. There is a major difference between the last two phases. A new region with locally high magnitudes can be observed for the last phase upstream of the distal end. This may be an indicator of a new flow structure occurring at the last phase. For the last phases, as in all cases, the magnitudes are very low in overall.

Streamline patterns for the first six phases are shown in Figure 4.11. For the remaining phases, they are presented in Figure 4.12. Swirling strength contours of the first six phases are shown in Figure 4.13. For the remaining phases, they are presented in Figure 4.14.

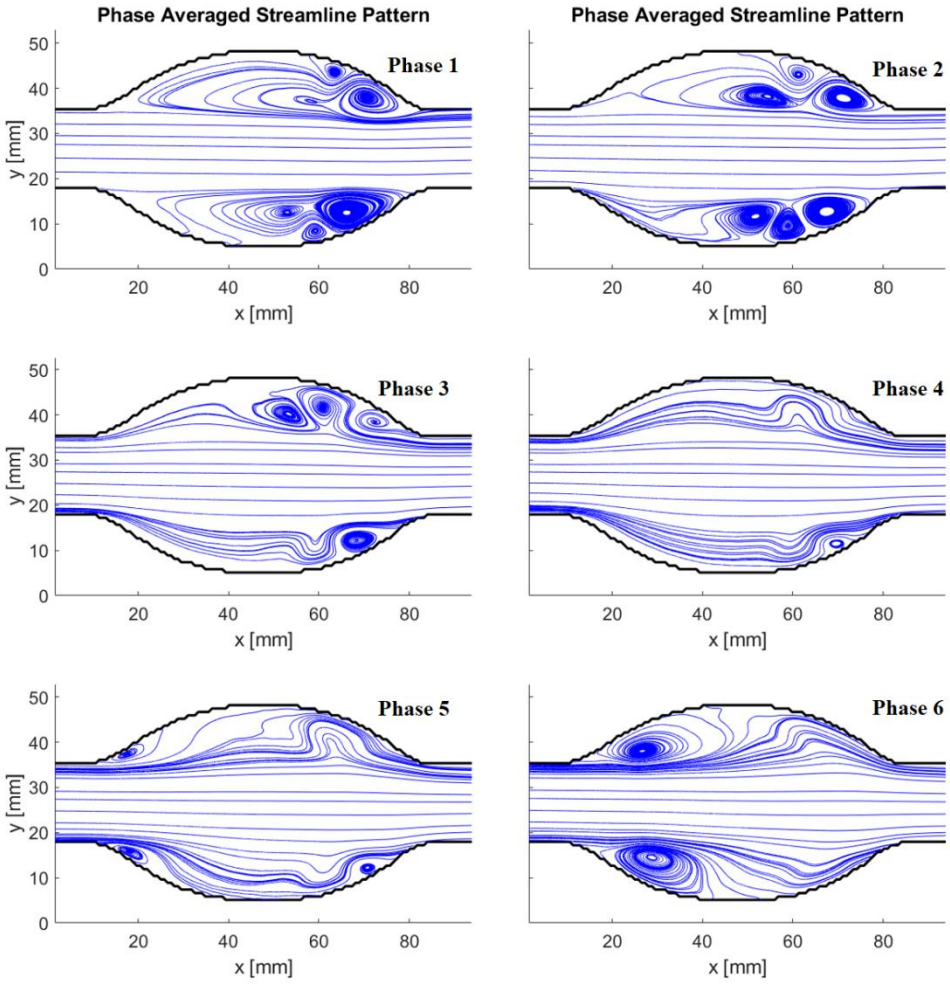

Figure 4.11: Streamline patterns of the first six phases, T=1.1 s

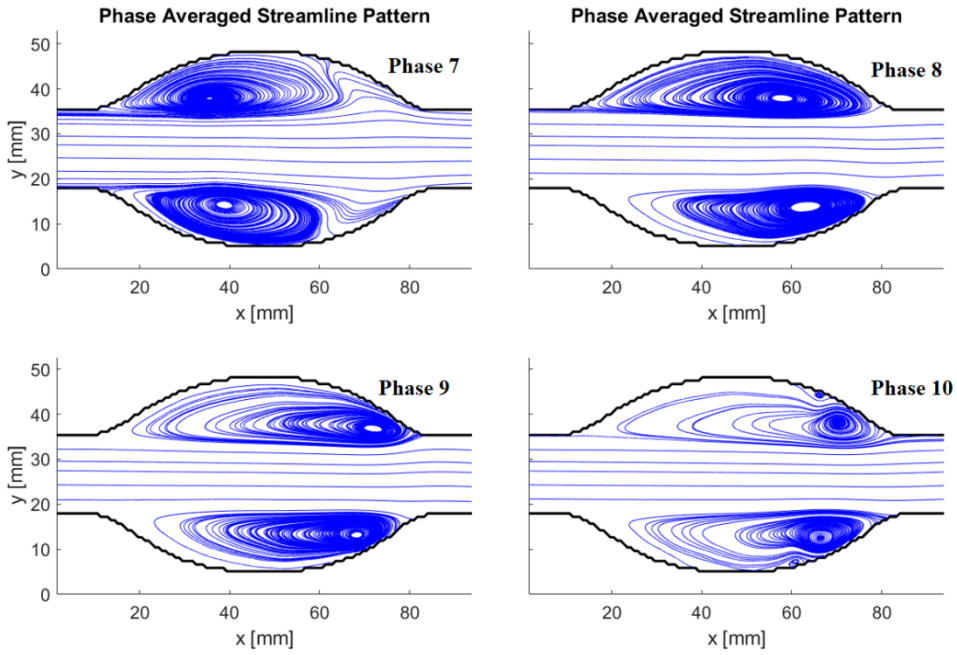

Figure 4.12: Streamline patterns of the last four phases, T=1.1 s

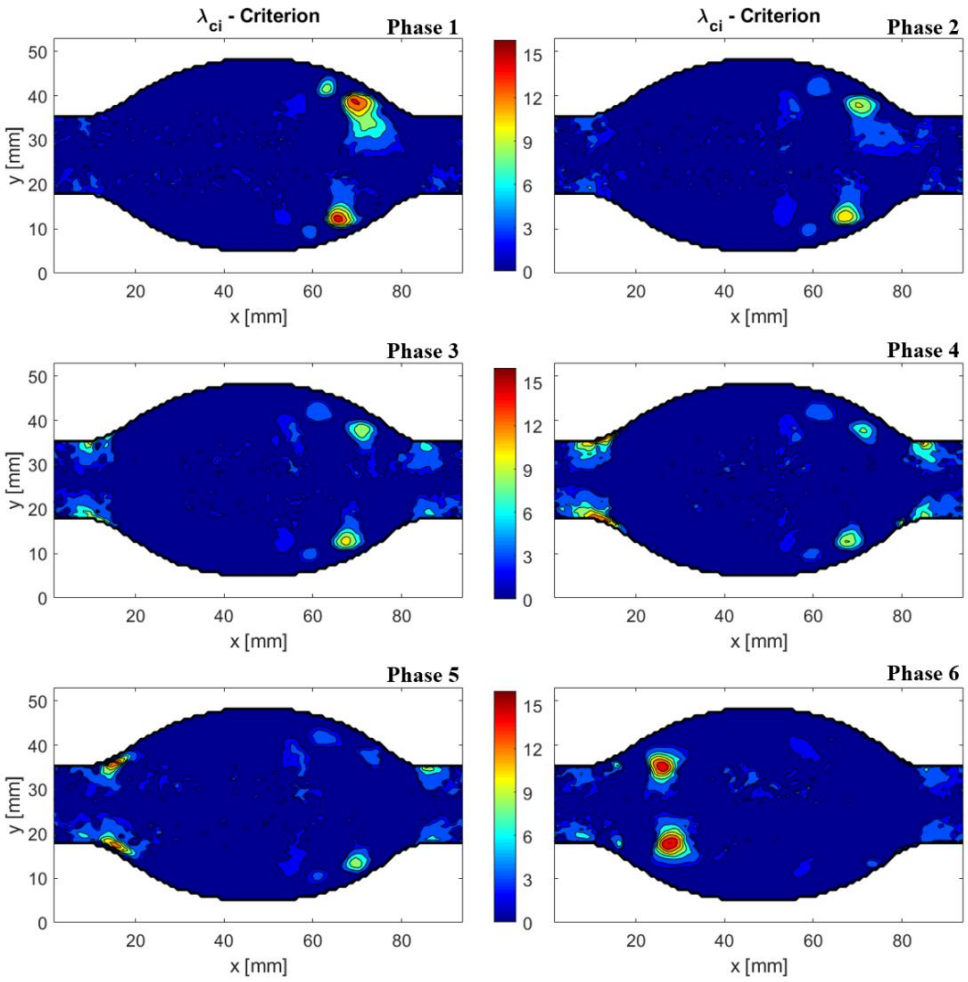

Figure 4.13: Swirling strength contours of the first six phases, T=1.1 s

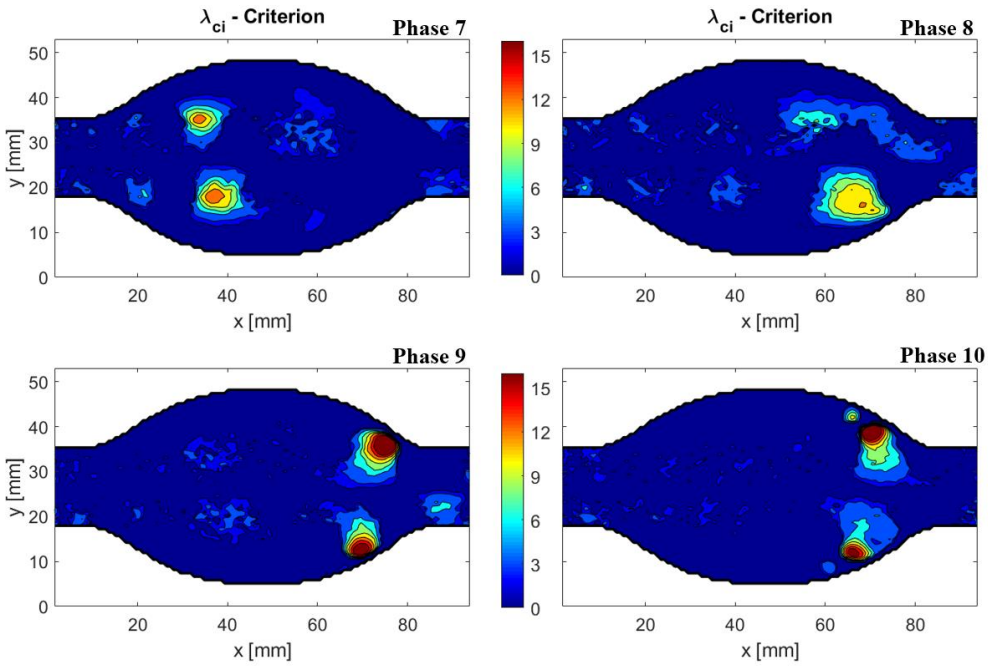

Figure 4.14: Swirling strength contours of the last four phases, T=1.1 s

The streamline pattern in the first two phases reveals complex flow structures inside AAA. As mentioned at the beginning, the primary vortex ring collides with the walls at the converging section upstream of the distal end around the end of a cycle, so a secondary vortex structure is generated around the end of a cycle, the tenth phase. In addition to these two vortices, a third vortex region is identified by the streamline pattern at the first phase. This new vortex is being originated from the primary vortex ring, as seen from the streamline pattern. The primary one and this new vortex are enclosed by common closed streamlines. However, their centers are separated distinctly. It can be said that the primary vortex is dividing into two parts after the effect of collision. This divided part of the main vortex ring can be labeled as the second primary vortex ring. Between the second phase and the first phase, the secondary vortex gets larger, but gets weaker in swirling intensity. The secondary vortex ring is confined between other two vortex rings and gets larger in size considerably between the first phase and the second phase. Moreover, slight

acceleration between the first and the second phases leads to flow attachment downstream of the proximal neck, especially for the down half. Swirling strength identifies the three vortex rings which are seen in the streamlines as well for the first two phases. However, it must be noticed that swirling strength of the second primary vortex ring is very small compared to the primary vortex ring and the secondary one. Its magnitude can be compared with the noisy data that does indicate any physically existing vortex structure or very small-scale vortex structures. Nonetheless, streamlines justify the existence of a weakly rotating vortex ring there. For the first phase; the magnitude of the maximum swirling strength of the primary vortex ring at upper half is 14.43 and 15.01 at the down half. For the secondary vortex ring it is 9.17 at the upper half and 5.97 at the down half. Lastly, the maximum swirling strength of second primary vortex ring at the upper half is 2.89 and 2.16 at the down half. These values indicate that the swirling intensity of the second primary vortex ring is too weak compared to other two vortices. Between the first two phases, the primary vortex ring loses its swirling intensity and transfers it to the second primary one. There is also a decrease in the secondary one as it expands into larger area while there is no such considerable change for the second primary one. The primary vortex ring at the upper half is observed to have a diffusive swirling intensity, that is tended to the distal end at the second phase. The reason for such a distribution is that the cross-section of the primary vortex ring at the upper half is closer to the distal end vertically in the last phase as in this phase, so it is exposed to the low pressure at the distal end. This mentioned flow field can also be seen from the streamline pattern.

Streamline patterns shows no symmetry with respect to the horizonal centerline for the third and fourth phases. The pre-defined vortex rings can still be identified with ease on the upper half, but not for the down half at the third phase. For the third phase; the primary vortex ring gets smaller at both cross-sections. On the upper half, the cross-section of the secondary vortex ring seems to increase in size and get compressed between the primary and the second primary vortex ring. At the down half, streamlines show considerably difference flow characteristics. Only the primary vortex ring can be identified with ease. However, streamlines show a hill-like

structure just downstream of the primary vortex ring. As it was explained in vortex identification methods part, this region seems to be a vortex, but the relative speed may be very low compared to general convection velocity magnitudes. This situation may also be caused by weak mixing of seeding particles in that region due to weak mixing. This will be investigated further in the upcoming sections. For the fourth phase; streamlines can only detect one vortex structure, which is the cross-section of the primary vortex ring at the down half of the bulge which is observed to be very small in diameter compared to the previous phases from the start of the cycle. There two hill-like structures in both halves that may correspond the vortex regions with low convection velocities. It should be noted that; the flow is attached to the walls at the diverging section in the fourth phase as the flow rate increased considerably.

Unlike phase averaged streamlines, the vortex rings identified for previous phases can still be recognized easily by swirling strength distribution for the third phase. The cross-section of the primary vortex ring at upper half has a maximum swirling strength of 9.41, at lower half 10.76. The second primary vortex ring at upper half has maximum swirling strength of 3.58 and lower half 2.64. The secondary vortex ring at the upper half has maximum swirling strength of 5.13, at the down half it is 4.24. This indicates that the visibility of hill-like structure is not related with the swirling strength magnitude. One may think that the vortex rings with lowest swirling intensities will not be captured by streamlines, but this is not true in this case. This phase strongly demonstrates the fact that streamlines may not be able to identify the vortex structures in planar PIV measurements with high accuracy. Unsteadiness in the problem, the homogeneity of distribution of seeding particles due to experimental conditions have major role on the effectiveness of streamlines approach to characterize vortex structures. One interesting thing seen in this phase is the existence of very high swirling intensities at the straight pipes close to the walls. This is the indicator that the primary vortex ring is about to be formed. For the fourth phase; swirling strength contour still identifies three of the vortex rings as before. In this phase, the maximum of swirling strength can be seen at the proximal neck and the distal end around the walls as the previous phase as well. The primary vortex

rings swirling intensity decreases between the third and the fourth phase, while the swirling strength of the other two vortices do not change considerably.

The vortex ring is initialized at the fifth phase as the streamlines having a closing pattern just downstream of the proximal neck. The streamlines vicinity of the initialized vortex ring tends to go up or down direction depending on the half due to lower pressure around the vortex core. The core of the remaining vortex ring at the down half from the previous phase can be identified by streamline pattern like the previous phase. For the upper half, one cannot identify any vortex core from the streamlines, but some locations can be observed to have hill-like patterns as before. Vortex identification methods will provide more information about them as usual. The initialized vortex ring in the fifth phase becomes more explicit at the sixth phase. The jet flow streamlines go in straight lines to the distal end. Streamlines show no vortex ring close to the distal end, but there are curved streamlines due to the pressure gradient occurring from vortex ring, and they are most probably the remaining vortex rings. The initial vortex ring can be seen clearly in the swirling strength contour of the fifth phase, which shows a nearly symmetrical vortex ring at the proximal neck. The local maximum of swirling strength magnitude in the initial vortex ring is 15.27 located at the upper half and 14.04 at the down half. It can be said that a vortex ring with an average swirling strength magnitude of 14.7 is occurring after the peak systole. For the sixth phase, the remaining vortex structures cannot be identified easily. Downstream of the primary vortex core, there are small scale vortex structures that are departed parts of the primary one. The second primary vortex can still be seen in its typical location. The primary vortex ring and the secondary vortex ring remaining from the previous cycles cannot be seen. Since they are relatively weak in terms in their swirling activity, the acceleration must have pushed them to the distal end. The maximum of swirling strength can be observed vicinity of the exit pipe in the sixth phase. A comparison between the swirling strength contours of fifth and sixth phases reveals that the remaining vortex rings from previous cycles have left the bulge, and they are transported out through the exit pipe close to the walls. The swirling intensity increases slightly between the fifth and the sixth phases. The center

of the vortex ring is located downstream for the down half compared to the upper half and the vortex core translated in axial direction. As an additional note, there is another small sized vortex ring upstream of the primary one at the sixth phase. This is due to second acceleration and deceleration that creates a secondary shear layer that rolls up to small scale vortex. Since the time derivatives are not that steep between the fifth and sixth phase as the previous phase couple, this vortex ring is smaller in size at this phase.

Streamlines show that primary vortex ring occupies the majority of the bulge section at the seventh phase. The primary vortex ring and its center can be located easily. The streamlines downstream of the spiraling ones are in convex shape due to the favorable pressure gradient at the converging. Swirling strength contour will prove this by showing no vortex rings there. Vortex ring is still evolving with small asymmetry as the cross-section at the down half is located more downstream compared to the upper half. Streamline pattern of the eighth phase shows that the primary vortex ring propagated to downstream of the center of the bulge. In this phase the streamlines show a similar structure to a steady flow pattern with low Reynolds number. Jet flow streamlines go straight to the distal end without any curves. Streamline pattern show that the axial distance between the two cross-sections of the primary vortex ring increased compared to the seventh phase. Swirling strength contour identifies the vortex ring clearly in the seventh phase. The swirling intensity decreases between this phase and the last phase. Moreover, the maximum of swirling strength decreases more for the upper half. There is another region with high swirling intensity upstream of the primary vortex ring. This is not a surprising outcome since there was another vortex ring that identified at the sixth phase due to the unexpected deceleration. However, this vortex is very small in size and strength compared to the primary vortex ring. The swirling strength magnitude of this vortex ring is changing between 5 and 6 in general. It should be noted that this vortex ring is not identified by the streamlines. For the eighth phase; meanwhile the phase averaged streamlines show a well-defined recirculation motion expanded in a large area, swirling strength contour shows distinct distribution characteristic

between the up and down cross sections of the vortex ring. The high swirling strength values at the upper half seems to have a diffusive distribution. At the down half of the bulge, the maximum of swirling strength is 12.44 meanwhile at the upper half it is 8.37. Compared to the previous phase, the maximum swirling strength of the upper cross-section decreases dramatically while the down one decreased gradually. This explains the diffusive distribution of the swirling intensity at the upper half. The after-initialized vortex ring also propagated downstream considerably with a nearly negligible change in its swirling strength distribution.

The ninth phase show a similar flow structure with the last phase considering streamline patterns. The vortex core translated considerably in axial direction and it is very close to the distal end. The jet flow streamlines go in straight lines as in the axial velocity contour. Streamlines show that the cross section at the upper half is closer to the distal end compared to the one at the down half with respect to the streamlines. This is the reverse of the previous phases. The down cross section is located more downstream compared to the upper half for the last phases after the primary vortex is initialized. The cross-section at the down half translated downstream. This fact may give hint about the possibility of collision of the vortex ring with walls as the axial movement direction has changed. Streamline pattern of the last phase reveals interesting flow characteristics. A secondary vortex structure can be seen upstream of the primary vortex ring. This secondary structure has a very small length scale at this phase. The vortex ring's translational motional is in upstream direction between the last phase and the ninth. This can only be caused by the interaction of the vortex ring with the wall. This interaction leads to generation of another vortex ring. Velocity vectors reveal that the center of the secondary vortex. The primary vortex ring is being reflected back from the walls between the last two phases as its axial displacement is negative. At the ninth phase, the vortex ring is very close to the distal neck, just a little upstream of it. The vortex ring is not perfectly symmetric if the center of the cross-sections is assumed to be maximum swirling strength positions. Swirling strength contour of the last phase reveals the primary and the secondary vortex ring for the last phase. The upstream displacement

is also observed from swirling strength distribution. The swirling intensity of the secondary vortex ring at the down half is larger than the other half likewise the primary vortex ring. The continuation of the last phase is the first phase, and it is seen that primary vortex ring is oriented into the distal end.

4.3.2 Evolution of Primary Vortex Ring

The position of the core of the primary vortex ring can be seen in Figure 4.15. The core locations are estimated from maximum swirling strength at the vortex ring locations. It should be noted that the core locations estimated by maximum swirling strength and streamline pattern are very close to each other with no considerable difference. The formed vortex ring follows an axial path till the seventh phase after its formation at the fifth phase. The symmetry of the vortex ring with respect to the horizontal centerline is disrupted as it moves a large distance axially between the seventh and the eighth phases. After the eighth phase, its downstream space is started to be restricted by the converging wall section. The reverse motion can be clearly seen between the ninth and the tenth phases indicating a collision of the vortex ring with the walls had already occurred. This collision leads to reversing the direction of translational displacement of the core for a time period and the next cycle starts at that interval. The displacement of the core between phases of the next cycle is very small due to low flow rate at the beginning of the cycle, and walls located just upstream. As the flow rate increases in the new cycle, it moves closer to the distal end, and it is no longer in the bulge after the sixth phase of the new cycle.

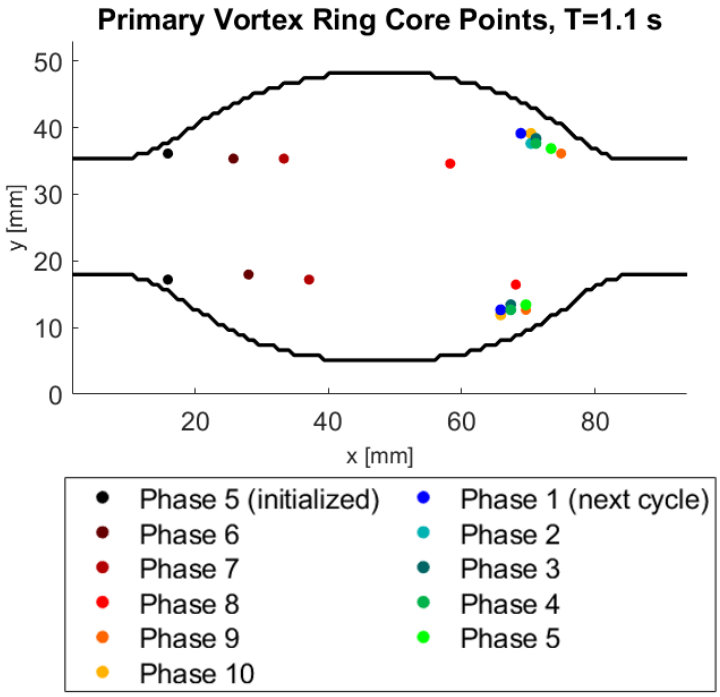

Figure 4.15: Location of primary vortex ring's core with respect to phases, T=1.1 s

The temporal evolution of the maximum swirling strength at the core of the primary vortex ring can be seen in Figure 4.16. After it is initialized, there is a slight increase till the sixth phase, and then slight decline for two phases. A dramatic increase between the eighth and the ninth phases draws attention. This huge increment is resulting from the collision of the vortex ring with the wall at the converging walls. After that, it decreases gradually with time, and it cannot be detected after the fifth phase in the bulge.

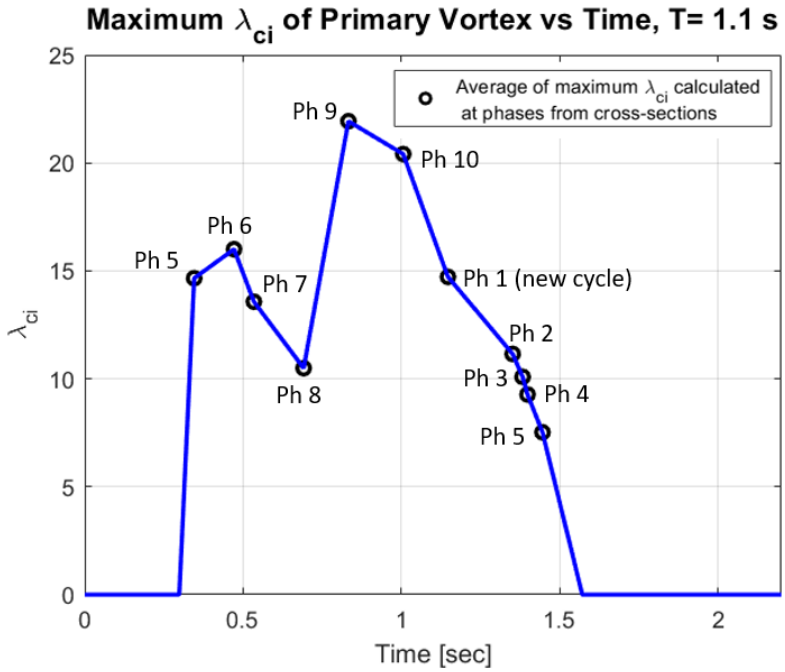

Figure 4.16: Variation of maximum swirling strength of the primary vortex ring calculated at phases in average of cross-sections, T=1.1

4.4 Physiological Flow of Period 2.9 Seconds

4.4.1 PIV Measurements

PIV measurements are taken for ten different phases, and phase averaging is done for 100 cycles to obtain good statistical convergence. The interrogation area used is 32 x 32 with 50% overlap. The spatial resolution of an interrogation area is 14.36 mm without overlap. The evolution of vortical structures are focused on for this flow pattern. Therefore, only swirling strength contours are presented for this case in Figure 4.17. It should be noted that although ten phases are used to take measurements and discussion, only six of them are shown. However, the flow field is explained considering all phases.

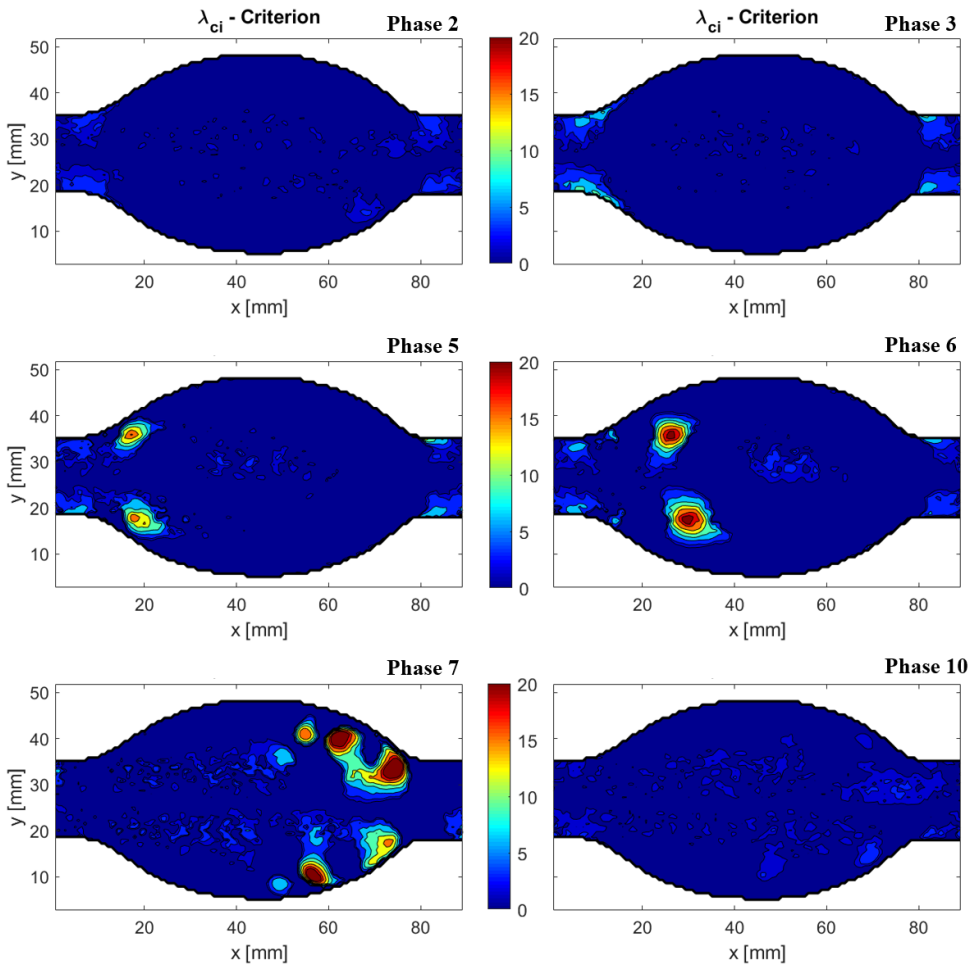

Figure 4.17: Swirling strength contours at selected phases, T=2.9 s

There are not any robust vortices in the first two phases. However, third phase shows interesting characteristics. High swirling strength values can be found at the proximal neck. It should be noticed that these high magnitudes do not reach to the center. As the acceleration proceeds further, vortex ring is started to be generated with higher swirling strength distribution compared to the third phase. The vortex ring is not detached from the walls of entrance pipe yet. The possible reasons of vortex generation at this phase is surface undulations due to a combination of phantom geometry and fluid-structure generation occurring in an inevitable level. These

situations lead to high shear layers at high flow rates. A disturbance with a very small amplitude starts instabilities to rise dramatically and shear layers roll up to vortices. As a reminder, the flow rate is higher for this flow pattern at peak acceleration compared to the 1.1 seconds case. The vortex is detached from the wall completely at the fifth phase and now it can be specified with ease. After this detachment, it makes translation motion in axial direction at the sixth phase. Moreover, a symmetric region of concentrated high swirling strength can be observed at this phase upstream of the proximal neck vicinity of the walls. This may indicate the generation of a small-sized secondary vortex ring generation as the flow rate is high. Spatial distribution the primary vortex is complex but still symmetric with respect to the horizontal centerline at the seventh phase. Although an additional measurement phase would have been helpful to see details of the evolution of vortex ring, the seventh phase reveals the general mechanics of the vortex. The vortex ring collides with the walls at the converging section before the seventh phase obviously. This collision leads to division of the vortex ring likewise the 1.1 seconds of period case. However, the second primary vortex moves closer to the walls in this case and its maximum swirling strength is in the same order of magnitude as the primary vortex ring. Since the collision at the upper half and down half is not completely the same due to asymmetry, major differences can be observed. Firstly, the cross-section of the primary vortex at the down half loses its swirling intensity dramatically. Then, the primary and the second primary vortex rings can be separately specified regarding their boundaries at the down half meanwhile they are connected in the upper half. Moreover, a new vortex can be identified upstream of the second primary ring, but its upper cross-sections swirling intensity is considerably larger compared to the down half. Lastly, there are two regions with locally high swirling strength values upstream of the primary vortex ring. They are not perfectly symmetric with respect to horizontal centerline. However, the distance between their cores and the centerline is nearly the same. These facts may be indicating the downstream displacement of the secondary vortex ring that generated at the sixth phase. It can be said that the collision of the primary vortex ring resulted in nearly the same flow

characteristics overall as the other unsteady pattern but with some distinct differences. At the eighth phase, primary vortex ring and the second primary one at the upper half separated completely. The primary vortex ring is about the pass through the distal end. The maximum swirling strength values of vortices decrease from the seventh phase to the eighth phase. The ninth phase shows nearly all vortices are about to die out except the second primary vortex ring at the down half. Its swirling intensity is still high. Tenth phase shows no considerable vortices in the bulge. The focused vortices have died out they are about to. It can be said that vortices generated in a cycle is not observed for the successive cycles. This was not valid for the 1.1 seconds case.

4.4.2 Evolution of Primary Vortex Ring

The core of the primary vortex ring can be followed by using Figure 4.18. After the vortex ring is initialized, it follows nearly a perfect axial line till the sixth phase. Between the sixth and the seventh phases, it moves a large distance in axial direction. It should be noted that the vortex ring collides and reflects back from the wall before the seventh phase. Then it is oriented to the distal end at the eighth phase. The cross-section at the up half is located just upstream of the distal end while the one at the down half is located a little more upstream. The primary vortex ring disappears before the ninth phase. This evolution in time shows time the vortex ring forms and dies out quickly as its lifetime is not even in one cycle. This is opposite compared to unsteady flow pattern with 1.1 seconds of period.

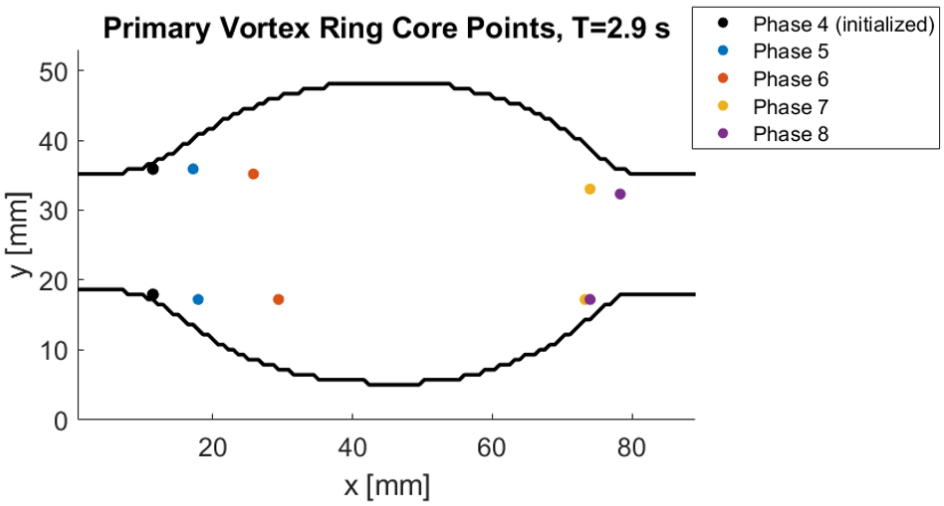

Figure 4.18: Location of primary vortex ring's core with respect to phases, T=2.9 s

The temporal evolution of maximum of swirling strength at the cross-sections of the primary vortex ring can be seen in Figure 4.19. After the vortex ring is formed at the fourth phase, its swirling strength decreases between the fourth and the fifth phases. Then it increases to value close to its initial one. Although a slight increase is observed between the sixth and the seventh phases, collision of the primary vortex ring occurs at that interval, and the maximum swirling strength increases dramatically for the upper cross-section. However, this increase is nearly neutralized by the down cross-section due to asymmetry of the collision. After the seventh phase, the magnitude decreases gradually, and then it leaves the bulge.

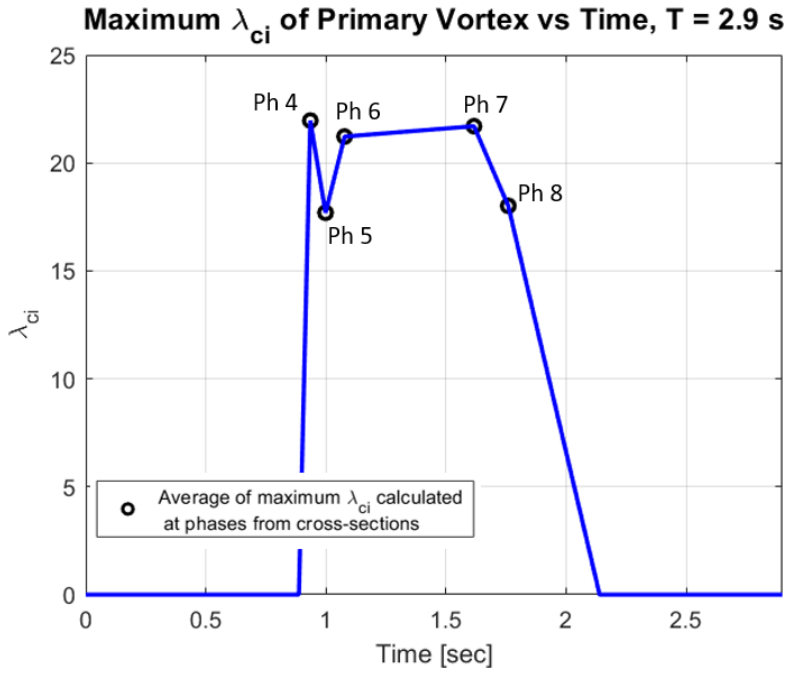

Figure 4.19: Variation of maximum swirling strength of the primary vortex ring calculated at phases in average of cross-sections, T=2.9 s

4.5 Comparison of Vortex Formation Between Physiological Flow Patterns

Physiological flow patterns with different Womersley number and Re variation resulted in a similar vortex ring formation, but there is a slight difference with respect to mean Re or the flow rate. The period of the first case was 1.1 seconds, and it displayed a typical vortex ring generation as flow rate started to decrease. However, for the second physiological flow pattern with a period of 2.9, the primary vortex ring is initialized while the flow rate or Re is still increasing in contrast. An increase in velocity gradients results in the grow of the region where shear layers dominate, and the vortex ring is tended to form easily with the effect of small disturbances and instability. To work on this problem, an alternative method in a quantitative manner other than flow rate or mean Re can be employed. Such an alternative method can provide information about temporal evolution of vortex formation process, and it may give more accurate hints about the phases where the vortex is formed and detached from the surfaces compared to the flow rate variation.

The initialization of the vortex ring can be followed by reviewing the swirling strength contours. The footprints of high swirling strength can be followed in the entrance pipe region. The concentrated region high swirling strength moves downstream and then it detaches from the surface at the proximal edge after the roll up of shear layer process is over. After this detachment, the vortex ring can be identified inside the bulge with its core located out of the wall at an instant. This progress is valid for both of the physiological flow patterns used in this study. The time interval that rolling-up process of shear layers ended to form a robust vortex shape matches with decrease in mean Re for the flow with 1.1 seconds period. For the flow pattern with a period of 2.9 seconds, this time interval still belongs to an interval where Re increases.

An alternative methodology is developed to understand more about vortex ring formation considering an approach to modify swirling strength in wall turbulence [38]. Swirling strength can be normalized with respect to root mean square for every data point in a wall turbulence. Moreover, the axis of rotation can be considered while normalizing by using the sign of vorticity. This methodology is similar to this approach, and it is based on analyzing the velocity gradient depending on the local velocity information. Considering a parabolic velocity profile inside a pipe flow, an increase in Re results in higher gradient across the walls. As the magnitude of gradients increase, the onset of instabilities will be expected to start earlier. Furthermore, the quantitative results of instabilities are also expected to increase just like a turbulent flow. The flow inside AAA geometry is dominated by axial velocity components in magnitude. The gradient of axial velocity in normal direction is dramatically greater than the gradient of normal velocity component in the axial direction. Even a very small gradient in the normal direction may lead to locally high swirling tendency, and reveals it as an increase in parameters of vortex identification methods. Considering these reasons, the derivative of the axial velocity component in the normal direction is used as the basis. The uncertainty and measurement errors in planar PIV experiments must be considered as well. Overall, this is a sensitive process to identify well-defined vortices inside AAA.

This methodology is applied to entrance pipe only as this is the place vortex ring is initialized as seen from footprints of high swirling strength for both physiological flow patterns. The velocity data between the walls and center velocity in the pipe is used. As a note, the first two data points vicinity of the wall are not used to avoid bias and measurement errors close to the walls as expected in PIV measurements. To analyze axial velocity gradients with respect to local axial velocity magnitudes, a simple normalization is done as in (4.1).

$$\frac{\partial u^*}{\partial y^*} = \frac{\frac{\partial u}{\partial y}}{\frac{u}{\Delta x}} \tag{4.1}$$

The numerator is simply the velocity gradient calculated using the least squares method. The denominator corresponds to the normalization term, consisting the axial velocity magnitude at that position and a typical length scale, which is selected as the grid size of the PIV results. The results are calculated in absolute. After that, root mean square of this gradient is calculated for every data point starting from the wall to the data closest to the center of the pipe. This is done to consider the effect of distance from the wall. The root mean square is calculated by following Equation (4.2).

$$\frac{\partial u^*}{\partial y^*}_{RMS} = \sqrt{\frac{1}{n}\left(\frac{\partial u^*}{\partial y^*}_1^{\,2} + \frac{\partial u^*}{\partial y^*}_2^{\,2} + \frac{\partial u^*}{\partial y^*}_3^{\,2} + \cdots + \frac{\partial u^*}{\partial y^*}_n^{\,2}\right)} \tag{4.2}$$

In Equation (4.2), ‘n’ represents the data number that is counted starting from the first data vicinity of the wall to the data point that calculation is being made. The next step is to normalize the gradient obtain in (4.1) with respect to the root mean square at that data point as in Equation (4.3).

$$m = \frac{\frac{\partial u}{\partial y}}{\frac{\partial u^*}{\partial y^*}_{RMS}} \tag{4.3}$$

It is seen that the magnitudes of 'm' hardly change at the same distance from the wall, so an average can be calculated for all cells in the same row in dataset. Considering that the gradient of this variable with respect to distance from the wall is similar for all phases, an average parameter can be determined for all the data points at one half of the entrance region of the inlet pipe. Moreover, this averaging process eases the comparison purpose phase to phase. This parameter is labeled as k and it can be investigated phase by phase for two unsteady flow patterns. The calculation of k can be done by Equation (4.4). In this equation 'N' represents the number of data points used at the entrance pipe.

$$k = \frac{m_1 + m_2 + \cdots + m_N}{N} \tag{4.4}$$

The calculation set of variable k can be seen in Figure 4.20. The first and second rows, which are closes to the wall are not taken into consideration. The variable 'm' is calculated for every data point shown between the red parentheses, and then average is taken.

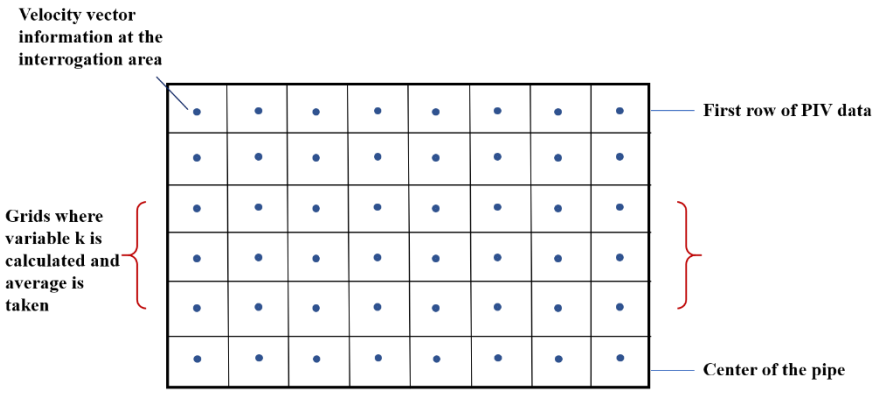

Figure 4.20: Calculation of variable k from PIV dataset (represented without scale)

Variation of k and mean Re of the first physiological flow pattern of 1.1 seconds period is displayed in Figure 4.21. Variation of k and mean Re of the second physiological flow pattern with 2.9 seconds period is displayed in Figure 4.22.

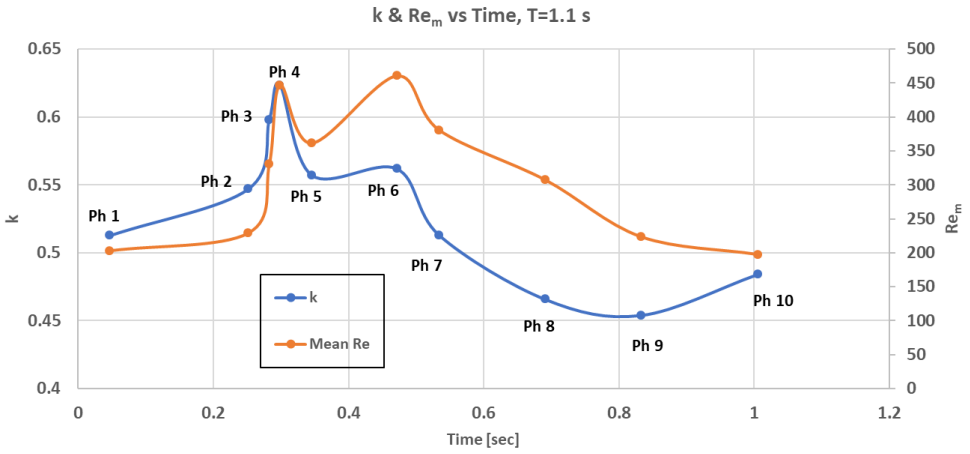

Figure 4.21: Variation of k and mean Re calculated at phases, T = 1.1 s

The variable k follows a similar pattern with mean Re in Figure 4.21. It increases gradually between the first two phases, and then increases rapidly till the fourth phase. A similar evolution of increment in swirling strength can be seen in Figure 4.13. Between the fourth and the fifth phases, a dramatic decrease grabs attention, and this decrease indicates that the concentrated region high swirling strength shifts downstream in the bulge. This fact gives hint about the formation of a detectable robust vortex formation in the bulge. Between the fifth and the sixth phases, k variable stops decreasing and increases instead. This time interval is related with detachment of the vortex ring from the walls.

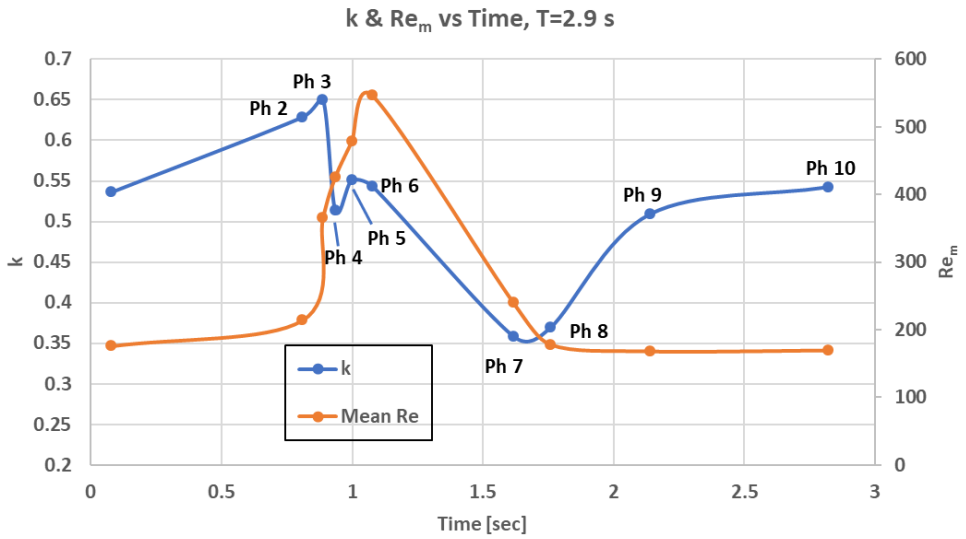

Figure 4.22: Variation of k and mean Re calculated at phases, T = 2.9 s

The variable k increases from the beginning of the cycle till the third phase for period of 2.9 seconds as seen in Figure 4.22. After the third phase, k decreases rapidly contrary to mean Re variation. Just like the flow of 1.1 seconds period, the concentrated region of high swirling stress can be found downstream of the proximal neck for the fourth phase. Between the fourth and the fifth phases, k stops decreasing and increases gradually as in the other physiological flow pattern. This time interval corresponds to detachment of the vortex from the walls.

These observations show that, variable k is able to guess the time interval of the formation of vortex ring and its detachment from the walls. This parameter may provide information about the vortex formation process, and its detachment from the walls. However, further investigation is needed.

4.6 Resolution Dependency

PIV measurements provide discrete data points where every data point is related with an interrogation area consisting of a number of pixels. The results presented in this study are obtained from 32 x 32-pixel interrogation area size with 50% overlap. The

spatial resolution depends on the interrogation area size selection and spatial calibration process. The resolution is not only affecting the estimated variables, but also the derived ones from the velocity field. A low resolution may miss some aspects of the flow field such as small size vortices. Meanwhile, an undesirably high resolution may include noisy data that is very challenging to filter out. To see its effect in this study, two additional interrogation area sizes (64x64-pixels and 24x24-pixels) are applied to the sixth phase of unsteady flow with 2.9 seconds period. It should be noted that an interrogation area of 16 x 16 pixels is also applied, but the resulting data quality was low due to high noise. The seeding particle intensity was not appropriate for that resolution. This phase is selected since the primary vortex ring can be identified easily. The results are displayed in Figure 4.23. The coarsest grid size of 64 x 64 IA provides the smoothest data quality as expected. Although it may be thought as applicable and satisfying, there are large differences in swirling strength values at the straight pipes between this grid size and 32 x 32 IA resolution. It can be said that such a coarse grid size can detect the spatial distribution of vortices, but a quantitative calculation includes high error. On the other hand, 24 x 24 IA gives nearly the same results as with the 32 x 32 but with higher noise. However, the locations of robustly identified vortices are the same.

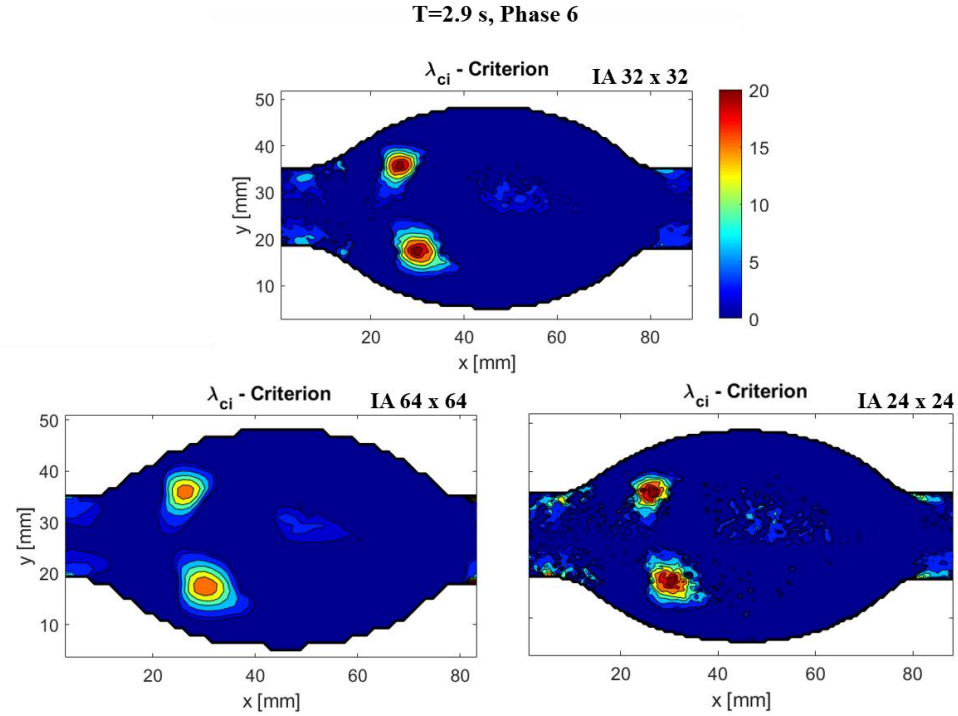

Figure 4.23: λ_{ci} contours of different interrogation area sizes applied at the sixth phase of T=2.9 s, 32 x32 at top, 64 x 64 at left-down and 24 x 24 at right-down

The identified primary vortex ring is also evaluated quantitatively with the maximum swirling strength value at the vortex core for different grid sizes. The results are presented in Table 4.1. The resolution given in this table refers to the original distance between the IA windows before overlap is applied. The maximum swirling strength increases slightly as the resolution gets higher. IA window size with 24 x 24 pixel shows 6.3% change in average with respect to the original 32 x 32 size. The flow field looks the same in. Moreover, 24 x 24 pixels include more noisy data with more measurement errors. Considering these, 32 x32 pixel interrogation area size can be said to be appropriate for this study.

Table 4.1: Variation of maximum swirling strength of the primary vortex with respect to resolution

IA size in pixels	Resolution in mm	Maximum λ_{ci} at the upper half	% Change	Maximum λ_{ci} at the down half	% Change
64 x 64	28.72	16.87	-	17.87	-
32 x 32	14.36	20.91	23.95	21.52	20.43
24 x 24	7.18	22.40	7.13	22.70	5.48

4.7 Performance of Vortex Detection Methods

4.7.1 Streamline Pattern

Streamline pattern is already proven to be unpractical to detect vortices. The hill-like pattern observed in streamlines are observed to be vortex regions from swirling strength distribution. In these kinds of situations, a Galilean decomposition can be made by decomposition of the velocity field in the vortex area detected by swirling strength [39]. As seen in Equation (4.5), the velocity at a region can be written as the sum of a convection velocity and the deviation of it. If the convection velocity is subtracted, the swirling motion can be identified from streamlines as well. The found convection velocity can be thought to be the velocity of the vortex core [39].

$$\vec{u} = \overrightarrow{U_c} + \overrightarrow{u_c} \tag{4.5}$$

Where:

$\overrightarrow{U_c}$: Convection velocity found by averaging the velocity components at a local region

$\overrightarrow{u_c}$: Deviation at a point from the convection velocity

The described procedure above is followed for the hill-like streamline pattern located at down half, upstream of the identified vortex ring in the third phase of the physiological flow with the period of 1.1 seconds. The region with high swirling strength is identified, and the average for both velocity components are found. Then, different percentages of the average velocity components are tried out as the convection velocity. A comparison can be made between the original pattern and the one with decomposition applied in Figure 4.24, in which the convection velocity is estimated as 60% of the average velocity at that region. The streamline pattern is now also able to identity the vortex region at the down half as closed streamline pattern likewise locally high values of swirling strength at that location.

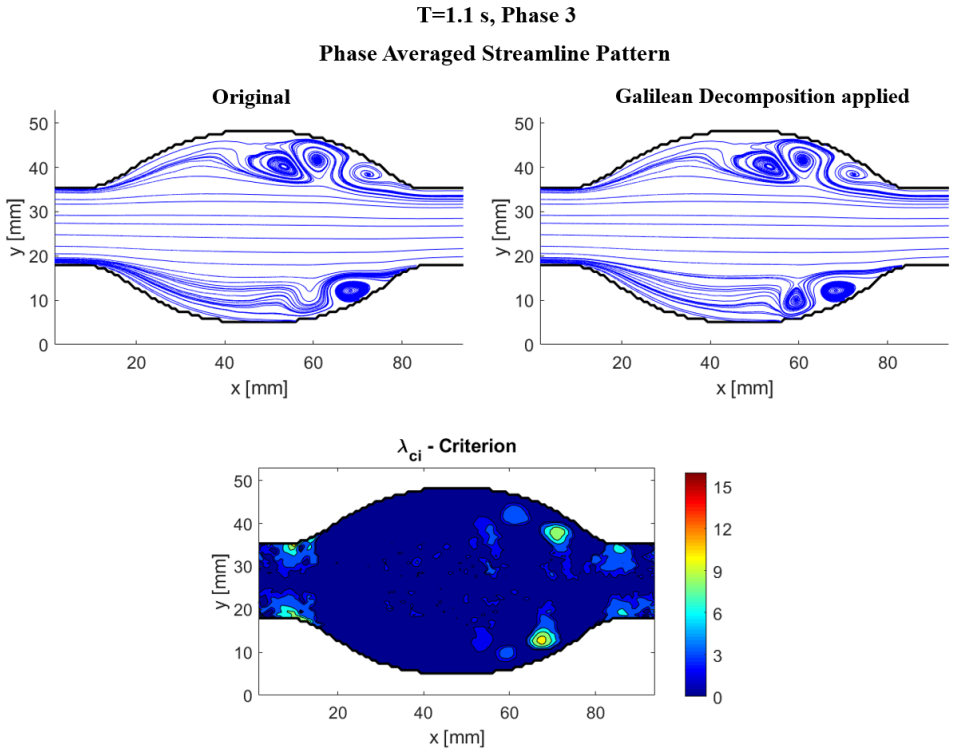

Figure 4.24: Original streamline pattern for the third phase of T=1.1 s, Galilean decomposition applied at right, and λ_{ci} – criterion at bottom

4.7.2 Vorticity Magnitude

Vorticity magnitude failed in steady flow as shown in Figure 4.3. A more detailed investigation is done in this part for physiological flow pattern. The last phase and the first phase, phase 10 and phase 1, of the unsteady flow pattern with 1.1 seconds of period can be the basis to evaluate the performance of vorticity magnitude to capture vortices under unsteady flow conditions. There are two important vortex structures at the tenth phase, which are the primary and secondary vortex rings. At the first phase, there is a third vortex labeled as second primary, which is identified by both streamline and swirling strength contours in Figure 4.11, Figure 4.12, Figure 4.13 and Figure 4.14.

Vorticity magnitude approach is able to identify existing two vortex rings clearly in the tenth phase as shown in Figure 4.25. The secondary vortex rings rotation axis is opposite of the primary vortex ring as expected. However, vorticity magnitude could not identify the third vortex structure which is the second primary vortex ring at the first phase. This observation shows that the vorticity magnitude is not always a valid method to extract the information about a vortex structure's size, especially for small time and length scale vortex structures such as the second primary vortex ring observed at the first phase.

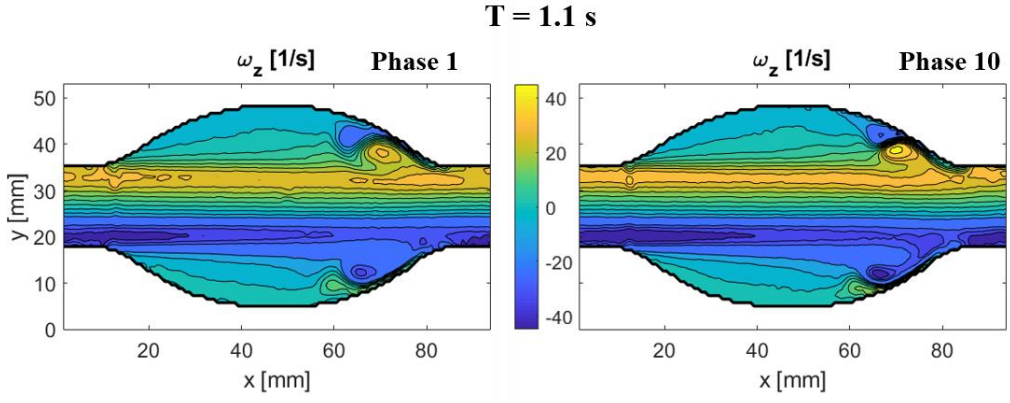

Figure 4.25: Vorticity magnitude, phase 10 at left and phase 1 at right, T=1.1 s

4.7.3 A Comparison of λ_{ci}, Q, Δ and λ_2 Criteria

These four criteria that reviewed in this study are applied at one common phase for comparison. For this comparison purpose, no threshold is selected for any of these methods. The locations identified as vortices by these methods are presented in Figure 4.26. All methods perform similarly with nearly negligible differences. Differently identified regions with small sizes correspond to very weak variable of the criterion that is being applied. They are generally ignored when a threshold is applied. It can be said that λ_2 method identifies the least vortices. While λ_{ci} - criterion and Δ - criterion provide the same results. Lastly Q - criterion identifies vortices between these methods. These results are as expected considering Figure 2.11. It can be said that they are practically the same in this study.

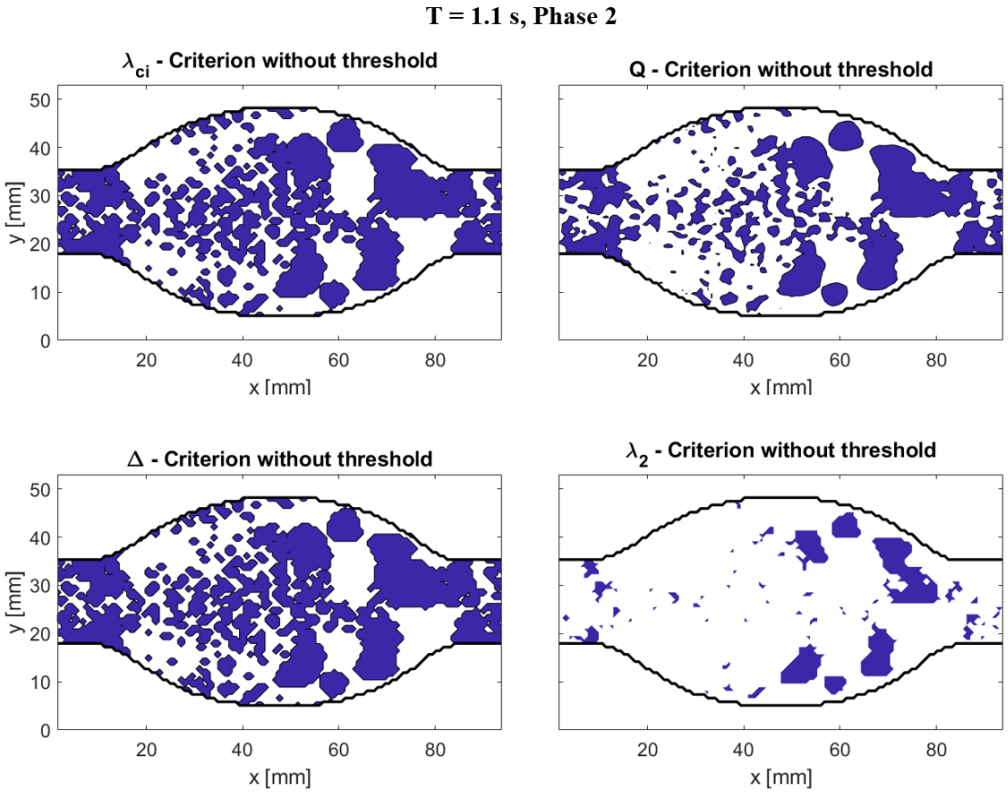

Figure 4.26: Regions identified as vortices by λ_{ci}, Q-criterion, Δ-criterion and λ_2-criterion without any threshold for comparison at the same phase of T=1.1 s

4.8 Reducing Noise in Vortex Identification Methods

As seen the in the unsteady flow results in this work, vortex identification methods depend on the magnitude of a variable calculated from discrete velocity data in an PIV experiment. The resolution of the discreet data, the effectiveness of the mixing of the seeding particles have effect on the parameters. Moreover, the two-dimensional swirling strength analysis may include errors as the investigated real vortices are not perfectly normal to the PIV measurement plane [40]. These reasons prove that vortex identification in real unsteady flows consisting a number of vortices with different scales is a challenging process for planar PIV measurements. Some methods are applied to filter the noisy data and obtain smoother results.

4.8.1 Increasing the Threshold

The first and easiest approach is to increase the threshold of the methods. The second phase of the unsteady flow pattern with period of 1.1 seconds can be considered for this purpose, where there are three vortex structures that are focused in the scope of this study. These vortices are identified both by streamline pattern and swirling strength contours. The maximum of swirling strength can be an initial point to select a threshold. Different percentages of the maximum value are selected as thresholds and applied. The results can be seen in Figure 4.27. A threshold of 10% is seen to be filtering most of the noise very well. The threshold of 20% percent of maximum seems to filter more of the unrealistic vortex structures downstream of the proximal neck. However, real vortices with small swirling strength values cannot be captured in a robust way. The size specification of them may be different than the real case. If the highest threshold is applied, the second primary vortex at the down half becomes completely missing. This shows that a direct threshold approach is not good if small scale and weak swirling vortices exist in the flow field.

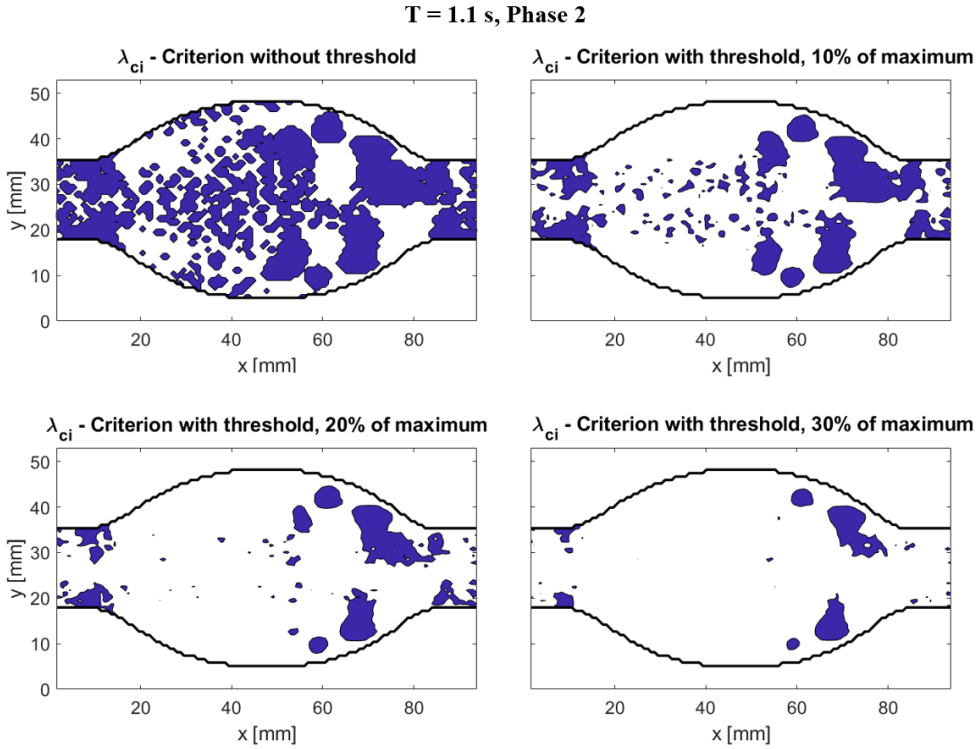

Figure 4.27: Vortex locations identified by different thresholds of λ_{ci} at the second phase of T=1.1 s

A similar approach is also followed for Q-criterion. The results are presented in Figure 4.28. A threshold of 3% of the maximum swirling strength filters most of the noisy data and three prominent vortex structures can be identified easily. A threshold of 6% misses the second primary vortex ring at the down half. Increasing the threshold more results in nearly no noise, but small sized vortices are all missing. It can be said that a simple threshold selection will filter out most of the noisy data in planar PIV measurements. However, one must make sure that the threshold must be small enough to capture weak vortices, yet large enough to filter most of the noisy data.

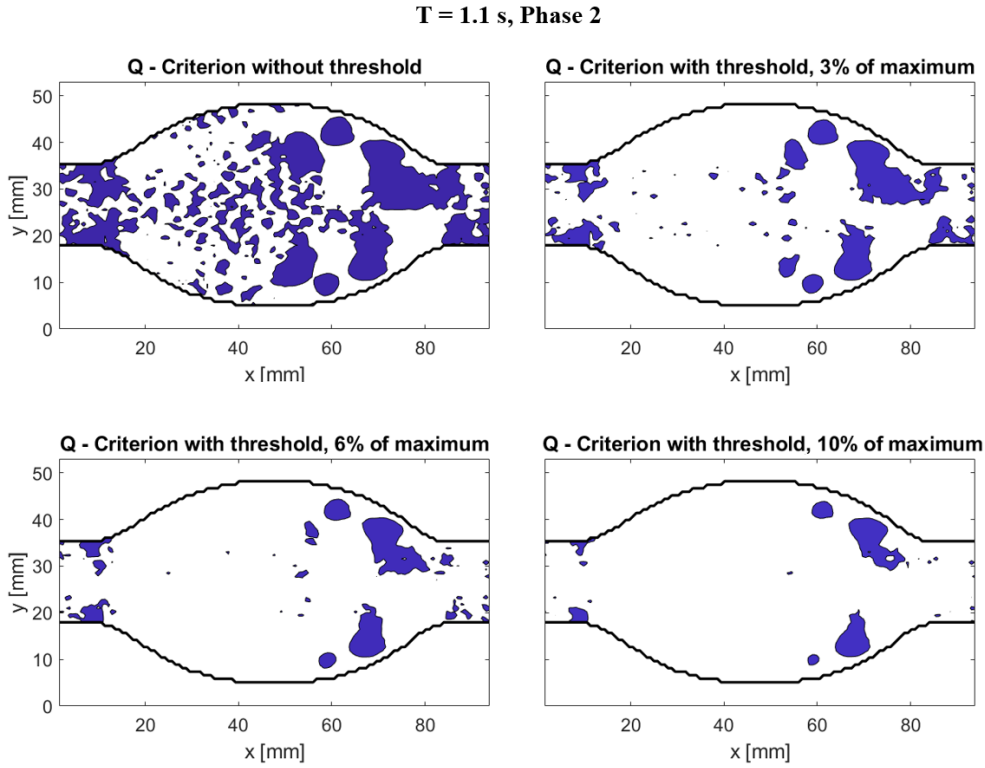

Figure 4.28: Vortex locations identified by different thresholds of Q-criterion at the second phase of T=1.1 s

4.8.2 An Alternative Method

The growing region method has three steps to identify the vortex cores [38]. The first step is to find the local maxima values of the swirling strength. Then, a typical threshold, such as 1.5, is applied to potential vortex core locations. It is expected to recognize at least three grids in one direction with higher swirling strength than the selected threshold. The last step is to scan the values from the highest to lower ones starting from the center to outward direction to specify the limits of the vortex as the name of the method implies. This method can be followed in this study as well. The first step is to identify the local maxima values in dataset of PIV measurements so that they are labeled as potential vortex cores PIV experiments provide discrete data. To define a vortex structure, a certain size is needed where rotation occurs around a common point. If there is a core of the vortex which is one interrogation area for

PIV, the particles just around it must show a characteristic behavior to create a vortical motion. A typical vortex structure can be seen in Figure 4.29. Every cell can be thought as an interrogation area in PIV. To have a well-defined spatial description of the vortex core, a minimum grid structure having nine elements can be used as a first approach. Here, instead of three grid size in one direction, it is looked in both of the directions. This may cause some small-scale vortices to be missed out but the vortices can be captured in a more robust way. The connectivity of each element to its eight neighboring cells are considered during local maxima determination.

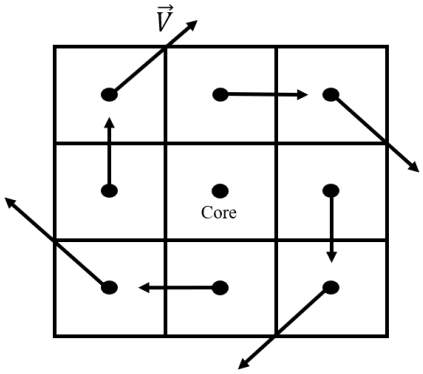

Figure 4.29: A vortex with square grid size of 3

After these steps, potential vortex core will be labeled. Regarding PIV, there might be more than one local maximum values in the same vortex core due to measurement errors or uncertainties. These regions may contain more than one vortex, and the boundary between them cannot be identified due to finite swirling strength values. It may not be possible to determine the exact core of a vortex. If this case is realized, instead of a growing mechanism, the local high values may be linked up together to specify the spatial distribution of the vortex.

The potential vortex cores identified by this method is shown for the fourth phase at left and the fifth phase at right in Figure 4.30. As it was explained, there are a couple of points for the fourth phase located in the same vortex as the potential core while for the fifth phase only two very close points were found out. The fourth phase can

be a good basis to test this alternative method to eliminate the potential vortex cores, which are not the real ones. It should be noted that normalization is done for the straight pipes with respect to root mean squares to eliminate vortex core points inside these pipes.

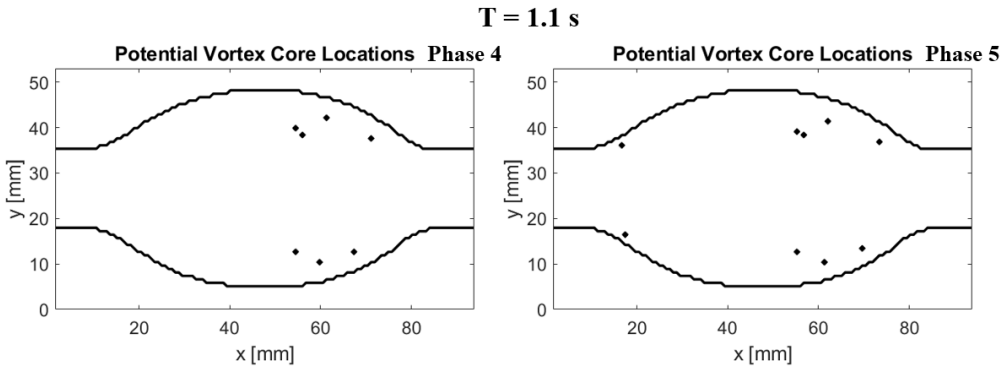

Figure 4.30: Potential vortex core locations with alternative method applied, phase 4 at left and phase 5 at right, T=1.1 s

After the potential points identified, the points that can be connected in a region with swirling strength magnitudes over the threshold are unified in one common vortex. This procedure is applied to the fourth phase of the psychological flow pattern and the results can be seen in Figure 4.31. The vortex cores are revealed clearly. Moreover, all the regions with high swirling strength, but with small grid size are neglected with this method. This method can be further developed. Nonetheless, this method could be able to provide more smooth data with more robust vortices identified, while sacrificing the sensitivity to capture very small scaled vortices with grid size lower than 3. The resolution depends on the spatial calibration of PIV experiments. However, it is certain that 2D PIV measurements require strict and well-defined methods to identify vortices.

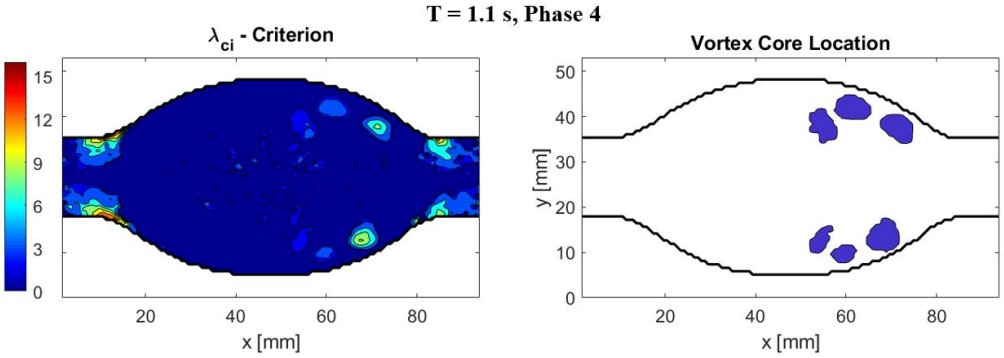

Figure 4.31: Default λ_{ci} contour at left and alternative method applied at right for the fourth phase of T=1.1

CHAPTER 5

CONCLUSION

This work aims to characterize vortex rings occuring in a AAA phantom with PIV measurements. To achieve this aim, an experimental setup is designed and installed. The cost of the experimental setup is minimized by producing the vessel from glass and preparing a working fluid with NaSCN. RI match between the phantom and the working fluid is satisfied. Planar PIV measurements are taken for one steady flow and two physiological flow patterns with different periods. Physiological flow patterns are investigated with respect to selected phases of the cycles. Pressure waveform of physiological flow patterns are obtained by implementing pressure transducers at certain locations of the experimental setup. Some of the most popular vortex identification methods; swirling strength criterion, Δ - criterion, Q - criterion and λ_2 - criterion are reviewed and implemented. Vortex formation process in the flow field is studied and explained in detail. Moreover, some methods are tested to filter out the noisy data in planar PIV measurements. The post process is done by the developed code. This code is applicable to planar PIV dataset of closed conduits. It specifies the boundaries of the phantom, and applied the vortex identification methods by calculating the variables from the velocity field. It can be developed further for multiplane measurements, or 3D VGT.

It is known that a vortex ring dominates the flow in a AAA case. The spatial and temporal evolution of the vortex ring depends on the geometry of the aneurysm and the flow pattern. In this study, a simplified and axisymmetric geometry with an elliptical cross-section is utilized. A typical steady flow is studied, by conducting an experiment of Re = 600. It is seen that a vortex ring occupies the bulging section while jet flow is not disturbed. Moreover, the reviewed vortex identification methods provide the same results in this case. The flow field and developed code are validated by considering the results of steady flow. Flow field validation is made by

considering a previous study, and a post-process software is used for comparison of derived vortex parameters. Considering this validation study, the results are found out to be as expected. Two physiological flow patterns with different periods and mean Re variations are studied by taking measurements at critical phases of these cycles. In both cases, a vortex ring is initialized after the instabilities arise considerably. The formation process can be followed from the foorprints of increasing swirling strength in the entrance pipe. These instabilities affect the shear layers arising as the flow rate increases. Although deceleration can result in rolling of the shear layers into a vortex ring, its formation can start earlier than the beginning of deceleration. Therefore, variation of Re or flow rate could not be the only parameter to follow, especially if the vortex ring formation is being studied in detail. An alternative quantitative method is tried out by considering the gradient of the streamwise velocity in the normal direction. In this method the effect of distance from the wall is also considered by implementing root mean square calculation. This method shows that vortex ring formation and detachment can be followed by the derived parameter at the entrance pipe, since it provides information about the displacement of the instabilies from the entrance of the pipe to the bulge section. The formed vortex ring is symmetric for both cases with respect to the horizontal centerline. This primary vortex ring collides with the walls at the converging section of the walls for both cases towards the end of cycle. The collision leads to formation of two additional vortices. One of them is secondary vortex as its direction of rotation is opposite of the primary vortex. The last one is occuring due to the division of the primary vortex ring. The vortex rings in the flow pattern with lower Womersley number (higher period) have higher swirling intensity compared to the one with higher Womersley number. However, the vortices leave the bulge in one cycle for this pattern, while for the one with higher Womersley number they remain in the bulge for two cycles.

Different approaches are followed to identifity these vortices. Vorticity magnitude and streamline patterns are proved to be insufficient, especially for the weak vortices with small scale. Vorticty magnitude fails as it contains shear layers, which are not

vortices, that are located vicinity of the walls. Moreover, vortices close to each other with the same axis of rotation cannot be identified by vorticity contours. In PIV experiments of AAA studies, the seeding particles must mix as homogeneous as possible to reveal vortex structures. However, this is a very hard process to occur, and it can be said that there is nearly no control over it in a closed conduit. As velocity magnitudes are changing drastically in a closed flow dominated by shear layers and vortex structures, streamlines may not capture the real vortex rings. This case is observed very clearly in this study. However, they still provide valid information to study on large scale vortex structures. Swirling strength criterion, Δ - criterion, Q - criterion and λ_2 - criterion methods are tested for different phases of the cycles, and they are seen to provide the same results for planar PIV measurements for physiological flow patterns as well. The differences only occur at the locations where the calculated variable for the method is very low compared to the robust vortices, which is associated with noise. It is seen that a filtration is required to get rid of noisy data for every vortex identification method applied to planar PIV measurements. Increasing the threshold is seen to be a helpful first step. However, it should be kept small enough to capture small sized vortices. Increasing the threshold too much may result in missing vortices with weak swirling intensity. An alternative method is applied in which local maxima of the variables of the vortex identification methods are considered as the potential vortex cores. It is found out that, the threshold selection can be implemented for the neighboring cells of these potential vortex cores. Noisy data occupying small grid size can be removed by establishing a requirement that searches for swirling strength values larger than a threshold at the neighboring cells of loxal maxima points. After this step, connecting the data points with the swirling strength values higher than the threhold can identify the robust vortices in the flow field. However, all these methods can be further developed to operate more efficiently.

5.1 Future Work Suggestions

The effect of non-Newtonian behavior on the vortex structures, and on the shear layer distribution is not defined yet in literature. A working fluid can be converted to a non-Newtonian fluid with the additive of Xanthan gum to obtain shear thinning properties. A comparison can be made under the same flow conditions for two working fluids, one Newtonian and one non-Newtonian. Swirling strength contours of the same phases can be used for this purpose to see the effect on the swirling intensity. Vorticity magnitude can be investigated as well to observe the changes in the shear layer distribution.

Although 2D PIV measurements from one plane provide the general flow structures and vortex mechanisms, 3D measurement will reveal more details about the vortex structures. To obtain 3D VGT with the current setup, multiplane (xy-plane) measurements can be taken at the different heights (z-direction) with small distance between them. However, it should be noted that both axial and cross planes are required. Starting from the middle horizontal plane, the measurement plane can be shifted in the vertical distance (z) step by step till the top and the bottom walls of the phantom in both directions. Since the velocitiy components in these planes at different heights, their gradients in the out of plane direction can be calculated by applying a finite difference method with the distance betweeen them. The out of plane velocity component must be known to calculate its derivatives in the measurement planes. Cross planes will provide these varilables, so the mentioned approach can be follow for cross planes as well. In the end, planar measurements at different heights can be connected in a matrix, so that 3D VGT is obtained.

As an alternative to multiplane planar measurements, stereo PIV setup can be utilizied. By using a second camera and a calibration sheet, the out of plane velocity component can be found by stereo PIV measurement in plane. Since the out of plane component is known for a plane, its derivatives in that plane can also be calculated. However, multiplane measurements are needed to calculate the gradients in the out plane direction. These planes are selected parallel to the initial measurement plane.

This approach is illustrated in Figure 5.1. If the geometry is axisymmetric, multiplane measurements can be taken for only one half, and the results are mirrored with respect to the middle plane. The data points can be connected together to genereate 3D VGT. Lastly, all three components of velocity can be measured by Volumetric PIV measurements with multiple cameras. Time resolved volumetric velocity field, and so their derivatives in three directions can be measured with ease since volumetric PIV provides 3D and three component results. Application of a Volumetric PIV will increase the spatial resolution, and vortex ring can be identified in 3D.

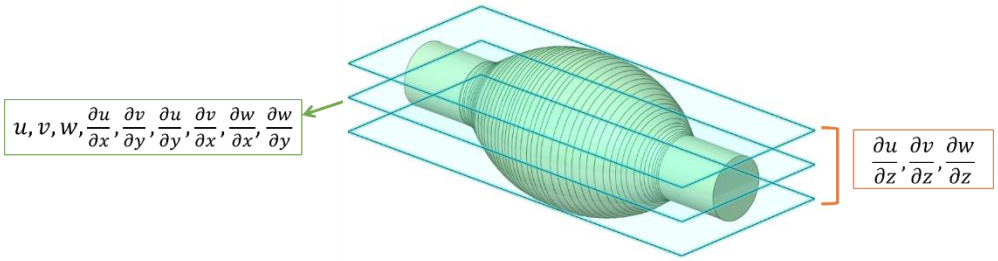

Figure 5.1: Multiplane measurements of stereo PIV to obtain 3D VGT and obtained parameters

REFERENCES

[1] J. Golledge, “Abdominal aortic aneurysm: update on pathogenesis and medical treatments,” Nature Reviews Cardiology, vol. 16, no. 4. Nature Publishing Group, pp. 225–242, Apr. 01, 2019. doi: 10.1038/s41569-018-0114-9.

[2] J. J. Reimerink, M. J. van der Laan, M. J. Koelemay, R. Balm, and D. A. Legemate, “Systematic review and meta-analysis of population-based mortality from ruptured abdominal aortic aneurysm,” British Journal of Surgery, vol. 100, no. 11. pp. 1405–1413, Oct. 2013. doi: 10.1002/bjs.9235.

[3] J. C. Lasheras, “The biomechanics of arterial aneurysms,” Annual Review of Fluid Mechanics, vol. 39. pp. 293–319, 2007. doi: 10.1146/annurev.fluid.39.050905.110128.

[4] F. Gianfagna et al., “Prevalence of Abdominal Aortic Aneurysms in the General Population and in Subgroups at High Cardiovascular Risk in Italy. Results of the RoCAV Population Based Study,” European Journal of Vascular and Endovascular Surgery, pp. 633–639, May 2018, doi: 10.1016/j.ejvs.2018.01.008.

[5] E. G. Lakatta, J. H. Mitchell, A. Pomerance, and G. G. Rowe, “Human aging: Changes in structure and function,” Journal of the American College of Cardiology, vol. 10, no. 2, pp. 42A-47A, 1987, doi: 10.1016/S0735-1097(87)80447-3.

[6] J. T. Powell et al., “Final 12-year follow-up of surgery versus surveillance in the UK Small Aneurysm Trial,” British Journal of Surgery, vol. 94, no. 6, pp. 702–708, Jun. 2007, doi: 10.1002/bjs.5778.

[7] D. H. Modai, R. H. Limet, and N. H. Sakalihassan, “Determination of the expansion rate and incidence of rupture of abdominal aortic aneurysms,” Journal of Vascular Surgery, vol. 14, no. 4, pp. 540–548, Oct. 1991, doi: 10.1067/mva.1991.30047.

[8] A. J. Boyd, D. C. S. Kuhn, R. J. Lozowy, and G. P. Kulbisky, “Low wall shear stress predominates at sites of abdominal aortic aneurysm rupture,” Journal of Vascular Surgery, vol. 63, no. 6, pp. 1613–1619, Jun. 2016, doi: 10.1016/j.jvs.2015.01.040.

[9] S. J. Haller et al., “Intraluminal thrombus is associated with early rupture of abdominal aortic aneurysm,” Journal of Vascular Surgery, vol. 67, no. 4, pp. 1051-1058.e1, Apr. 2018, doi: 10.1016/j.jvs.2017.08.069.

[10] A. Łukasiewicz, A. Garkowski, K. Rutka, J. Janica, and U. Łebkowska, “Evaluation of the thrombus of abdominal aortic aneurysms using contrast enhanced ultrasound - Preliminary results,” Scientific Reports, vol. 6, Sep. 2016, doi: 10.1038/srep34152.

[11] J. Stenbaek, B. Kalin, and J. Swedenborg, “Growth of thrombus may be a better predictor of rupture than diameter in patients with abdominal aortic aneurysms,” European Journal of Vascular and Endovascular Surgery, vol. 20, no. 5, pp. 466–469, 2000, doi: 10.1053/ejvs.2000.1217.

[12] Thurston GB. “Rheological parameters for the viscosity viscoelasticity and thixotropy of blood.” Biorheology. 1979;16(3):149-62. doi: 10.3233/bir-1979-16303. PMID: 508925.

[13] M. Y. Yousif, D. W. Holdsworth, and T. L. Poepping, “Deriving a Blood-Mimicking Fluid for Particle Image Velocimetry in Sylgard-184 Vascular Models,” 2009.

[14] T. J. Pedley, The Fluid Mechanics of Large Blood Vessels. 1980. doi: 10.1017/cbo9780511896996.

[15] J. A. Long, A. Ündar, K. B. Manning, and S. Deutsch, “Viscoelasticity of pediatric blood and its implications for the testing of a pulsatile pediatric blood pump,” in ASAIO Journal, Sep. 2005, vol. 51, no. 5, pp. 563–566. doi: 10.1097/01.mat.0000180353.12963.f2.

[16] E. A. Finol and C. H. Amon, “Blood flow in abdominal aortic aneurysms: Pulsatile flow hemodynamics,” Journal of Biomechanical Engineering, vol. 123, no. 5, pp. 474–484, 2001, doi: 10.1115/1.1395573.

[17] S. G. Yazdi, P. H. Geoghegan, P. D. Docherty, M. Jermy, and A. Khanafer, “A Review of Arterial Phantom Fabrication Methods for Flow Measurement Using PIV Techniques,” Annals of Biomedical Engineering, vol. 46, no. 11. Springer New York LLC, pp. 1697–1721, Nov.15,2018. doi: 10.1007/s10439-018-2085-8.

[18] A. v. Salsac, S. R. Sparks, J. M. Chomaz, and J. C. Lasheras, “Evolution of the wall shear stresses during the progressive enlargement of symmetric abdominal aortic aneurysms,” Journal of Fluid Mechanics, vol. 560, pp. 19–51, 2006, doi: 10.1017/S002211200600036X.

[19] M. C. Brindise, M. M. Busse, and P. P. Vlachos, “Density- and viscosity-matched Newtonian and non-Newtonian blood-analog solutions with PDMS refractive index,” Experiments in Fluids, vol. 59, no. 11. Springer Verlag, Nov. 01, 2018. doi: 10.1007/s00348-018-2629-6.

[20] M. R. Najjari, J. A. Hinke, K. v. Bulusu, and M. W. Plesniak, “On the rheology of refractive-index-matched, non-Newtonian blood-analog fluids for PIV experiments,” Experiments in Fluids, vol. 57, no. 6. Springer Verlag, Jun. 01, 2016. doi: 10.1007/s00348-016-2185-x.

[21] E. M. Pedersen, A. P. Yoganathan, and X. P. Lefebvre, “Pulsatile flow visualization in a model of the human abdominal aorta and aortic bifurcation,”

Journal of Biomechanics, vol. 25, no. 8, 1992, doi: 10.1016/0021-9290(92)90234-R.

[22] V. Kolář, "Vortex identification: New requirements and limitations," International Journal of Heat and Fluid Flow, vol. 28, no. 4, pp. 638–652, Aug. 2007, doi: 10.1016/j.ijheatfluidflow.2007.03.004.

[23] B. P. Epps, "Review of vortex identification methods," 2017. doi: 10.2514/6.2017-0989.

[24] H. J. Lugt, "The dilemma of defining a vortex.," 1979, doi: 10.1007/978-3-642-67220-0_32.

[25] J. Jeong and A. N. D. Fazle Hussain, "On the identification of a vortex," 1995.

[26] M. S. Chong, A. E. Perry, and B. J. Cantwell, "A general classification of three-dimensional flow fields," Physics of Fluids A, vol. 2, no. 5, pp. 765–777, 1990, doi: 10.1063/1.857730.

[27] J. C. R. Hunt', A. A. Wray2, and P. Moin3, "N89-24555 Eddies, Streams, and Convergence Zones in Turbulent Flows."

[28] Zhou, J., Adrian, R., Balachandar, S., & Kendall, T. (1999). Mechanisms for generating coherent packets of hairpin vortices in channel flow. *Journal of Fluid Mechanics, 387*, 353-396. doi:10.1017/S002211209900467X

[29] Q. Chen, Q. Zhong, M. Qi, and X. Wang, "Comparison of vortex identification criteria for planar velocity fields in wall turbulence," Physics of Fluids, vol. 27, no. 8, Aug. 2015, doi: 10.1063/1.4927647.

[30] C. Stamatopoulos, Y. Papaharilaou, D. S. Mathioulakis, and A. Katsamouris, "Steady and unsteady flow within an axisymmetric tube dilatation," Experimental Thermal and Fluid Science, vol. 34, no. 7, pp. 915–927, 2010, doi: 10.1016/j.expthermflusci.2010.02.008.

[31] S. C. M. Yu, "Steady and pulsatile flow studies in Abdominal Aortic Aneurysm models using Particle Image Velocimetry."

[32] V. Deplano, Y. Knapp, E. Bertrand, and E. Gaillard, "Flow behaviour in an asymmetric compliant experimental model for abdominal aortic aneurysm," Journal of Biomechanics, vol. 40, no. 11, pp. 2406–2413, 2007, doi: 10.1016/j.jbiomech.2006.11.017.

[33] V. Deplano, C. Meyer, C. Guivier-Curien, and E. Bertrand, "New insights into the understanding of flow dynamics in an in vitro model for abdominal aortic aneurysms," Medical Engineering and Physics, vol. 35, no. 6, pp. 800–809, 2013, doi: 10.1016/j.medengphy.2012.08.010.

[34] V. Deplano, C. Guivier-Curien, and E. Bertrand, “3D analysis of vortical structures in an abdominal aortic aneurysm by stereoscopic PIV,” Experiments in Fluids, vol. 57, no. 11, 2016, doi: 10.1007/s00348-016-2263-0.

[35] J. Biasetti, F. Hussain, and T. Christian Gasser, “Blood flow and coherent vortices in the normal and aneurysmatic aortas: A fluid dynamical approach to intraluminal thrombus formation,” Journal of the Royal Society Interface, vol. 8, no. 63, 2011, doi: 10.1098/rsif.2011.0041.

[36] S. S. Gopalakrishnan, B. Pier, and A. Biesheuvel, “Dynamics of pulsatile flow through model abdominal aortic aneurysms,” Journal of Fluid Mechanics, vol. 758, 2014, doi: 10.1017/jfm.2014.535.

[37] M. Raffel et al., Particle Image Velocimetry: A Practical Guide, vol. 2nd. 2007.

[38] H. Chen, D. Li, R. Bai, and X. Wang, “Comparison of swirling strengths derived from two- and three-dimensional velocity fields in channel flow,” AIP Advances, vol. 8, no. 5, May 2018, doi: 10.1063/1.5023533.

[39] R. J. Adrian, K. T. Christensen, and Z.-C. Liu, “Analysis and interpretation of instantaneous turbulent velocity fields.”

[40] R. Camussi and F. di Felice, “Statistical properties of vortical structures with spanwise vorticity in zero pressure gradient turbulent boundary layers,” Physics of Fluids, vol. 18, no. 3, 2006, doi: 10.1063/1.2185684.